2007-07-13

Investigation of Particle Velocity and Drag with Spherical and Non-Spherical Particles Through a Backward Facing Step

Kyle Frederick Larsen
Brigham Young University - Provo

INVESTIGATION OF PARTICLE VELOCITY AND DRAG WITH SPHERICAL AND NON-SPHERICAL PARTICLES THROUGH A BACKWARD FACING STEP

by

Kyle F. Larsen

A dissertation submitted to the faculty of

Brigham Young University

in partial fulfillment of the requirements for the degree of

Doctor of Philosophy

Department Mechanical Engineering

Brigham Young University

August 2007

BRIGHAM YOUNG UNIVERSITY

GRADUATE COMMITTEE APPROVAL

of a dissertation submitted by

Kyle F. Larsen

This dissertation has been read by each member of the following graduate committee and by majority vote has been found to be satisfactory.

Date	Dale R. Tree, Committee Chair
Date	Matthew R. Jones, Committee Member
Date	R. Daniel Maynes, Committee Member
Date	Scott L. Thomson, Committee Member
Date	Brent W. Webb, Committee Member

BRIGHAM YOUNG UNIVERSITY

As chair of the candidate's graduate committee, I have read the dissertation of Kyle F. Larsen in its final form and have found that (1) its format, citations, and bibliographical style are consistent and acceptable and fulfill university and department style requirements; (2) its illustrative materials including figures, tables, and charts are in place; and (3) the final manuscript is satisfactory to the graduate committee and is ready for submission to the university library.

Date

Dale R. Tree
Chair, Graduate Committee

Accepted for the Department

Matthew R. Jones
Graduate Coordinator

Accepted for the College

Alan R. Parkinson
Dean, Ira A. Fulton College of Engineering and Technology

ABSTRACT

INVESTIGATION OF PARTICLE VELOCITY AND DRAG WITH SPHERICAL AND NON-SPHERICAL PARTICLES THROUGH A BACKWARD FACING STEP

Kyle F. Larsen

Department of Mechanical Engineering

Doctor of Philosophy

Numerous practical applications exist where dispersed solid particles are transported within a turbulent accelerating or decelerating gaseous flow. The large density variation between phases creates the potential for significant differences in velocity known as velocity slip. Flow over a backward facing step provides a well characterized, turbulent, decelerating flow useful for measuring the relative velocities of the solid and gaseous phases in order to determine velocity slip and particle drag. Numerous investigations have been conducted to determine the gas phase velocity in a backward facing step for both laminar and turbulent flows and therefore the gas phase flow is well know and documented. Furthermore, some studies have also been conducted to determine the velocity of various sizes of spherical particles in a backward facing step

and compared with their corresponding gas phase velocities. Few if any velocity measurements have been made for non-spherical particles in a backward facing step.

In this work, a Phase Doppler Particle Analyzer (PDA) was used to measure gas and particle phase velocities in a backward facing step. The step produced a 2:1 increase in cross sectional area with a Reynolds number of 22,000 (based on step height) upstream of the step. Spherical particles of 1 – 10 μm with an average diameter of 4μm were used to measure the gas phase velocity. At least three sizes in the range of (38 – 212 μm) for four different particles shapes were studied. The shapes included: spheres, flakes, gravel, and cylinders. Since the PDPA is not able to measure the size of the non-spherical particles, the particles were first separated into size bins and a technique was developed using the PMT (photo multiplier tubes) gain to isolate the particle size of interest for each size measured. The same technique was also used to measure terminal velocities of the particles in quiescent air.

The measured gas phase velocity and spherical solid phase particles were in good agreement with previous measurements in the literature. The results showed relative velocities between the particles and gas phase to be in the range of 0 – 3 m/s which is in transition between stokes flow and fully developed turbulent flow. Drag coefficients were an order magnitude higher for non-spherical particles in turbulent flows in comparison to stokes flow which agreed reasonably well with quiescent terminal velocity drag. This information is valuable for modeling turbulent two-phase flows since most assumptions of the drag are currently based on correlations from empirical data with particles moving through a still fluid.

ACKNOWLEDGMENTS

I would first like to thank my wife, Joni, who has supported and encouraged me throughout the time I have spent at BYU in the pursuit of my doctoral degree. Her great love, dedication, faith and patience have been instrumental in making this all possible. Even after the many long years of struggling to get through school she has never given up on me. I would also like to thank all my dear children for their great love and support especially for all their prayers in my behalf. In addition to the great love and dedication of my wife and children, both our extended families have also been very supportive while we have been at BYU. I am also very grateful to my parents for all their encouragement and help and to my wife's parents who have also helped to make this all possible.

I would also like to acknowledge the support of my advisor, Dr. Dale Tree, in the research work that I have done. Dr. Tree was very kind to take me on as a graduate student after the departure of my prior advisor from BYU. I know I wasn't always an easy student to work with and I thank him for all his patience and understanding. I appreciate both our friendship and our professional association. His advice and counsel concerning the work done for this dissertation during the years we worked together has been an essential part of finishing the work presented here. I also appreciate the support of my advisory committee during my time at BYU. They have always been willing to provide me the necessary help and support to complete my research.

Lastly, I would like to thank all the other people at BYU that have helped me over the many years which include other faculty members and people such as Susan Phillips, Kevin Cole, Keith Nielson, Ken Forster, my janitor friends and many others.

TABLE OF CONTENTS

LIST OF TABLES

LIST OF FIGURES

Nomenclature

Variable	Units	Definition
A	m^2	area
C_D	__	drag coefficient
d_f	μm	fringe spacing
d_p	μm	particle diameter
du_p	m/s	derivative in particle velocity
du_p/d_t	m/s^2	particle acceleration
du_f/d_x	1/sec	spatial gradient of velocity
f	mm	focal length
F_d	N	drag force
f_d	1/sec	scatter frequency
fr	mm	separation of projected fringes from particle
F_x	N	other forces
g	m/s^2	gravity
g_x	m/s^2	gravity in the x-direction
$\vec{k}$	__	laser ray
l_k	μm	Kolmogorov's microscale of turbulence
l_o	μm	integral length scale
l_λ	μm	Taylor's microscale of turbulence
p	kPa	pressure
q	kg/s	mass flow rate

Re	__	Reynolds number
S_{mas}	__	max slip
t	sec	time
T	varies	temperature
u or u_g	m/s	gas velocity
u_p	m/s	particle velocity
u_x	m/s	particle velocity through measurement volume
V′	__	turbulent intensity
V_p	m^3	particle volume
ρ	kg/m^3	density of gas (air)
ρ_p	kg/m^3	density of particle
μ	$N{\cdot}s/m^2$	absolute viscosity of gas (air)
Ø	__	sphericity
$Ø_{AB}$	mm	spacing between photo-detectors A and B
$Ø_{AC}$	mm	spacing between photo-detectors A and C
ω_p	radian/sec	angular particle velocity
κ	degrees	beam angle
λ	nm	wavelength
α	__	discharge coefficient
θ	degrees	laser receiver offset angle
θ_c	__	critical pressure ratio
τ	degrees	angle of refracted rays
τ	sec	period for turbulent fluctuations
Δs	μm	separation of projected fringes
Δs′	μm	photo-detector separation

1 Introduction

Two-phase flows are important in numerous industrial applications, including combustors, furnaces, spray drying, spray forming and fire suppression. These devices normally entrain solid particles or liquid droplets in air or entrain solid particles within a liquid. The ability to predict particle velocity, position and mass in both phases is often critical in the design of these devices. In many processes, particularly those involving liquid fuels or sprays, the particles (droplets) are spherical. However, non-spherical particles are also very common for applications where the particles are produced through pulverizing, grinding and crushing, such as with coal, bio-mass, and other solid materials. Obtaining experimental data for the flow of non-spherical particles is crucial to being able to provide useful data necessary to optimize these processes and accurately validate computer codes that model particle dispersion. The drag coefficient is a fundamental engineering parameter which must be determined in order to predict the forces on a particle within a flow. The objective of this work is to measure the drag coefficients of non-spherical particles at Reynolds numbers and in flows characteristic of practical applications.

An example of an application of non-spherical particles in a two-phase flow is found in biomass or coal-biomass co-firing in a utility boiler. Biomass consists of forest, agricultural, or waste products which are ground or crushed to sub millimeter sized particles before being introduced into a furnace. When burned with pulverized coal, the

coal and biomass are conveyed with primary air into the boiler where they mix with hot combustion products that ignite the fuel followed by secondary air which is used to burn up the fuel. Re-circulating products and turbulent flow are used to stabilize the flame and mix products and reactants at the proper rates to minimize pollutants and maximize burnout. Non-spherical particles in the 50 – 1000 μm range are therefore experiencing accelerating and decelerating, turbulent flows.

Empirical data and fundamental descriptions of drag on non-spherical particles in this type of flow are lacking in the literature. Most of the data for non-spherical shapes is collected in wind tunnels for large objects and settling or terminal velocity measurements for particles. These flows lack the fundamental physical characteristics and scaling found in the example described above. Namely, the flow is not turbulent with length scales both ranging above, through, and below the size of the particles in addition to applying net forces on the particles which scale with the difference in the average velocities of the two phases. Forces which will tend to rotate the particle or rapid changes in the orientation of the particle relative to the flow are expected to occur on a time scale much shorter than is represented by average velocities. Thus it is important to produce an experimental flow field characteristic of the turbulent flows found in many practical applications from which relevant data can be obtained and new theories related to forces on the particles can be tested.

A backward facing step provides a classical flow containing a rapid deceleration and the introduction of turbulent eddies which will allow the characterization of drag on non-spherical particles. A backward facing step has been used in the past to validate the accuracy of CFD calculations related to turbulent flows because measurements exist

showing the recirculation zone and reattachment points as well as velocity profiles. A backward facing step of sufficient width can also be assumed to be relatively two-dimensional, thereby simplifying computational and experimental efforts. A backward facing step has also been used in the past to characterize the velocity slip of spherical particles in a two-phase flow. For these reasons, a backward facing step was selected for use in obtaining velocity slip and drag coefficient measurements on non-spherical particles.

1.1 Objectives

The primary objective of this work was to measure velocity slip and particle drag on non-spherical particles in a turbulent, decelerating flow. The data obtained represents a unique data set in that non-spherical particles have not yet been measured in a well characterized turbulent flow. Most experimental data and particle dispersion models related to a backward facing step are based on the use of spherical particles. Significant differences in the interaction of the fluid with the particle can occur due to particle shape and are therefore important in further theoretical and model development in the area of particle dispersion. This was accomplished by the following activities:

1. This research produced a detailed map of mean velocities for the gas phase through a rectangular, axisymmetric backward facing step. Three sets of measurements were made at the same locations for the gas phase to examine repeatability.

2. A detailed map of mean velocities for three different sizes of spherical particles and their corresponding slip was measured.

3. Particle velocities were obtained for four shapes including three mono-disperse sizes of non-spherical particles at a minimum of two points in the flow field. Where possible the entire flow field below the step was measured. The slip of non-spherical particles was compared with that of the corresponding spherical particles. The drag coefficients of these particles were estimated using the particle momentum equation and compared with currently excepted values.

1.2 Overview

This chapter has introduced the topic and explained the motivation for the work. The following chapters provide background information and outline the proposed research method as well as present results and conclusions. Chapter 2 is an extensive review of the research of flow behavior of particles in turbulent and non-turbulent flows including those conducted in a backward facing step. Chapter 3 provides the theory related to particle flow. Chapter 4 provides a description of the research facility, the set-up for selected measurement techniques and analysis procedures. Results are shown and discussed in Chapter 5 followed by summary, conclusions and recommendations in Chapter 6.

2 Literature Review

Many experiments using spherical particles have been performed to help study particle dispersion and flows in various geometries and situations. This research includes the effect of particle size, distribution and concentration on particle dispersion (Asia et al., 2002; Sommerfeld, 1990), particle dispersion in a turbulent mixing layer (Hishida, Ando and Maeda, 1992), particle measurements in a coaxial jet flow (Wang and Stock, 1993), vortex pairing in two-way coupled particle laden mixing layers (Kiger and Lasheras, 1995; Wallner and Meiburg, 2000), dissipation due to particle/turbulence interaction in a two-phase, turbulent shear layer (Kiger, Lasheras, 1997), and particle dispersion in a vertical round sudden-expansion flow (Hardalupas, Taylor and Whitelaw, 1992).

Another useful geometry in the study of particle dispersion/flow is the backward facing step. The backward facing step is valuable because it is often used as a benchmark in validating a computer code before its further development with more complex geometries. A good example of this is where Liou and Singh (1998) describe a numerical model for turbine coolant passage flows where the code is validated with flows of increasing physical complexity, beginning with a backward facing step.

Although most experiments in a backward facing step for both one and two phase flows have been performed in two-dimensional flow geometries, where only two of the three vector components of velocity have been measured at any one time, there have been

some three-dimensional experiments performed where the three vector components are measured instantaneously. Two of these experiments were performed by Shih and Ho (1994) and by Kasagi and Matsunaga (1995) with water as the carrier fluid with tracer particles used to track the flow. One of these experiments showed for a small aspect ratio (AR) < 10, where AR is defined as the ratio of channel width to step height, that the reattachment and the flow in the recirculation zone can be highly three-dimensional. Although this was performed in water, it could have a similar effect when air is used as the carrier fluid with a small AR. However, a later study by Benedict and Gould (1998) with air through a backward facing step suggests that significant three-dimensional effects are present in all backwards-facing step flows, even those with AR's above 10, but that turbulence statistics are independent of aspect ratios for AR $\geq$ 4.

One of the most well known experiments related to particle dispersion in a backward facing step is that of Ruck and Makiola (1988) using a Laser-Doppler Anemometer (LDA). In this experiment 1 μm oil particles were used to measure the fluid velocity of air along with approximately spherical starch particles of diameters ranging from 15 to 70 μm. The velocity of the oil droplets which were assumed to be the same as the air was compared to the starch particles of increasing size. Two different Reynolds numbers were used, namely Re=15,000 and Re=64,000 based on step height. The main results of this research showed that with increasing particle size and Reynolds number, the particle velocity field differs increasingly from the flow velocity field of the continuous phase. However, this study also showed that the velocity field differed more significantly by size.

Another aspect that should be considered when measuring particle dispersion in a two-phase flow is the effect of the particles on the carrier fluid. One experiment addressing the issue of the effect of particle loading on turbulence in a backward-facing step is that of Fessler and Eaton (1999). In this paper various spherical particles and particle loadings were used to determine their effect on modifying turbulence. Mass loadings between three and forty percent using three different particle classes (90 and 150 μm diameter glass and 70μm copper spheres) were measured using LDA. Attenuation of the turbulence of up to 35% was observed for a 40% mass loading of the largest particles.

Several numerical studies (Zhou and Leschziner, 1997; Lu, Fontaine and Aubertin, 1992; Morgan and Barton, 2000) have used the results of Ruck and Makiola (1988) to validate their two-phase CFD based models. The resulting models of these studies generally show good agreement with the experiments of Ruck and Makiola (1988). All these studies assumed spherical particles in the modeling like that in Ruck and Makiola's (1988) experiment.

The modeling of turbulent particle dispersion has also been the subject of several recent papers. McAndrew, Coppen and Rogers (2001) present a quasi-numerical technique that uses a laser Doppler anemometer probe mounted on a two-dimensional traverse to track the path of an emulated particle through a turbulent backward-facing step flow. Although all these papers referenced provide valuable insight and information to the dispersion and flow of spherical particles, no literature was found dealing specifically with non-spherical particles through a backward facing step. Having data for different shaped particles could be useful in predicting the behavior of the particle flow in situations where the particles are non-spherical. In related areas, several researchers have

investigated the effect of particle shape on drag. Most of this work consists of the development of formulas to predict the drag coefficient for particles of various shapes in a stationary fluid. Examples include Hartman, Trnka and Svoboda (1994), Ganser (1993), Haider and Levenspiel (1989), Swamee and Ojha (1991) and Tran-Cong, Gay and Michaelides (2003). All of these researchers show a significant influence of particle shape on drag coefficient. The effect of shape on drag and the methods for determining the drag are also given by Clift, Grace and Weber (1978). Since non-spherical particles have different drag coefficients, the changes in interaction with the fluid should be significant. Although research has been done on the drag of non-spherical particles, very few experiments have been attempted to document how the particle's shape affects the flow. An exception to this is research that has been done on free-falling non-spherical particles in the atmosphere (Klett, 1995) where a theoretical investigation was made on predicting the orientation of falling non-spherical particles in the atmosphere and the work of Black (1997), comparing the flow behavior of spherical and non-spherical particles in a confined geometry.

In Black's (1997) research he completed several different projects in conjunction with his dissertation. One of these projects was measuring particle size, velocity, and concentration in both a coaxial jet flow and a swirling flow through a cylindrical chamber using both spherical and non-spherical particles. His results showed a significant difference in the flow characteristics between the spherical versus non-spherical particles. However, since then the results of his measurements for the non-spherical particles have been shown to be questionable since his measurement techniques permitted serious small particle bias. Additionally, while the data generated by Black (1997) involves non-

spherical particles, the flow through the cylindrical chamber introduces swirl which is difficult to model numerically and therefore produces too much uncertainty in the fluid modeling to allow an evaluation of the particle modeling.

A review of laser-based particle measuring methods has also been previously completed by Black, McQuay and Bonin (1995), including the laser-based instrumentation for particle analysis available at BYU. The review of the literature related to the behavior of non-spherical particle flow in a backward-facing step shows that there is a need for measurements to be made in order to develop and validate existing computer models and provide valuable information regarding the flow behavior of non-spherical particles.

Additionally, there is evidence showing that a turbulent fluid can significantly increase the drag coefficient of particle especially for non-spherical particles. While very little literature is available discussing the effects turbulent fluids have on the drag on particles, Brucato, Grisafi and Montante (1998) studied the effects that turbulence had on the settling velocities of particles versus that in a still fluid. In their experiment they were able to measure the average particle drag coefficients in a turbulent media by means of a suitable residence time technique of the settling velocity exhibited by a cloud of particles. The data they obtained confirmed that free stream turbulence can significantly increase or decrease a particle's drag coefficient when compared with a still fluid without free stream turbulence.

3 Theory

A widely used commercial computational fluid dynamics (CFD) code, Fluent (2005), has a model to describe the dispersion of non-spherical particles in multiphase flows. In this program, one of two different approaches to model the turbulent dispersion of particles may be selected. These two models are: (1) the stochastic discrete particle approach and (2) the cloud representation of a group of particles about a mean trajectory. The second approach used in Fluent has been incorporated based on the work of other investigators such as Baxter (1989) and Shirolkar (1996)

In the cloud model, the turbulent dispersion of the particles (the cloud) is tracked about its mean trajectory using statistical methods. The mean trajectory is calculated from the ensemble average of the equation of motion for the particles represented by the cloud. The distribution of the particles in the cloud is tracked by a probability density function based on the cloud's position relative it's mean center trajectory. The probability density function is assumed to be Gaussian.

In this Fluent (2005) model and others it requires an estimate for the coefficient of drag (C_D) of the particles used in the equation of motion or particle momentum equation. The momentum equation used to track the mean trajectory is given by the equation 3.1.

$$\frac{du_p}{dt} = F_d(u - u_p) + \frac{g_x(\rho_p - \rho)}{\rho_p} + F_x \qquad \textbf{(3.1)}$$

Where: $F_d(u-u_p)$ is the drag force per unit particle mass and F_d is given by equation 3.2 Fluent (2005).

$$F_d = \frac{1}{2}\rho(u-u_p)C_D A = \frac{18\mu}{\rho_p d_p{}^2}\frac{C_D \mathrm{Re}}{24} \qquad \textbf{(3.2)}$$

Here, u is the fluid velocity, u_p is the particle velocity, μ is the viscosity of the fluid, ρ is the fluid density, ρ_p is the density of the particle, and d_p is the particle diameter, Re is the relative Reynolds number, which is defined as:

$$\mathrm{Re} = \frac{\rho d_p |u-u_p|}{\mu} \qquad \textbf{(3.3)}$$

For spherical and non-spherical particles Equation 3.4, by Haider and Levenspiel [1989] , based on a curve fit of empirical data of particles in a stationary fluid is used for the calculation of C_D. The equation for C_D is as follows:

$$C_D = \frac{24}{\mathrm{Re}}(1 + b_1 \mathrm{Re}^{b_2}) + \frac{b_3 \mathrm{Re}}{b_4 + \mathrm{Re}} \qquad \textbf{(3.4)}$$

Where:

$$b_1 = \exp(2.3288 - 6.4581\phi + 2.4486\phi^2)$$

$$b_2 = 0.0964 + 0.5565\phi$$

$$b_3 = \exp(4.905 - 13.8944\phi + 18.4222\phi^2 - 10.2599\phi^3)$$

$$b_4 = \exp(1.4681 + 12.258\phi - 20.7322\phi^2 + 15.8855\phi^3)$$

The shape factor, ϕ (sphericity), is defined as:

$$\phi = \frac{s}{S} \tag{3.5}$$

Where *s* is the surface area of a sphere having the same volume as the particle, and *S* is the actual surface area of the particle. The d_p used in the previously mentioned equations is the diameter of a sphere having the same volume as the particle.

The F_x in Equation 3.1, represents all the other forces per unit mass except for the steady-state drag and gravity. Where:

$$F_x = \underbrace{K_m \rho_p V_p \frac{d}{dt}(u - u_p)}_{\text{Virtual mass}} + \underbrace{\frac{K_B d_p^2 (\pi \rho \mu)^{\frac{1}{2}}}{4} \int_{t_0}^{t} \frac{\frac{d}{dt}(u - u_p)}{(t - t_1)^{1/2}} dt_1}_{\text{Bassett force}}$$

$$+ \underbrace{\frac{\pi}{8} \rho d_p^3 \omega_p (u - u_p)}_{\text{Magnus Force}} + \underbrace{1.61 (\mu \rho)^{\frac{1}{2}} d^2 (u - u_p)(u)^{\frac{1}{2}}}_{\text{Saffman Force}} + \underbrace{V_p p}_{\text{Buoyancy}}$$

As mentioned in the research of Baxter (1989) these forces are usually small in comparison with that of steady state drag and can often be eliminated to provide a reasonable approximation. In fact, an order-of-magnitude estimate indicates that over ninety percent is attributed to the steady state drag force.

The virtual-mass which accounts for inertia of the gas a particle displaces when it is accelerating is usually less than 1%. However, since the particle is not always accelerating during its lifetime its overall contribution is even less than this amount.

The Bassett force accounts for the non-steady portion of particle drag. The Bassett force usually contributes less than 0.1% of the total force during particle acceleration and vanishes altogether as the flow approaches steady state.

The Magnus force accounts for forces which act on rotating particles in non-rotating gases. In most applications, the Magnus force contributes less than 0.1% of the total force on the particle.

The Saffman force accounts for the force induced on a particle by a gradient in the local gas velocity. This force is usually negligible for most situations, contributing an estimated 10^{-6} % of the total force.

The Buoyancy force accounts for differences in the pressure forces on the particle. This term is typically less than 0.1% for particles with a density significantly greater than that of the gas phase.

Lastly, particle weight is usually the second largest contributor to the total force. Typically the contribution of weight to the total force is about 5%.

Therefore, the elimination of all forces except drag can be justified as a reasonable approximation since the drag accounts for over 90 percent of the total force and the fact that particle motion is dominated by gas phase velocity fluctuations.

As previously mentioned, the C_D used in the Fluent model for spherical and non-spherical particles is based on an empirical curve fit by Haider and Levenspiel (1989) in a stationary fluid or a non-turbulent medium. Although the particle Reynolds numbers for the curve fit is large enough to represent local turbulence, the fluid itself is not turbulent. While past assumptions haven't differentiated between the two situations, current

research has shown evidence that there could be a difference. In this research in order to evaluate whether or not there is a difference, a method for estimating the C_D was necessary.

Since as shown earlier the significant forces associated with particles in a flow are due to mainly inertial and drag the particle momentum equation can be simplified as shown by Equation 3.6.

$$m\frac{du_p}{dt} = \frac{1}{2}\rho(u-u_p)^2 C_D A \qquad \textbf{(3.6)}$$

Solving for C_D equation 3.6 becomes:

$$C_D = \frac{2m\frac{du_p}{dt}}{\rho(u-u_p)^2 A} \qquad \textbf{(3.7)}$$

A first order approximation yields:

$$du_p \approx \Delta u_p = u_{p2} - u_{p1}$$

and

$$dt \approx \Delta t \approx \frac{\Delta y}{\frac{u_{p2}+u_{p1}}{2}}$$

Where the m in equation 3.7 is the mass of the particle, A is typically the cross sectional area of the particle perpendicular to the flow, ρ is the density of the air (gas phase) and u is the velocity of the air (gas phase). The $u_{p2} - u_{p1}$ used to approximate the du_p in Equation 3.7 was the difference in particle velocity measured between two different

points a distance of $\Delta y = 0.50$ inches a part on the same streamline. The formula for $\frac{\Delta y}{\frac{u_{p2}+u_{p1}}{2}}$ used to approximate dt in equation 3.7 was calculated by dividing Δy by the average of the two different particle velocities u_{p2} and u_{p1}.

To validate whether it makes a difference in the drag coefficient for a particle flowing through a stationary fluid versus a turbulent fluid both having similar Reynolds numbers, the particle velocities were measured in still air once they reached their terminal velocity. This was similar to the methods used in Haider and Levenspiel (1989) except they used glycerin instead of air as the fluid.

If a particle is dropped through still air, the velocity of the air u is zero. Furthermore, if the particle has reached terminal velocity $\frac{du_p}{dt}$ will be zero and gravity becomes significant and Equation 3.7 becomes:

$$mg = \frac{1}{2}\rho u^2 C_D A \qquad \textbf{(3.8)}$$

If Equation 3.8 is rewritten to isolate C_D it becomes:

$$C_D = \frac{2mg}{\rho u^2 A} \qquad \textbf{(3.9)}$$

As an approximate check to see the maximum distance necessary to obtain terminal velocity, Equation 3.9 was numerically evaluated. Figure 3.1 shows the results

of the numerical evaluation of Equation 3.9 for velocity versus distance for the particles that take the longest distance to achieve terminal velocity. The distance used to take the measurements in this research greatly exceeded these values. Therefore, it was determined that terminal velocity was acquired by the time the particles had reached the measurement location.

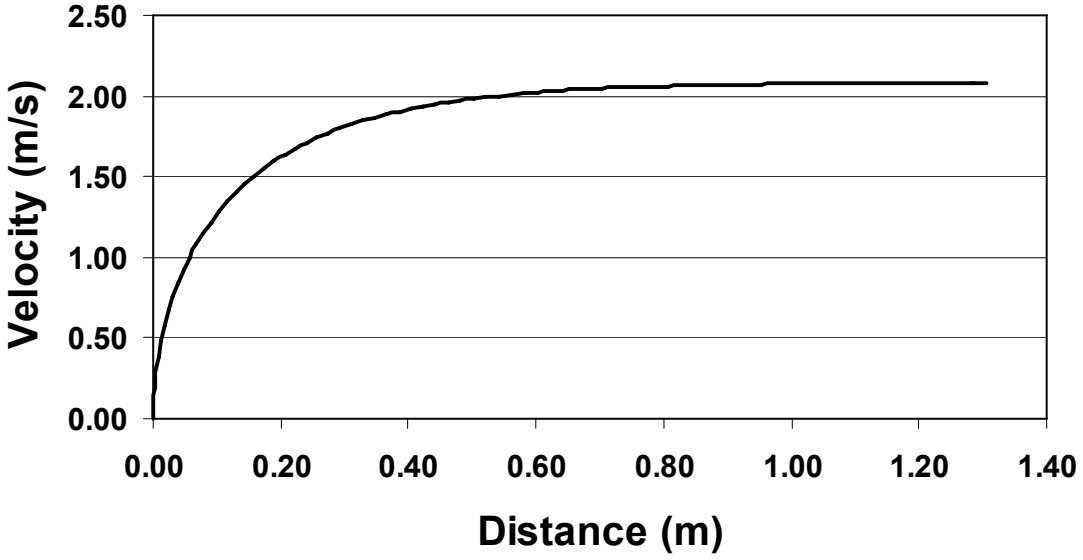

Figure 3-1 Graph showing when terminal velocity is reached.

4 Method

Achieving the stated objectives required the following: 1) a facility to observe the velocity of the particles; 2) equipment and instrumentation capable of measuring the particles; 3) the measurement matrix with the sizes, shapes and locations for the various particles used in the research; and 4) the use and preparation of the different particles and technique for measuring the proper size distribution of the particles. Each topic is addressed in the following sections.

4.1 Backward Facing Step Flow Facility

A simplified geometry commonly used to validate the accuracy of fluid dynamic models is that of a backward facing step. A backward facing step is often used because it contains key elements of a realistic flow such as turbulence and a change in geometry without the complexities of swirl. To make particle velocity measurements a backward facing step flow facility was constructed out of acrylic with removable panels for easy cleaning access, modifications, and repairs. This new facility is shown in Figure 4.1 and 4.2. This backward facing step was designed to have a maximum Reynolds number of 22,000 based on step height and flow velocities from -3.5 to 16 m/s. An important purpose of this facility, along with gaining a fundamental understanding of these types of flows, is to obtain accurate experimental data for model validation. This facility has been built with a high degree of optical access that provides the capability to measure particle

information within very tightly controlled conditions. To ensure that accurate measurements were made with low distortion of the laser beam, thin windows made out

Figure 4-1 Backward facing step facility.

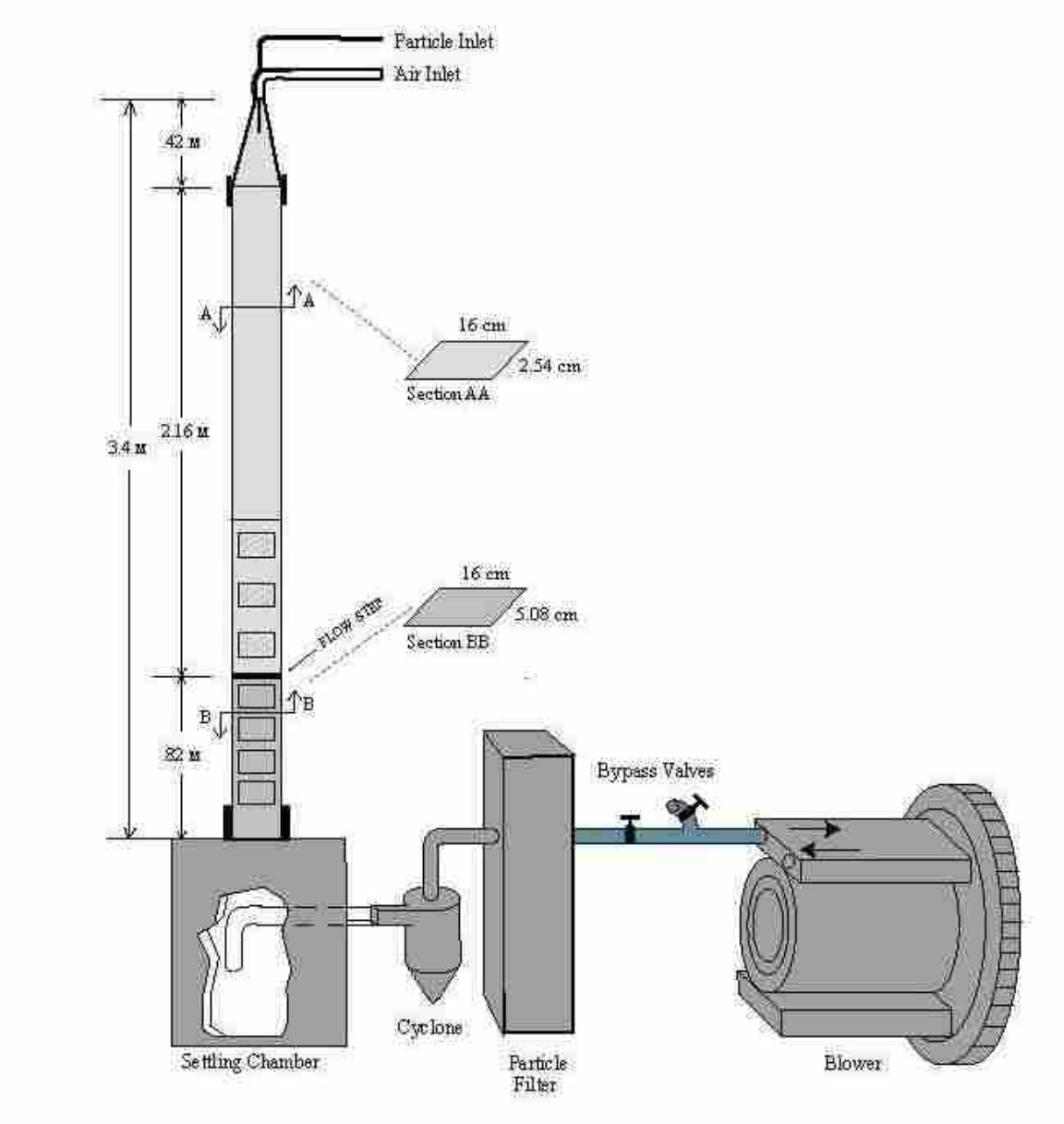

Figure 4-2 Drawing of backward facing step facility.

of glass .01016 cm (0.004 in.) thick were strategically placed in several locations of the flow facility to map velocity profiles.

The backward facing step facility was mounted on top of a settling chamber to maintain an even velocity distribution across the exit. Air was pulled out of the settling chamber by a Rotron model 707R blower which was matched to the incoming air flow rate in order to maintain atmospheric pressure within the measurement volume. This not only avoided breakage of the thin glass windows, but also eliminated undesirable crevice flow which might influence the desired flow-field. A manometer was used to adjust the operating flow rate to equilibrate the pressure. Airflow was extracted from the settling chamber through an inverted 90 degree elbow in order to pull air more evenly from the settling chamber to avoid distorting the velocity profile at the exit of the facility. The air and particles then passed through a cyclone particle separator and filter to remove the particles before passing through the blower.

Because the blower was not variable speed, the amount of air passing through the blower was fixed. To control the pressure in the chamber, as shown in Figure 4.2 a bypass route was installed with a valve allowing the blower to draw adjustable amounts of room air.

Figure 4.3 shows the PDPA sending and receiving unit positioned down stream of the step. The PDPA used in this research was an Argon-ion laser manufactured by Aerometrics. The sending optics (transmitter) is on the left side of the photograph and is mounted parallel to the window. The receiving unit is also on the left and mounted at a 30° angle relative to the beams passing through the measurement volume. The configuration of the laser shown in figure 4.3 is in the backscattering direction. When the

transmitter is mounted on the other side of the receiver this is what's called the forward scattering direction. Two pairs of beams traverse the measurement chamber. One pair is oriented vertically and measures the velocity in the vertical direction. The second pair is horizontal and measure velocity in the right to left direction as viewed from the sending unit. The velocity component in the direction of the laser beams is not measured. The high level of optical accessibility and the ease of operation of this facility made it ideal for investigating the effects of particle shape on velocity and slip.

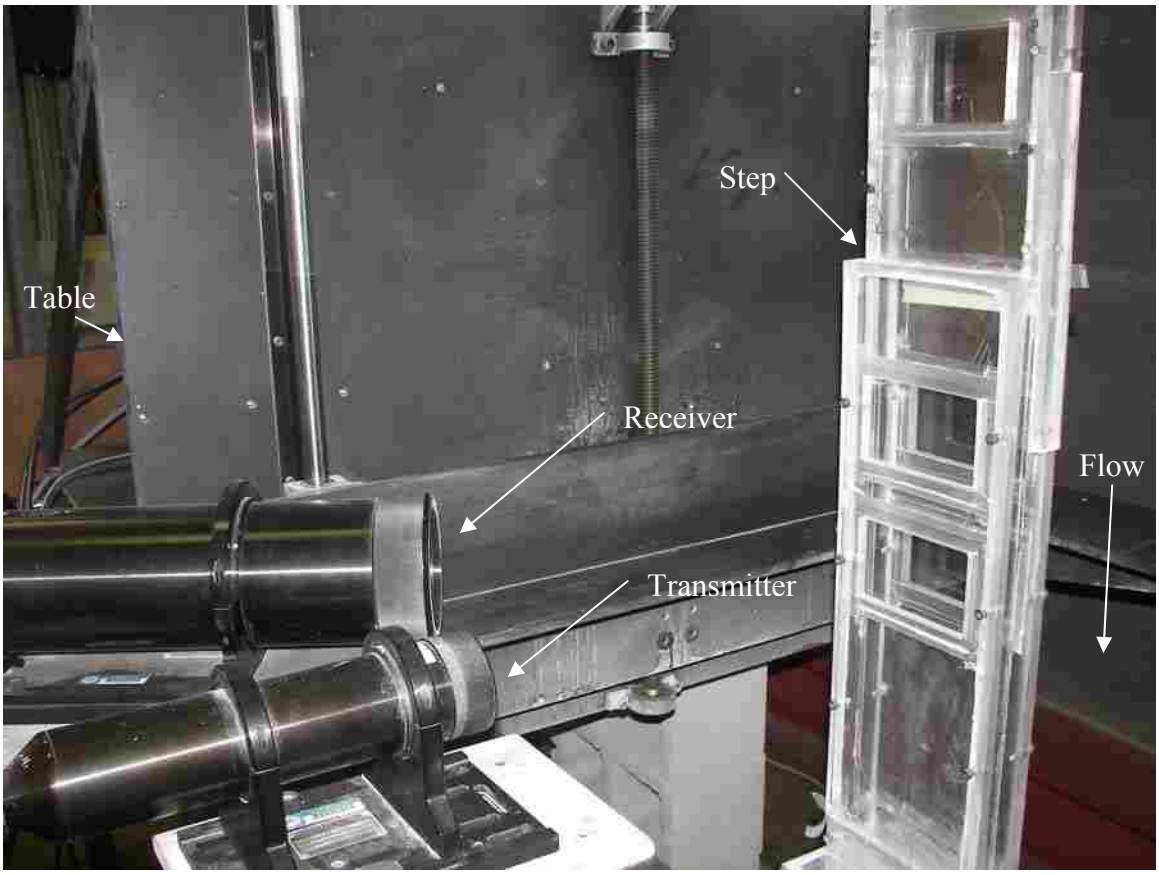

Figure 4-3 Laser setup for measurements through optical windows.

Upstream of the flow facility, dried air was supplied to the chamber by a large tank of compressed air and supplied by a compressor. A choked-flow orifice with a pressure transducer was used to determine the airflow to the chamber. The pressure transducer was connected to a multimeter calibrated to relate the millivolt output of the transducer per the given load to the corresponding pressure reading on the meter. Using a choke flow orifice requires only a single upstream pressure measurement to determine the flow rate along with the temperature of the air once the flow is choked at the orifice. Accuracy using a choke flow orifice for flow measurement is very good, on the order of 2%. The flow rate for the choked-flow orifice was determined using the following equation (Ower and Pankhurst, 1977)

$$q = \alpha a \sqrt{\frac{P^2}{RT}} \sqrt{\gamma \theta_c \frac{\gamma+1}{\gamma}} \qquad \textbf{(4.1)}$$

where α is the discharge coefficient, a is the area of the orifice, P is the measured upstream pressure, T is the upstream temperature, R is the gas constant, γ is the ratio of specific heats (1.4), and θ_c is the critical pressure ratio (0.528). The diameter used for the orifice was .250 inches. As is shown in Table 4.1, when the results of a Coriolis mass flow meter are compared with those calculated from Equation 4.2, the best minimized percent differences in the mass flow rates are found to occur with a correction factor or discharge coefficient of 0.994. The information in the table are based on 29.44°C

(85°F) since that was the temperature at the time the mass flow measurements were taken. However, all of the measurements of this research used a constant mass flow rate of 0.0467 kg/sec. based on a pressure of 551.6 kpa (80 psig) and temperature of 20°C (68°F). To maintain this mass flow rate the pressure was adjusted from the nominal pressure of 551.6 kpa (80 psig) depending on the temperature measured during the time of the tests. However, as is shown in Equation 4.1 the temperature differences must be very large to make a significant difference in the mass flow rate. For example a difference in temperature of 12.22°C (10°F) results in only a 1% difference in the mass flow rate.

Table 4.1 Minimizing the difference between the measured and calculated flow rates to find the discharge coefficient.

Pressure (kpa)	Pressure (psig)	Measured Mass Rate (kg/sec)	Calculated Mass Flow Rate (kg/sec)	Difference in Percent Between Mass Flow Rates (kg/sec)	Difference in Percent Between Mass Flow Rates After a .994 Correction Factor (kg/sec)
275.8	40	0.0259	0.0263	1.54%	0.93%
344.7	50	0.0312	0.0313	0.32%	0.26%
413.7	60	0.0361	0.0362	0.32%	0.33%
448.2	65	0.0385	0.0388	0.78%	0.18%
482.6	70	0.0409	0.0413	0.98%	0.04%
517.1	75	0.0436	0.0437	0.23%	0.37%
551.6	80	0.0459	0.0462	0.65%	0.04%

As is shown in Figure 4.4, the particles are fed into the chamber in a downward direction and mix with the chamber air flow. The particles are pulled into a funnel and through a tube by the suction created by the low static pressure created by the velocity of

the air passing through the chamber. The particles were fed into the funnel either by hand or by an Accurate model 102 volumetric feeder. In the cases where the feeder was used the feed rates resulted in a particle loading of no more than 0.12%; a mass loading which would certainly be considered a dilute flow. With some of the particles it was not possible to feed them through the volumetric feeder due to their shape and size and therefore they were fed by hand at an approximately similar loading.

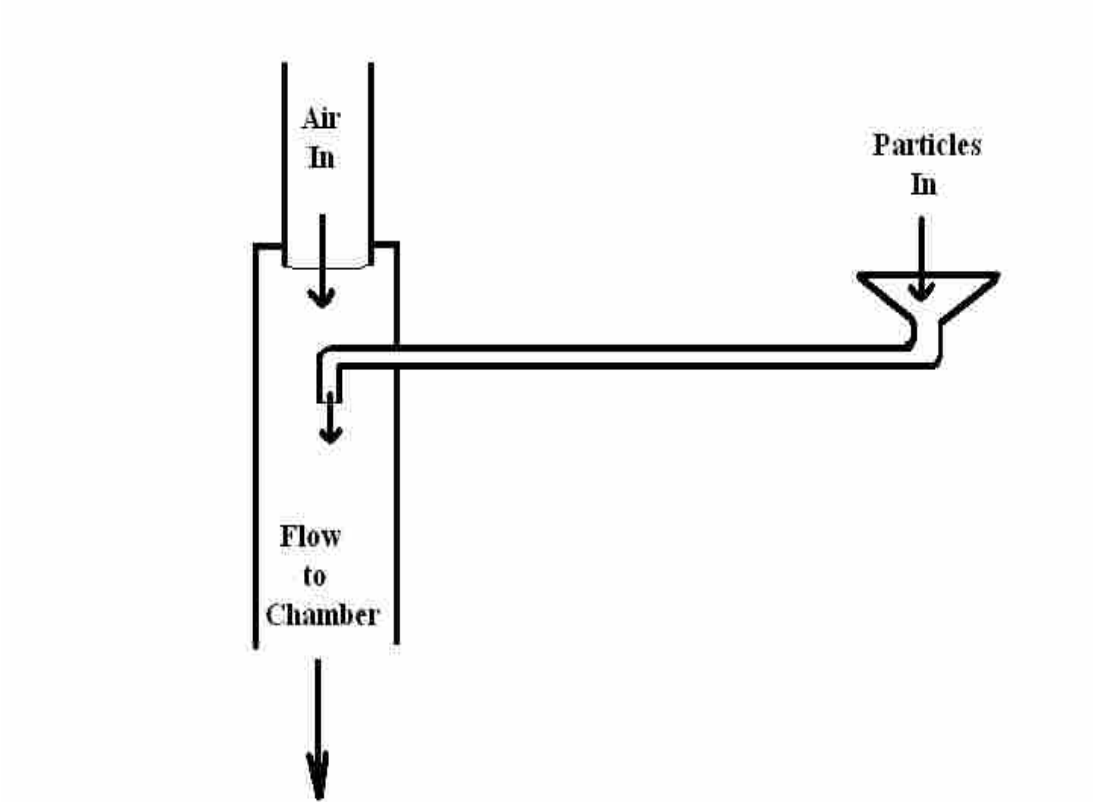

Figure 4-4 The inlet for air and particles located at the top of the chamber.

In order to place the laser at the various locations of the chamber, a three-dimensional computer-controlled positioning table was used. A diagram of this system is shown in Figure 4.5. It was essential that this table had the ability to provide the spatial accuracy necessary to take good measurements. The two important features of

this positioning system were, first, that it could hold the laser-based equipment necessary to take the measurements and second, that it was controlled by a computer and capable of moving in three dimensions. The maximum travel in the x-y directions of the table was approximately 50 cm, where the maximum travel in the z-direction was approximately 60 cm.

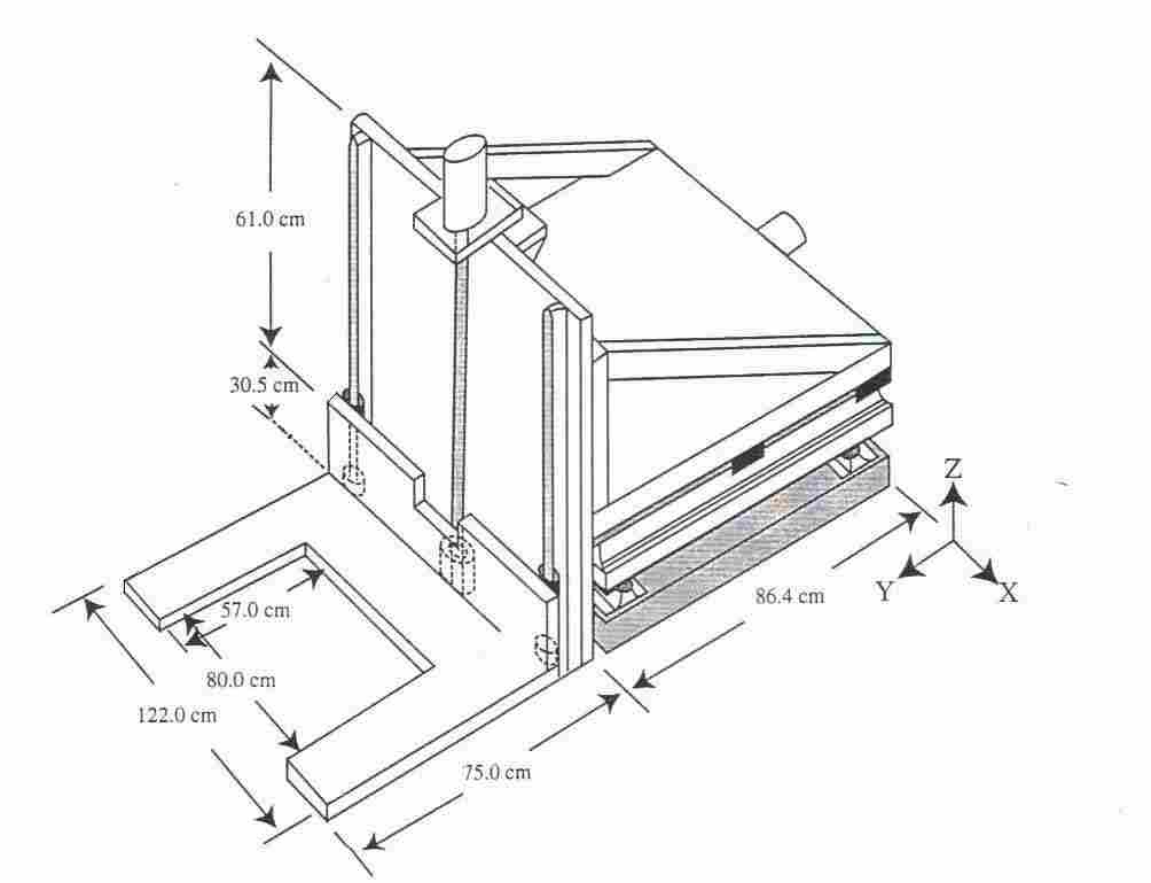

Figure 4-5 Computer controlled three-dimensional positioning table (Black 1997).

Since a larger extension in the z-direction was necessary to reach all the windows both upper and lower, a manual forklift system shown in Fig 4.6 was used in conjunction with the positioning table. The fork lift system combined with the positioning system

allowed measurements to be taken up to a vertical distance of 2 meters. The positioning table provided the capability to position the measuring volume of the laser system to within 1.0 mm.

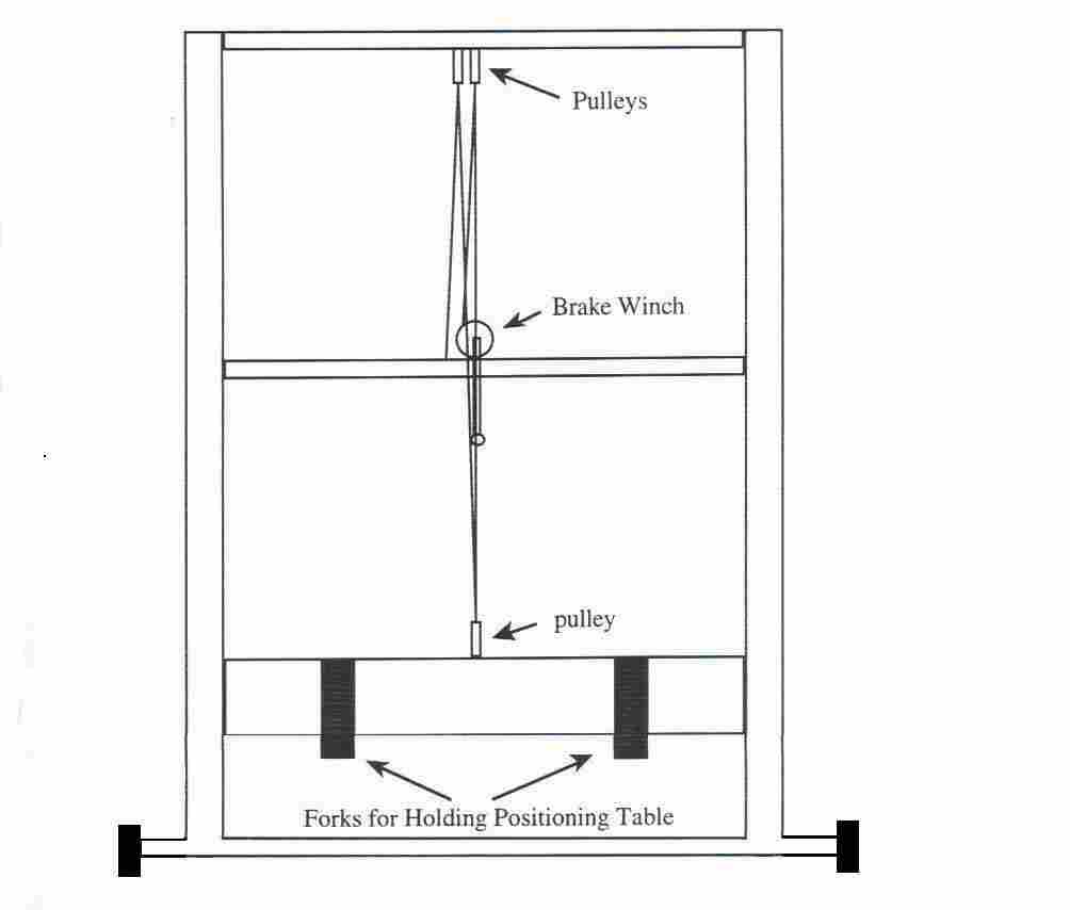

Figure 4-6 Fork lift for positioning table (Black 1997).

4.2 Equipment and Instrumentation for Particle Measurement

Completing the objectives of this dissertation required a method for measuring velocity of particles without disturbing the flow. Light or laser based diagnostics are well suited for this task. Two laser based instruments were used. Velocity measurements and the sizing of spherical particles was done using a Phase Doppler Particle Analyzer

(PDPA) and a Coulter LS100 laser diffraction particle size analyzer was used to measure the size distributions of spherical particles.

4.2.1 Phase-Doppler Particle Analyzer (PDPA)

Laser-Doppler and Phase Doppler anemometry is a well established and accurate technique for non-intrusive measurement of both velocity and spherical particle size. The PDPA requires seeded particles in the flow in order to scatter light to make velocity measurements which can then in well specified conditions be taken to equal the gas phase velocity. The principle of a Phase Doppler was first introduced by Durst and Zare (1975) and usually combines both the velocity measuring capability of the Laser Doppler along with the particle sizing capability of the Phase Doppler. Many papers summarizing the Phase Doppler technique since then have been published. Some of these include Bauckhage (1988), Durst and Naqwi (1993), and Sankar and Bachalo (1995), which provide an overview of the Phase Doppler method.

Figure 4.7 shows a diagram how the velocity measuring capability of the Laser Doppler or Laser Doppler Velocimetry (LDV) system works. In this figure, a pair of beams is shown which cross and overlap in a region called the measurement volume. This measurement volume is ellipsoidal in shape and forms a fringe pattern of alternating light and dark bands from the interference of the two light beams.

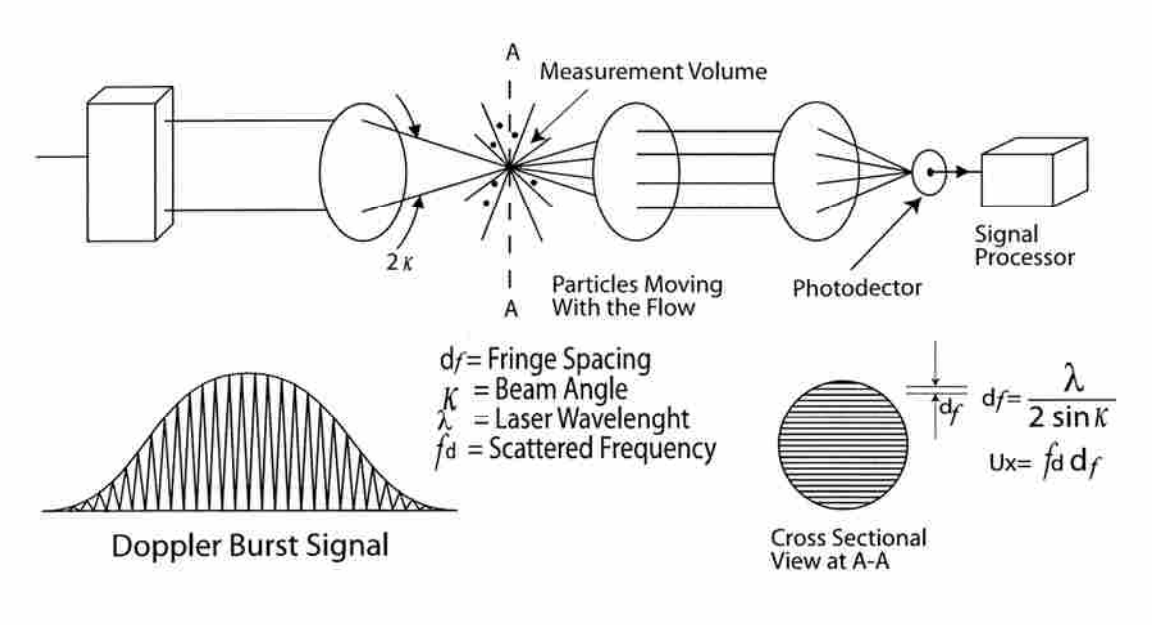

Figure 4-7 Laser velocimetry system.

As particles pass through the fringe pattern, the scattered light forms a Doppler burst signal at the detector. The higher the frequency of the light scattered by the particle passing through the fringe pattern in the measuring volume, the higher the velocity of the particle is in any one given direction. This method of describing how the Laser Doppler measures velocity is called the fringe method. A more technical way to describe this method can be explained by the Doppler principle. To measure all three components of velocity, three pairs of crossing beams with each pair having a different wavelength is required. The system used for this research emits two pairs of crossing beams and is therefore a two-component system and hence can measure two components of velocity.

When the LDV is also combined with the added feature of being able to measure the phase difference, this system is commonly called a Phase Doppler Particle Analyzer (PDPA). The measurement of particle size requires only one set of crossed beams. As

Figure 4.8 shows the sizing of particles is accomplished by extending the receiving optical system with at least two photo-detectors.

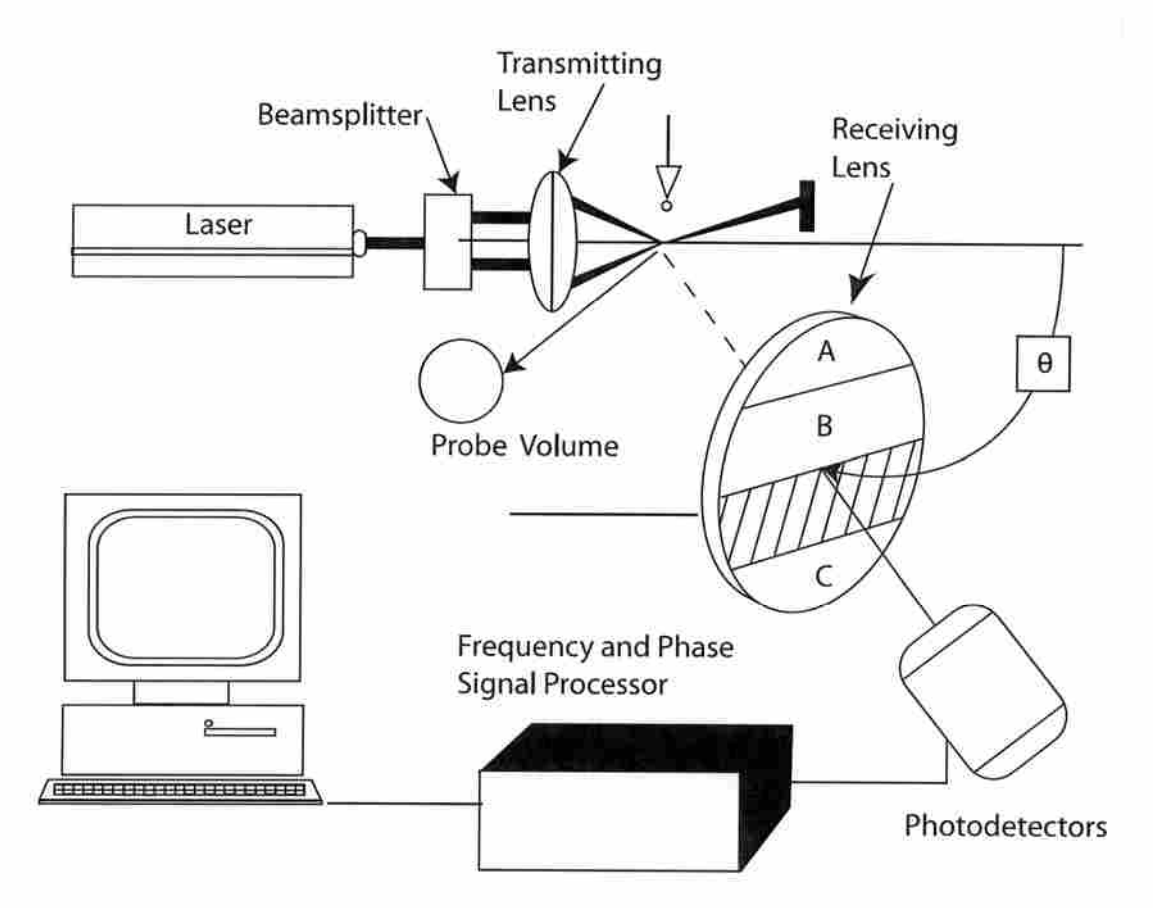

Figure 4-8 Phase Doppler system with three photo-detectors.

The measurement of particle size relies on the phase shift difference of the light scattered by refraction or reflection from two intersecting laser beams at two or more spatial locations at the photo-detector. If the particle is transparent like glass, light scattered by refraction is usually used since the intensity of the light is the highest in this mode. Whereas for opaque particles reflected light is the only mode that can be used

since it is impossible for light to be refracted through a non-transparent particle. Figure 4.9 shows the phase difference between two of the detectors.

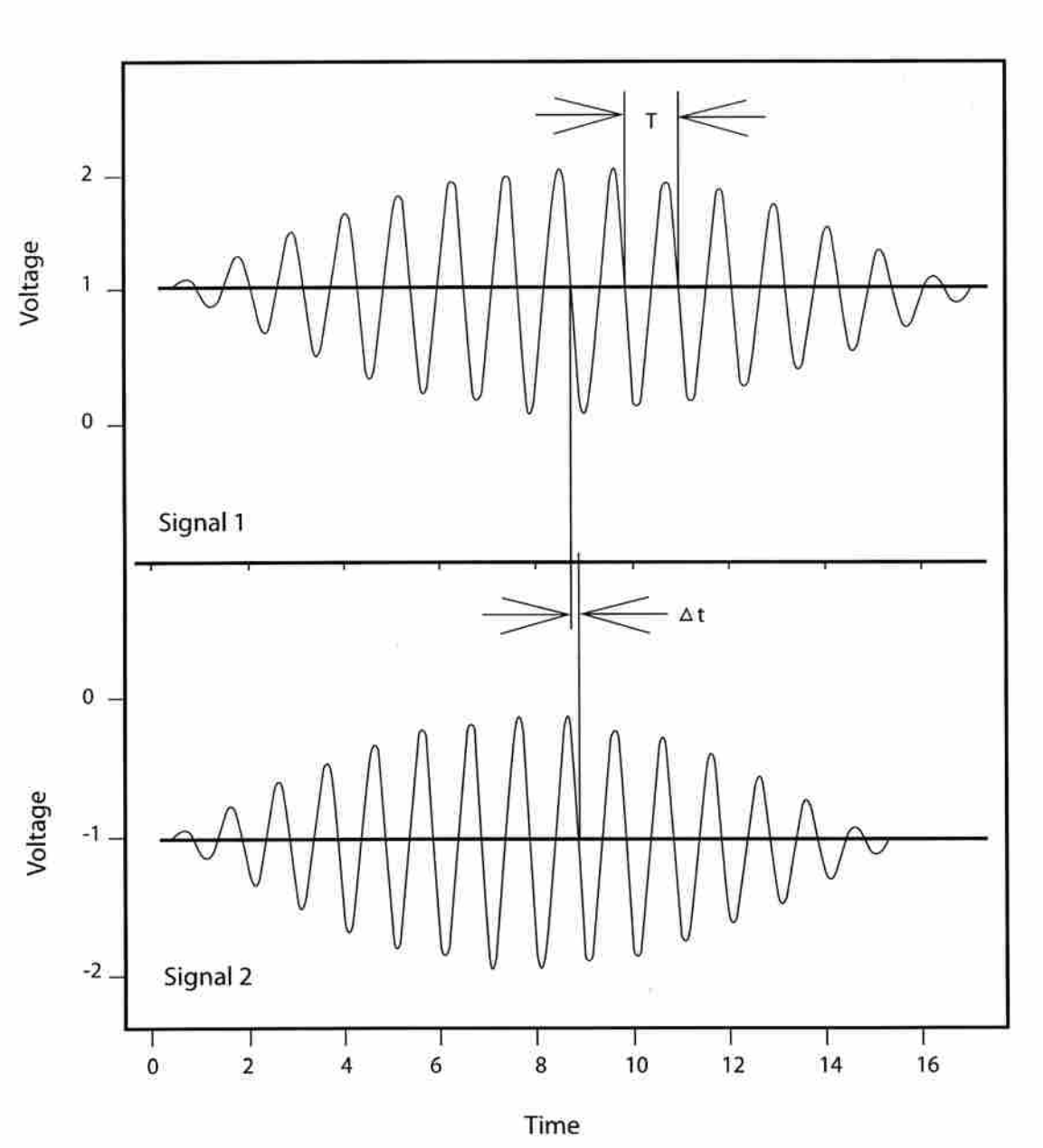

Figure 4-9 Phase shift between detectors.

Although, only two detectors are needed to measure size, three detectors provide a redundant size measurement that can be used to check for sizing accuracy. Figure 4.10 shows the instrument response for a typical PDPA system using three detectors.

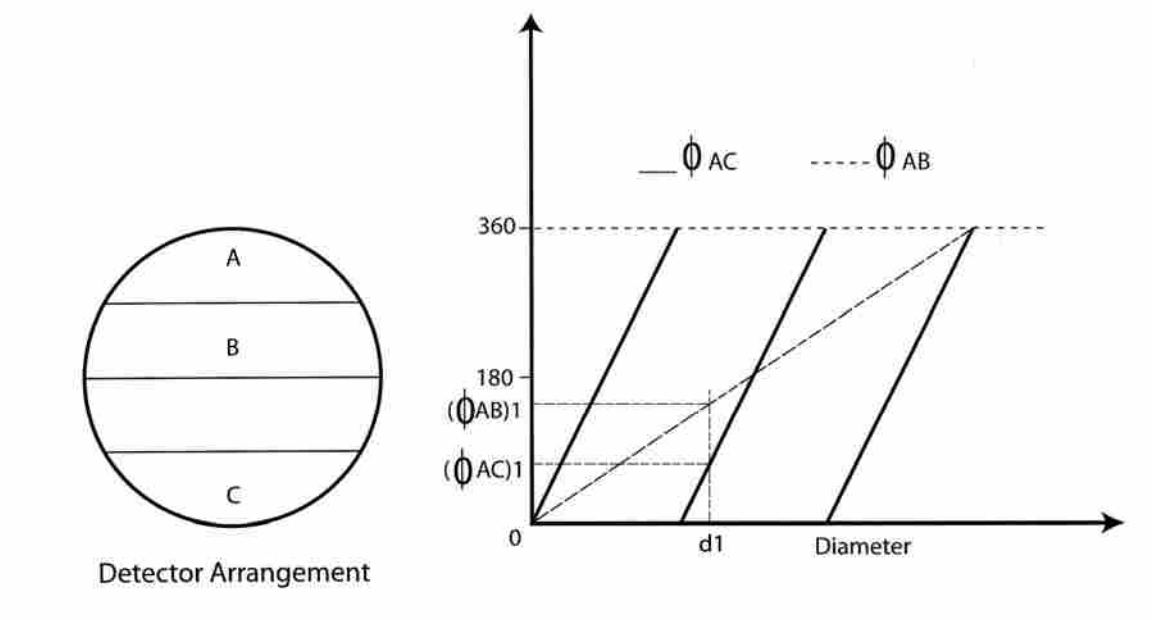

Figure 4-10 Three detector configuration.

In order for the phase difference to be related to the size, the particles must be approximately spherical since the phase shift is dependent on the radius of curvature. Figure 4.11 shows a phase shift due to the refraction of scattered light through a spherical particle.

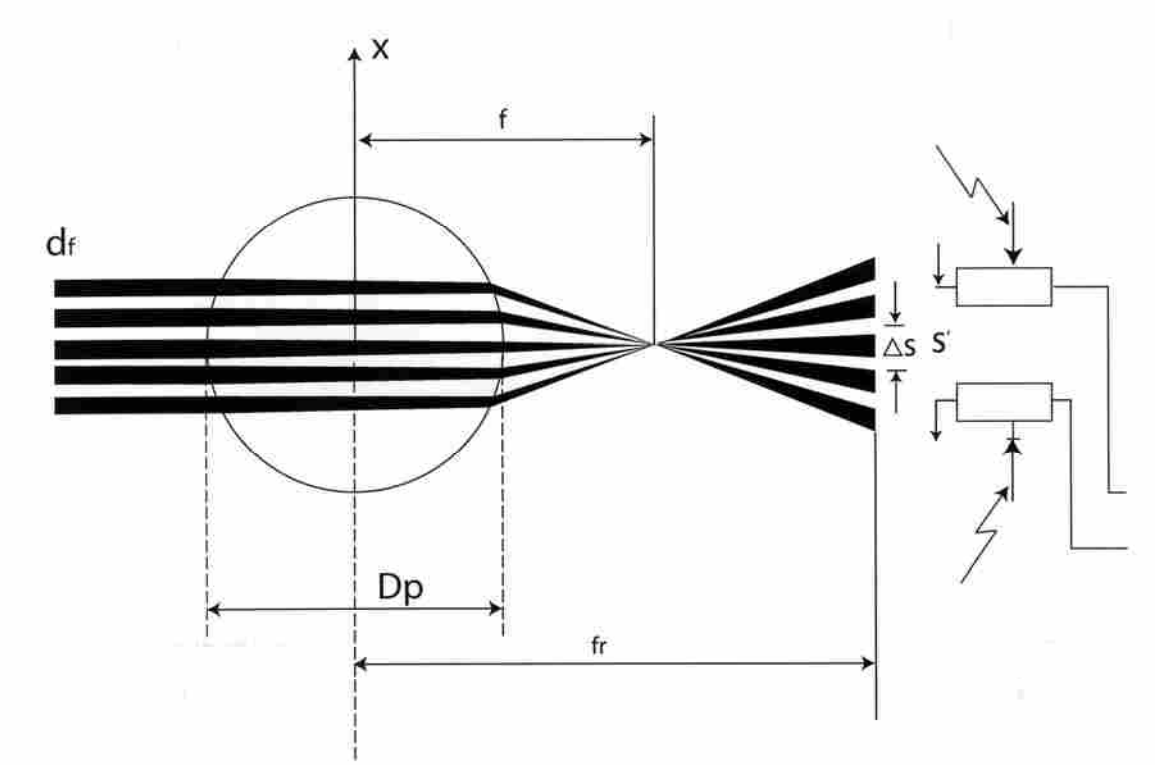

Fringe model for phase-Doppler principle for the case of refraction .

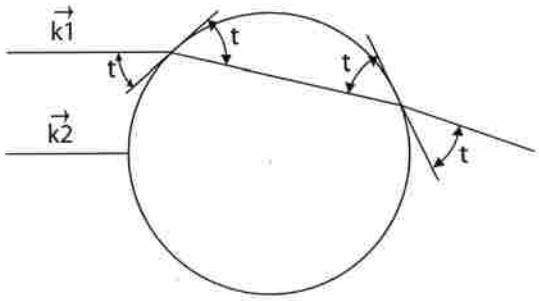

Phase difference of a light ray refracted at a spherical particle .

Figure 4-11 Phase difference of refracted light through a spherical particle.

The typical configuration for the receiving optics for most particle types is 30 degrees measured from the forward axis. For particles whose scattered light is reflective

rather than refractive, a back-scatter collection angle of 150 degrees can be used. However the best configurations are those closest to the forward scattering direction, since backscatter as shown by Hardalupas and Lui (1993), both limit the dynamic size range and sometimes create difficulties in instrument response. Additionally, the signals in the back-scatter direction are significantly lower than that of the forward configuration due to a lower amount of light being scattered in that direction. This can be somewhat compensated for by increasing the power of the laser, but this can create other problems and in general makes data collection more difficult.

Phase-Doppler is capable of measuring particles as large as several millimeters to as small as 0.5 μm in diameter; however for particles less than 10 μm there have been some concerns about oscillations in the instrument response function that can affect the instrumentation. However, Houser and Bachalo (1985) and Sankar and co-workers (1991) show that with the right selection of optics, these oscillations can be minimized and accurate measurements can be made for particles as small as 0.5 μm. For non-spherical particles the PDPA is limited to measuring velocity since the error in size measurements increases the more the particle deviates from spherical. Under the best of conditions using a PDPA, velocities can be measured to within one percent and spherical particle size to within 4 percent.

4.2.2 Coulter LS100

The Coulter LS100 is an instrument based on the Fraunhofer diffraction principle, manufactured by the Coulter Corporation. Unlike the PDPA this instrument does not measure velocity but uses an ensemble technique that measures the size distribution of a

group of particles simultaneously. The output of the size distribution of the particles is expressed as that of spheres having equivalent diameters. In other words, the average area of the projection of the particles converted to an equivalent diameter is what is really being measured.

Diffraction based instruments have been widely used in both in industry and research to measure the size distribution of both solid and liquid particles. Figure 4.12 shows a diagram of a diffraction-based sizing system like that of the Coulter system. Swithenbank (1977) was the first to develop the diffraction-based particle sizing instrumentation. In fact, it was his work which led to the development of the popular Malvern particle-size analyzers.

A diffraction based sizing system operates by passing a laser beam through particles which are dispersed in a liquid or air. The light scattered or diffracted from the particles is collected by a Fourier lens and focused on a series of detectors to measure the angular separation of the light. In general, the smaller the particles the larger the angle is of the diffracted light. By using an algorithm to interpret the angular distribution of the scattered light across the detectors the particle size distribution can be determined from the Fraunhofer diffraction theory.

Fraunhofer diffraction theory is based on plane waves scattered by a particle producing a series of light and dark bands that decrease in intensity with increasing radial position. The particle size distribution can be found by measuring the scattered light intensity at various radial locations.

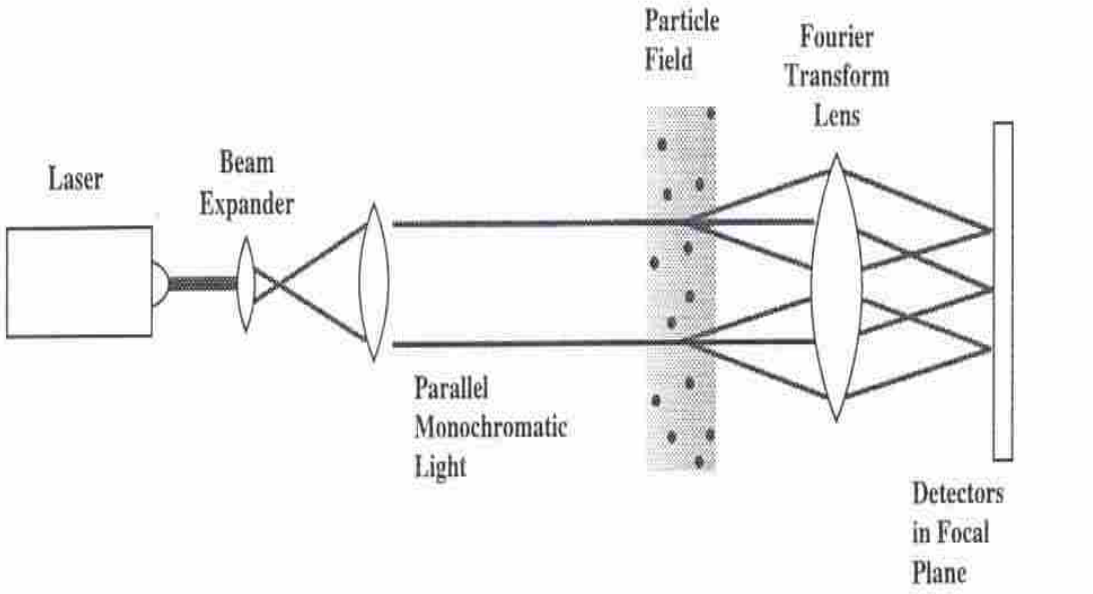

Figure 4-12 Laser diffraction particle sizing (Black 1997).

4.3 Particle Measurement Matrix

In order to relate velocity to the drag coefficient and thereby make general use for the velocity data, it was necessary to measure the velocity of the particles according to their size and shape. Table 4.2 shows the different shapes and sizes of the particles used in this research along with their measurement locations (for measurement locations see Figure 4-13). For the spherical particles the size is the diameter and for the non-spherical particles the size is based on sieve size.

Table 4.2 Table for particle shapes, sizes and measurement locations.

Particle (shape/size)	Axial Location	Thickness Location (mm)
	Steps	Increments of 2.54 mm
Spherical Seeded		
(1-10µm dia.)	(1 - 9, 12)	(2.54 - 48.26)
Spherical		
(38-45µm dia.)	(1 - 9, 12)	(2.54 - 48.26)
(45-51µm dia.)	(1 - 9, 12)	(2.54 - 48.26)
(51-63µm dia.)	(1 - 9, 12)	(2.54 - 48.26)
Gravel		
(38-45µm sieve size)	(1 - 9, 12)	(2.54 - 48.26)
(45-53µm sieve size)	(1 - 9, 12) (9.5)	(2.54 - 48.26) (35.56)
(53-61µm sieve size)	(1 - 9, 12)	(2.54 - 48.26)
(75-90µm sieve size)	(1 - 9, 12) (9.5)	(25.4 - 48.26) (35.56)
(90-106µm sieve size)	(1 - 9, 12)	(25.4 - 48.27)
(106-125µm sieve size)	(7- 9, 12)	(25.4 - 48.27)
Cylinder		
(53-61µm long) (16µm dia.)	(7.5, 8) (9, 9.5)	(43.18, 43.18) (35.56, 35.56)
(61-75µm long) (16µm dia.)	(7.5, 8) (9, 9.5)	(43.18, 43.18) (35.56, 35.56)
(106-125µm long) (16µm dia.)	(7.5, 8) (9, 9.5)	(43.18, 43.18) (35.56, 35.56)
Flakes		
(53 - 61µm sieve size) (5µm thick)	(7.5, 8) (9, 9.5)	(43.18, 43.18) (35.56, 35.56)
(106 -125µm sieve size)(5µm thick)	(7.5, 8) (9, 9.5)	(43.18, 43.18) (35.56, 35.56)
(180 - 212µm sieve size)(5µm thick)	(7.5, 8) (9, 9.5)	(43.18, 43.18) (35.56, 35.56)

Because the PDPA can not measure the size of non-spherical particles it was important to produce particles of a narrow size distribution and known shape prior to collecting the velocity data. Several different sizes and shapes of glass particles were used. These included: very small spherical seeded particles used to measure the gas phase velocity, three different sizes of spherical particles, six sizes of gravel shaped particles, three sizes of cylindrical shaped particles and three sizes of flake shaped particles.

During the course of this research the use of particles made out of biomass or saw dust was also explored. However, due to the random nature of saw dust it was found very difficult to separate enough particles in both the shape and size necessary to properly characterize them into a reasonable distribution. Also, sawdust large enough to flow differently than the gas phase was difficult for the laser system to measure since the density of wood is low and required too large a particle to produce any noticeable slip.

Figure 4.13 shows a schematic of the locations below the step where the velocities of the particles were measured. For most particles these measurements were taken at 2.54 cm (1 inch) increments from the step in the chamber until 22.86 cm (9 inches) and then at 30.48 cm (12 inches) at the front centerline in the axial direction of the chamber. Since each 2.54 cm (1 inch) equals one step size, measurements were made at a total of ten steps. At each step in the thickness direction of the chamber along the front centerline nineteen measurements equally spaced .254 cm (.1 inches or .1 steps) apart were taken at each step for a total of 190 measurements. After the tests were made with the glass panels as shown by the squares in the front view of Figure 4.13, other glass panels were installed with windows installed in a different orientation in order to take the remaining velocity measurements.

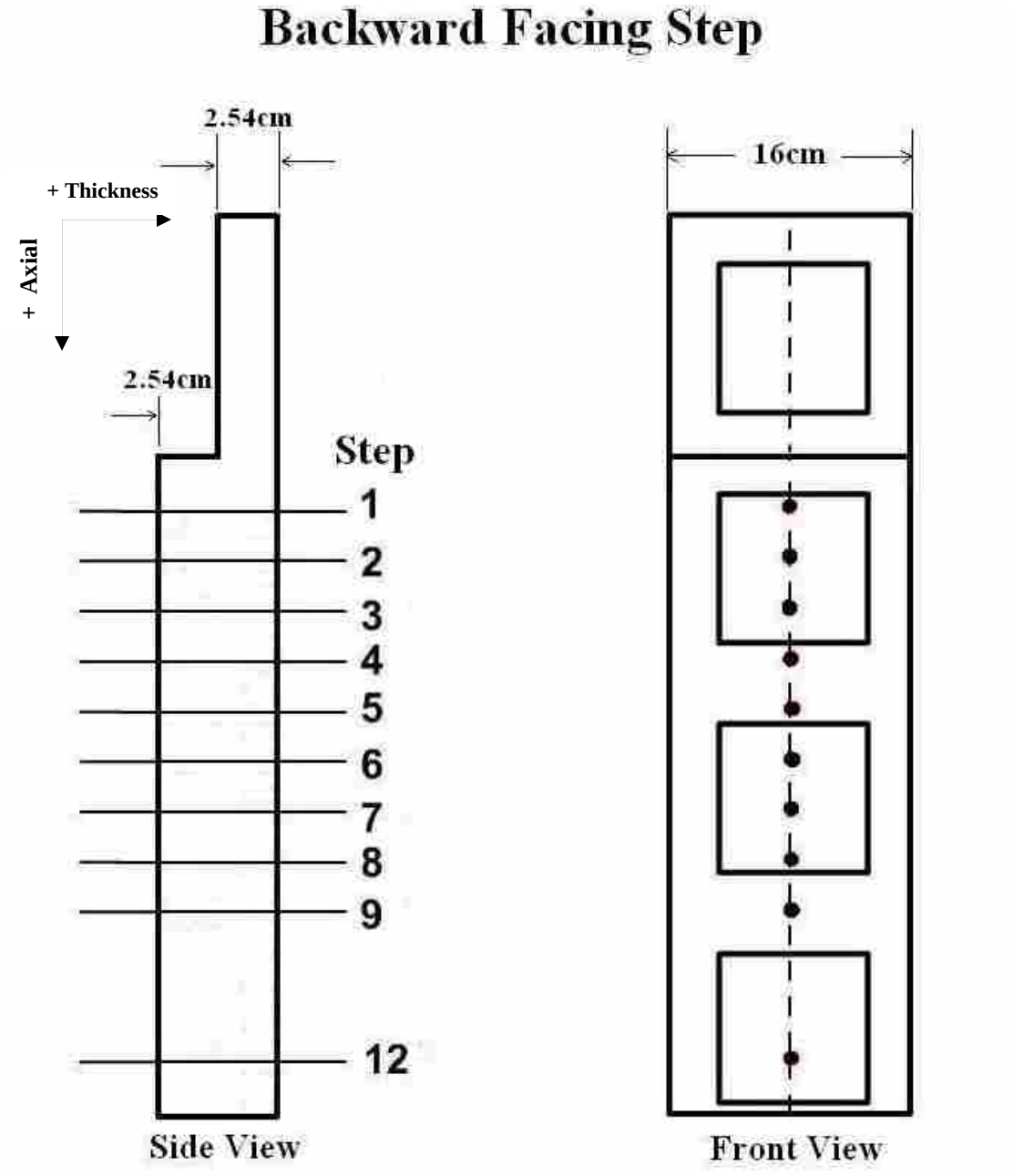

Figure 4-13 Schematic of measurement locations.

For the cases of the cylinders and flakes and some of the gravel particles, measurements were also made at fractional step sizes in order to reduce the distance between the measurements in order to provide better resolution in the drag coefficient calculations for the non-spherical particles. In addition to three measurements being made for each seeded position, three measurements were also made for each size of the cylinders and flakes at each of the locations shown in table 4.2 and for the 45-53 μm and 75-90 μm gravel particles at the 9 and 9.5th steps at the 35.6 mm depth location. Since the spherical seeded particles showed reasonable repeatability only one measurement was made at each of the locations for the spherical particles.

4.4 Biasing Problem

Since the laser measurement system used in this research could only measure the size of the spherical particles with their corresponding velocities, a method for measuring the velocity of the desired size distribution of the non-spherical particles was necessary. Without the proper preparation of the particles and using the correct techniques of measuring the non-spherical particles the results can be greatly biased.

4.4.1 Bimodal Distribution Containing Small Particles

For the small spherical seeded particles the size distribution has just one mode. Figure 4.14 shows a microscope image of these seeded particles. Additionally, Figure 4.15 shows the size distribution of these particles. Therefore, these particles do not have a bimodal size distribution. However, for the larger spherical particles and all the non-spherical particles they have an inherent bimodal size distribution which is impossible to

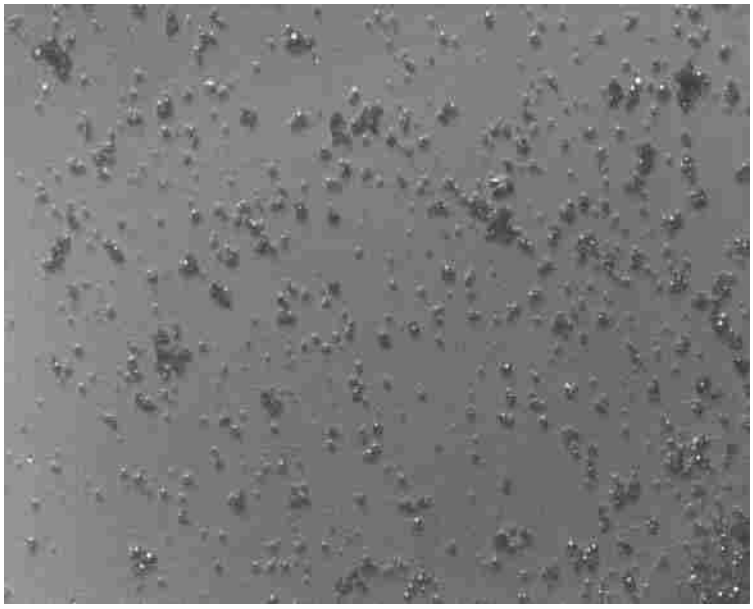

Figure 4-14 Microscope image of spherical seeded particles.

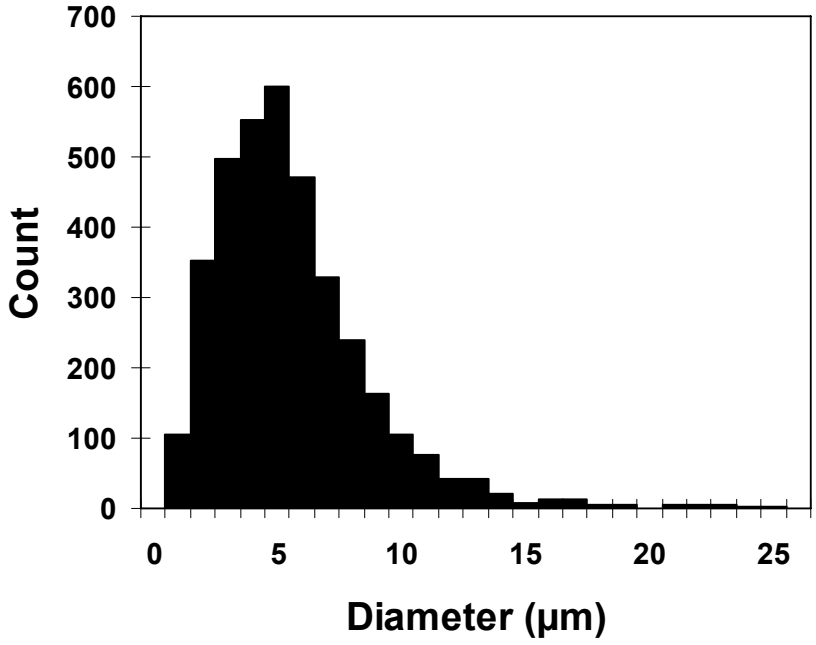

Figure 4-15 Seeded particle size distribution.

eliminate regardless of the amount of preparation done on these particles due to the difficulty of removing the smaller particles from these larger ones.

While the bimodal size distribution doesn't present a problem for the larger spherical particles since the PDPA system can measure both the size and velocity of spherical particles, it does serve to illustrate the bimodal size distribution problem associated with the measurement of non-spherical particles. Two main problems exist with particles having a bimodal size distribution:

First, it is difficult to totally eliminate all the small particles that are mixed in with the larger particles. Figure 4.16 shows the volume percent of the 38–45 μm spherical particles. In this figure it shows a histogram of the size distribution in volume percent measured by the Coulter particle size analyzer of these particles. As can be seen in the histogram, even though the glass beads have been sieved four times there are still two different size distributions, a smaller one between 5 and 12 μm and a larger one between 30 and 68 μm. While most of the particles by volume percent are closer to the 38 to 45 μm range, the number percent of particles is quite different. Figure 4.17 shows a histogram of the same particles except the graph measures the number percent of particles instead of volume percent. In this case there are a lot more of the smaller 5 to 12 μm particles. This adds a serious complication in trying to achieve a mono-disperse size distribution measurement for non-spherical particles since the laser system measures the quantity of the particles the analyzer detects (the smaller particles) rather than the larger ones that are intended to be measured. Since there are usually more small particles then the larger ones this tends to bias the measurements toward the smaller sizes. This can then greatly misrepresent the actual physics of the flow and give erroneous results.

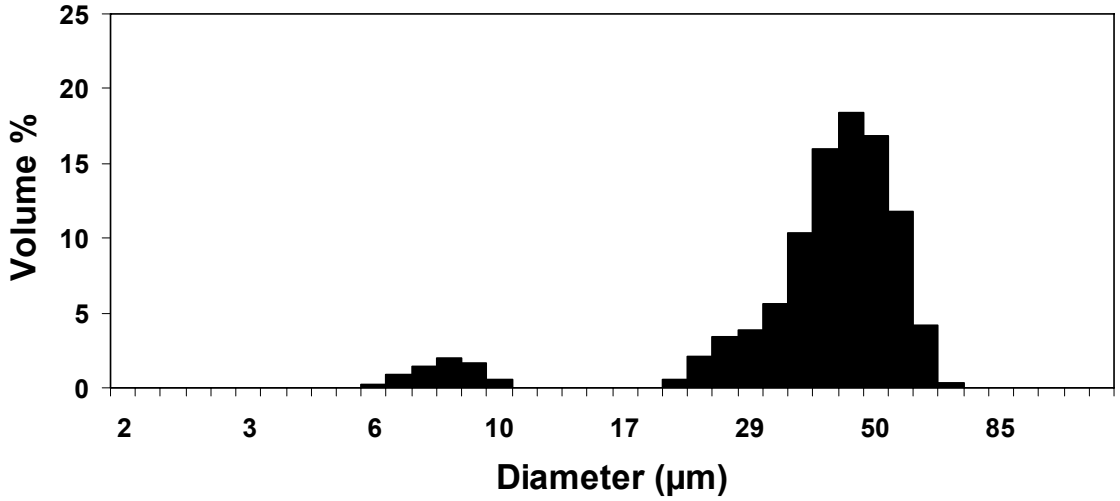

Figure 4-16 Volume percent of the 38–45 µm spherical particles.

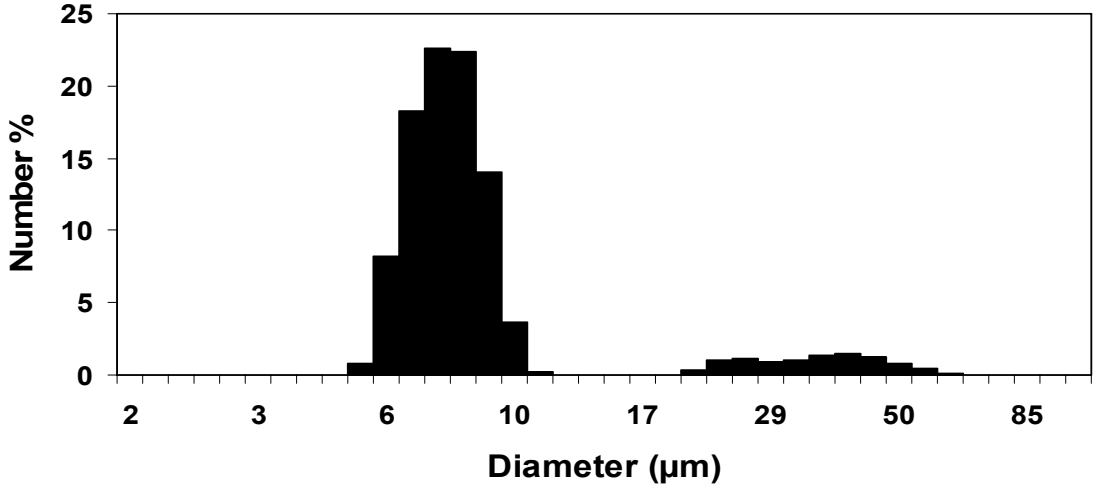

Figure 4-17 Number percent of the 38–45 µm spherical particles.

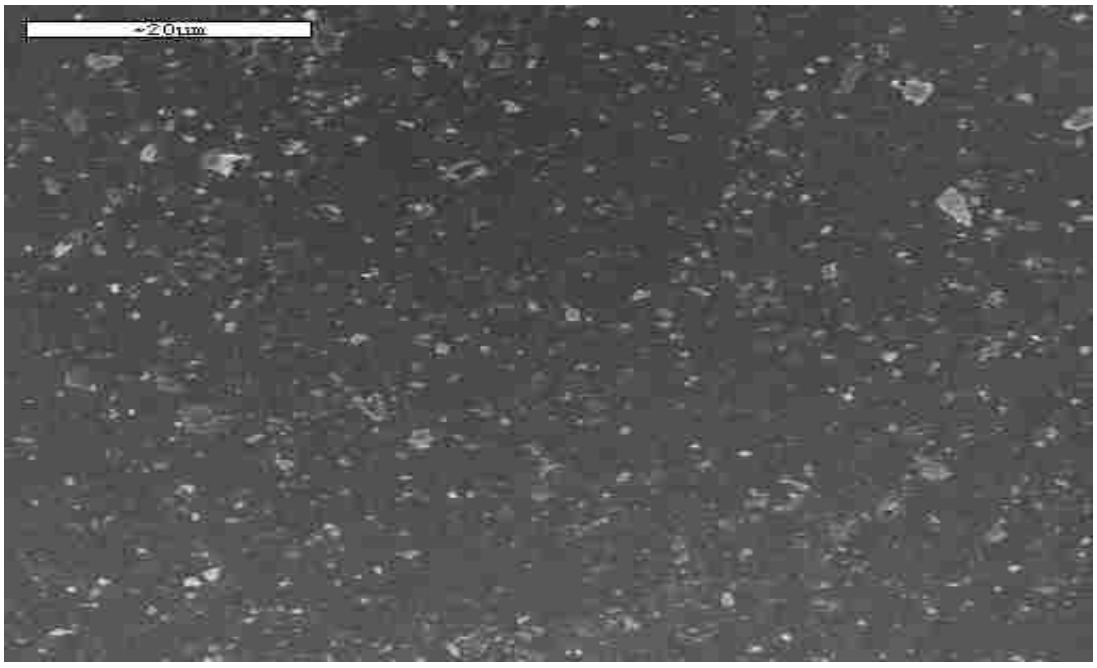

Figure 4-18 SEM image of small particles on the surface of a larger particle.

Second, even if all the smaller particles mixed in with the larger ones could be totally removed there are still small particles attached to the surfaces of the larger particles. Figure 4.18 shows a SEM image of the surface of a large 450 μm spherical particle. The image shows only a portion of the surface such that the edges of the 450 μm particle can not be seen, but very small particles in the 1μm range stuck on the surface of the particle exist in large numbers. Even after sieving the particles many times this research has shown that these much smaller particles do not become dislodged until they are entrained into the flow at which time a great amount of them come off the surface and are measured with the larger particles adding to the bimodal size distribution problem.

4.4.2 Sieving and Particle Preparation

As mentioned in the prior section, it was not possible to eliminate the bimodal size distribution characteristics of particles due to small particles either mixed in and/or attached to the larger particles. However, to provide a narrow size and shape distribution mode for the particles that were measured in this research it required thorough preparation.

Different sieving methods were used to prepare the different particles. Table 4.3 shows the number of times each of the different particles was sieved.

Table 4.3 Number of times particles were sieved.

Particle (shape/size)	Times Sieved
Seeded	
(1-10µm)	0
Spherical	
(38-45µm)	3-4
(45-51µm)	3-4
(51-63µm)	3-4
Gravel	
(38-45µm)	10-12
(45-53µm)	10-12
(53-61µm)	10-12
(75-90µm)	10-12
(90-106µm)	10-12
(106-125µm)	10-12
Cylinder	
(53-61µm)	3-4
(61-75µm)	3-4
(106-125µm)	3-4
Flakes	
(53 - 61µm)	12
(106 -125µm)	12
(180 - 212µm)	12

The sieving of all particles was accomplished with round sieve pans equipped with square mesh screen. The pans were then put into a shaker in order to shake the particles through the different mesh screens according to their size.

The spherical particles were a commercial product manufactured by Potters Industries called Spheriglass 2530 made out of soda-lime glass with a refractive index of 1.51 and a specific gravity of 2.45. They were sieved 3 to 4 times to produce a narrow distribution in the size range desired for measurement. Since the PDPA made it possible to sort the sizes of the spherical particles with their corresponding velocities, sieving these particles this many times proved to be adequate in providing enough particles in the size range needed to make good measurements.

The gravel shaped particle material used in this research was a commercial sand blasting powder made from glass and manufactured by a grinding process. Since the gravel shaped particles were irregular in shape and size they required a lot of sieving in order to obtain a reasonable distribution. Figure 4.19 shows a picture of the size and shape of the gravel particles before they were sieved. Since this is a SEM image it doesn't show these glass gravel shaped particles being transparent. The gravel shaped particles were sieved between 10-12 times at 1.5 hours for each time they were sieved. This proved to provide a reasonable distribution for this shape of particle.

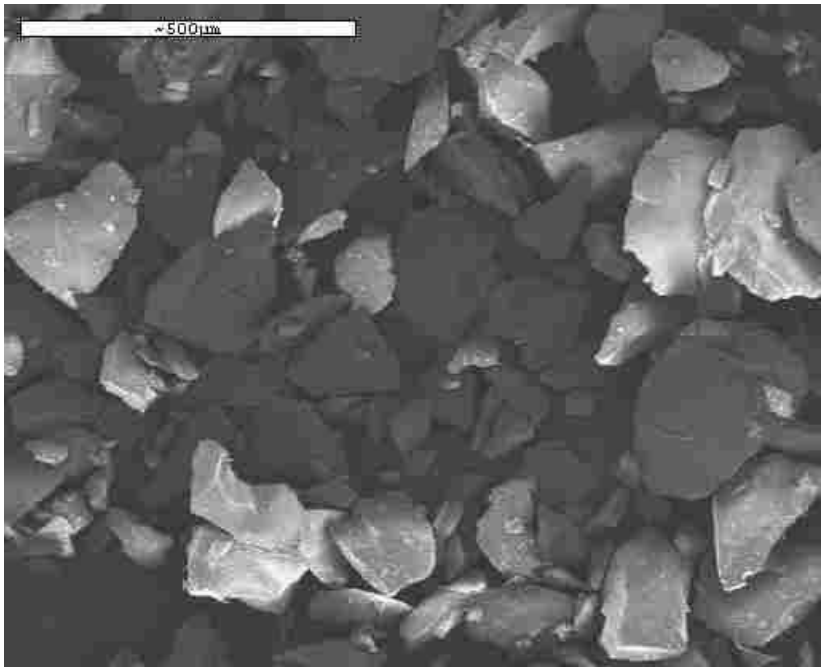

Figure 4-19 Size and shape of the gravel particles before they were sieved.

The cylindrical shaped particles used were a commercial product manufactured out of glass and used to strengthen resins for various industrial applications. The mean diameters of these particles were 16µm with lengths varying from 5 - 300µm. These cylindrical shaped particles were carefully sieved between 3 to 4 times. The reason for having to be careful in sieving this type of particle was because of the fairly large aspect ratio indicative of cylinders. Because of this large aspect ratio in contrast to the other particles this required that the cylinders be first sieved into a rough size grouping and then refined several more times into a narrower length distribution. In order to accomplish this task, only very small amounts of the particles at very short time intervals were shaken at any given time and only in a side ways direction to prevent them from sieved could be controlled. falling through the sieve lengthwise. In this manner the

length of the particles being Glass flakes with a mean thickness of 5µm used to strengthen resins in different industrial applications were used. The flakes came in many different sizes. The flakes were sieved 12 times in order to produce a narrow distribution of size and shape while removing as many as the small particles mixed in with the flakes. Like the gravel shaped particles the flakes were sieved 1.5 hours for each time the particles were sieved.

4.4.3 Particle Shapes after Sieving

During and after the sieving process the particles were examined under a microscope to check how good of a size and shape distribution they had. Figure 4.20 shows a SEM of the 38-45µm glass spherical particles.

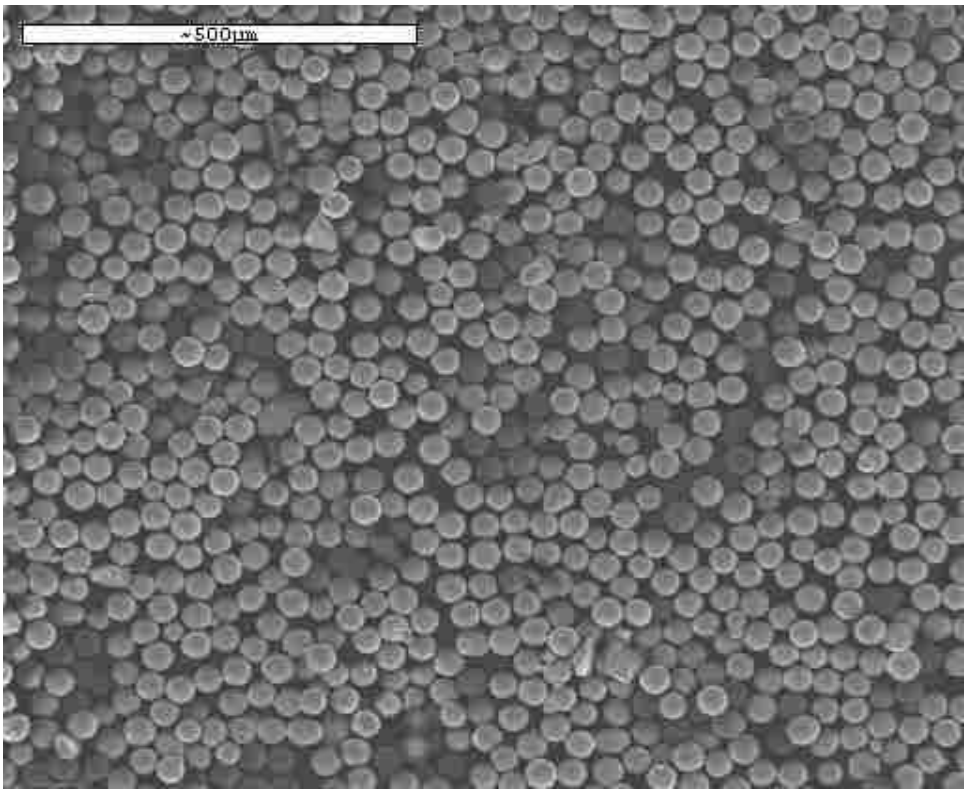

Figure 4-20 SEM of the 38-45µm glass spherical particles.

In this figure these spherical glass beads have been sieved 4 times and show that most of these particles have a fairly uniform size. Since the PDPA was used to measure these particles, this amount of sieving proved to be more than satisfactory in providing good measurements.

Figure 4.21 shows a picture of the gravel particles after they have been sieved 12 times. Since this picture was taken by a microscope instead of an SEM it shows the transparency of these glass gravel shaped particles. These gravel particles were sieved through a 53-61µm sieve size mesh and show a fairly good size distribution for having such an irregular shape to begin with.

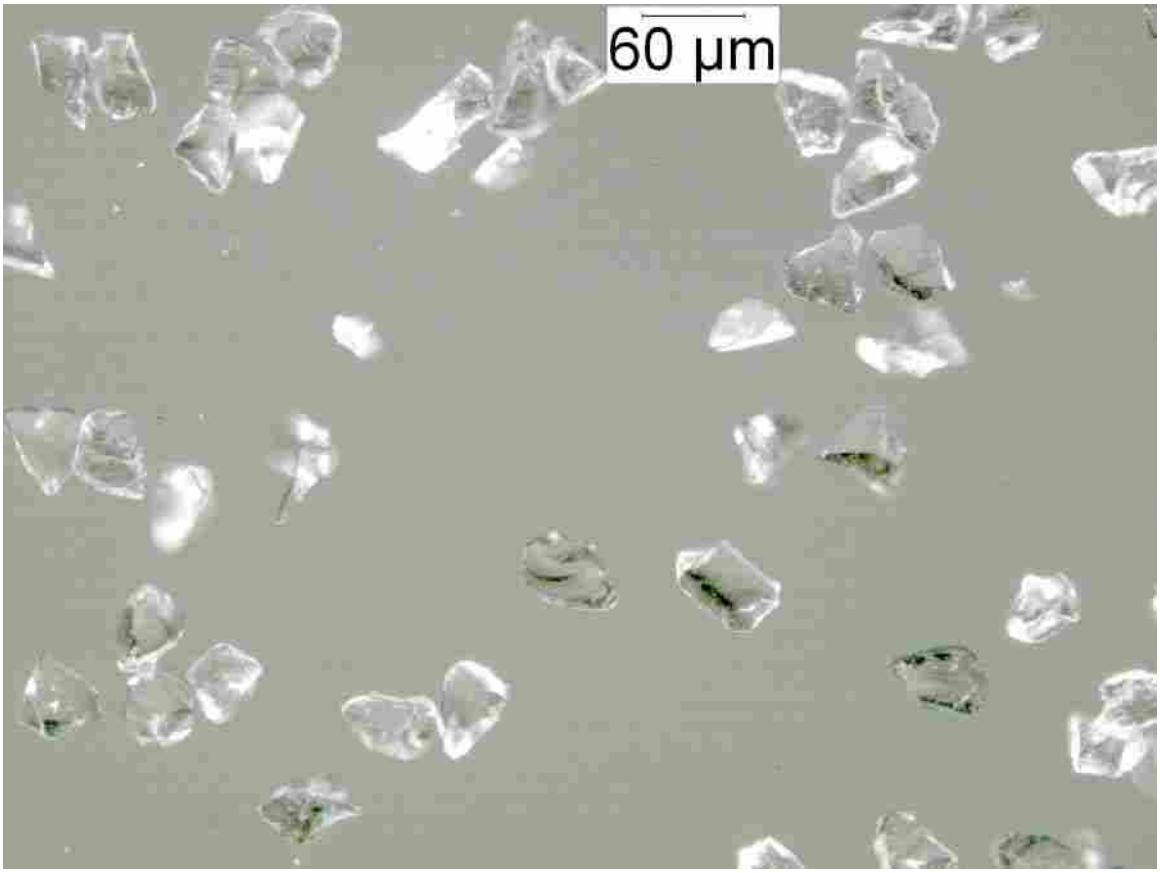

Figure 4-21 Gravel sieved 12 times through a 53-61µm sieve size mesh.

Microscope pictures of the cylindrical shaped particles and the flake particles were also taken after they had been sieved. Figures 4.22 and 4.23 show the results of the cylinders and flakes after they had been sieved.

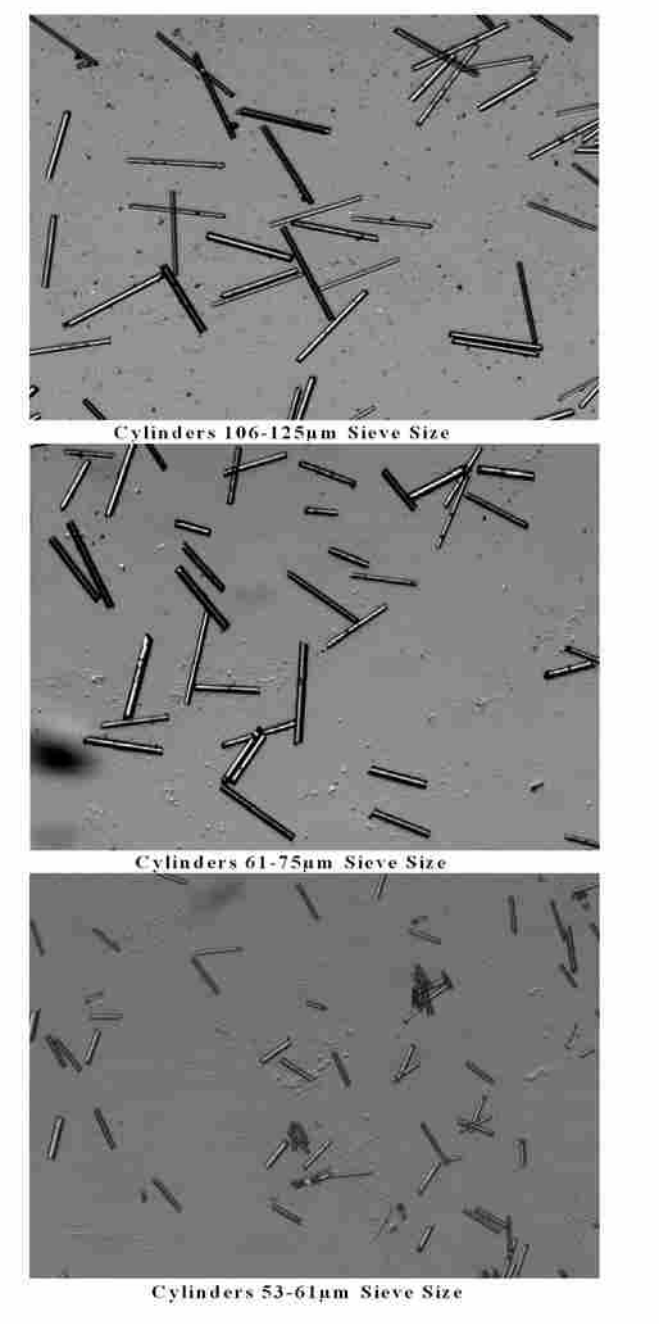

Figure 4-22 Results of cylinders after being sieved.

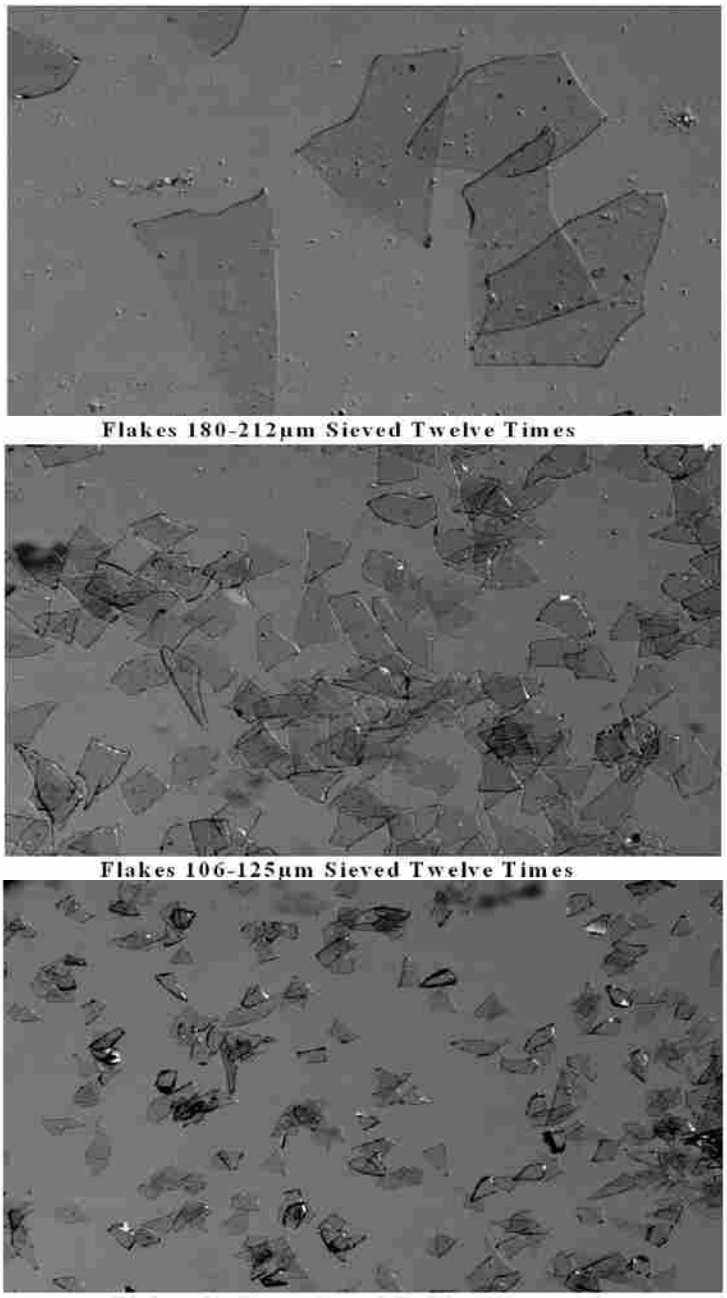

Figure 4-23 Results of flakes after being sieved.

Figure 4.24 shows an example of a size distribution of the 53-61μm sieve size flakes. The mean equivalent diameter for these flakes was approximately 96 μm. The mode of the smaller particles in this case is not shown in this diagram.

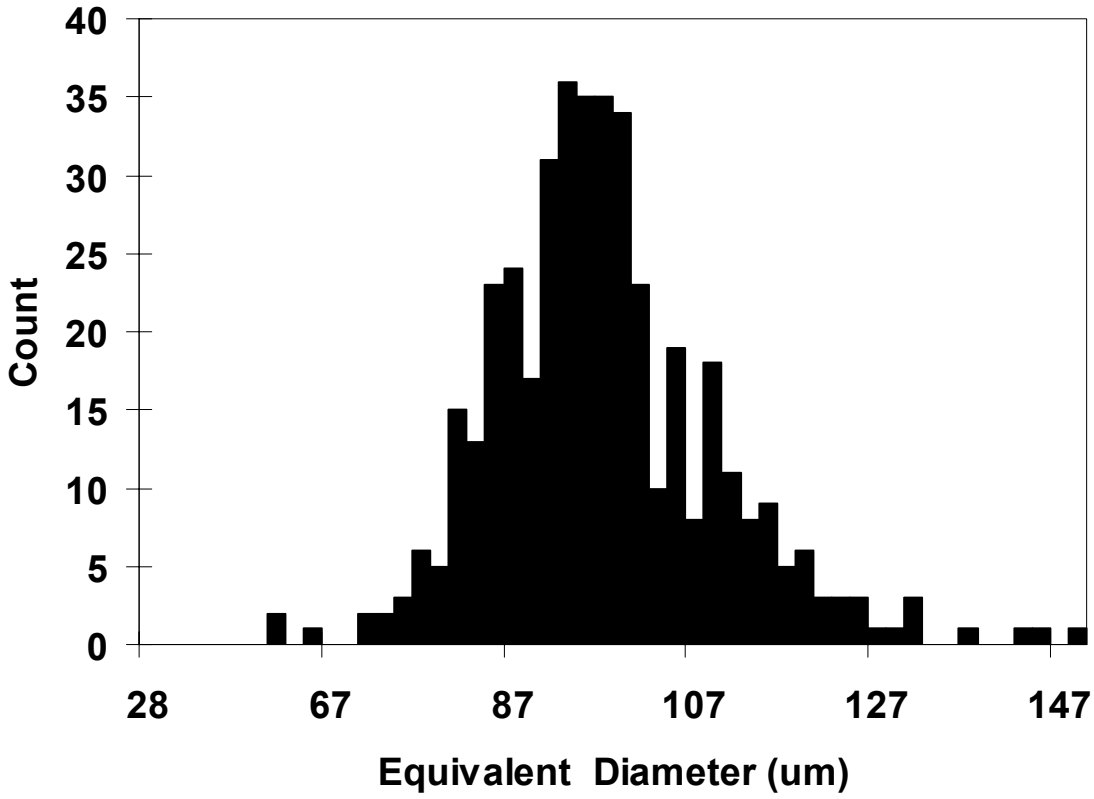

Figure 4-24 Size distribution of the 53-61μm sieve size flakes.

The results of the mean diameters and lengths of all the distributions of the particles are shown in Table 4.4. The diameter and lengths were found by using a calibrated microscope in conjunction with a computer program capable of making these measurements by tracing the particle's length and/or perimeter. From this information the average mass of each particle type was calculated by multiplying its volume by its density (2500 kg/m^3 for glass). For the case of the gravel particles it was more

complicated to calculate the mass since its thickness was difficult to measure and not well defined. However, an estimate of thickness was made from visual observations of the gravel shape under the microscope by viewing several different samples and orientations.

Table 4.4 Mean equivalent diameter for all particles after sieving.

Particle (shape/size)	Mean Equivalent Diameter (µm)	Mean Length (µm)
Seeded		
(1-10µm) Not sieved	4	
Spherical		
(38-45µm)	42	
(45-51µm)	49	
(51-63µm)	57	
Gravel		
(38-45µm sieve size)	34	
(45-53µm sieve size)	42	
(53-61µm sieve size)	49	
(75-90µm sieve size)	74	
(90-106µm sieve size)	88	
(106-125µm sieve size)	105	
Cylinder		
(53-61µm sieve size)	16	99
(61-75µm sieve size)	16	151
(106-125µm sieve size)	16	219
Flakes		
(53 - 61µm sieve size) (5µm thick)	96	
(106 -125µm sieve size)(5µm thick)	183	
(180 - 212µm sieve size)(5µm thick)	312	

4.4.4 Proper Method for Measuring Particles

As mentioned previously, it is not possible to entirely remove all the small particles from those that are to be measured. Hence there exist a bimodal size distribution one mode with very small particles and another that contains the larger particles with a significant separation between the distributions. While making measurements is not a problem with spherical particles when a PDPA laser system is used, it does present a significant problem for measuring the correct velocity for non-spherical particles.

However, this problem can be remedied by either adjusting the PMT voltage (gain) or the laser power. Since the amount of laser light scattered to the detector is proportional to the particle surface area, when either the laser power or PMT voltage are reduced enough the velocity measurements of the smaller particles can be eliminated. Consequently, reducing the laser power or PMT has the effect of filtering out the velocity measurements of the smaller particles. The main problem then is finding the correct PMT voltage that will filter out the smaller particles and measure the larger particle size distribution. The adjustment of the PMT voltage while holding the laser power constant was the method used in this research since the PMT was much easier to control.

In order to demonstrate the basic concept, data from 45-53 μm spherical particles using the PDPA were used. Since the flow is decelerating after the step, the velocity of the larger particles due to their inertia would be higher than the smaller ones whose speed is close to that of gas phase. Figure 4.25 shows two graphs aligned with each other. The top graph shows the average velocity of the all the particles sizes measured from left to right corresponding to the size distributions of the particles shown on the lower graph. In

other words, if the high PMT setting is used then the laser system measures the average velocity of the distributions of all the particles between the sizes of 1 to 60 μm. This average velocity is shown to be approximately 11.9 m/s.

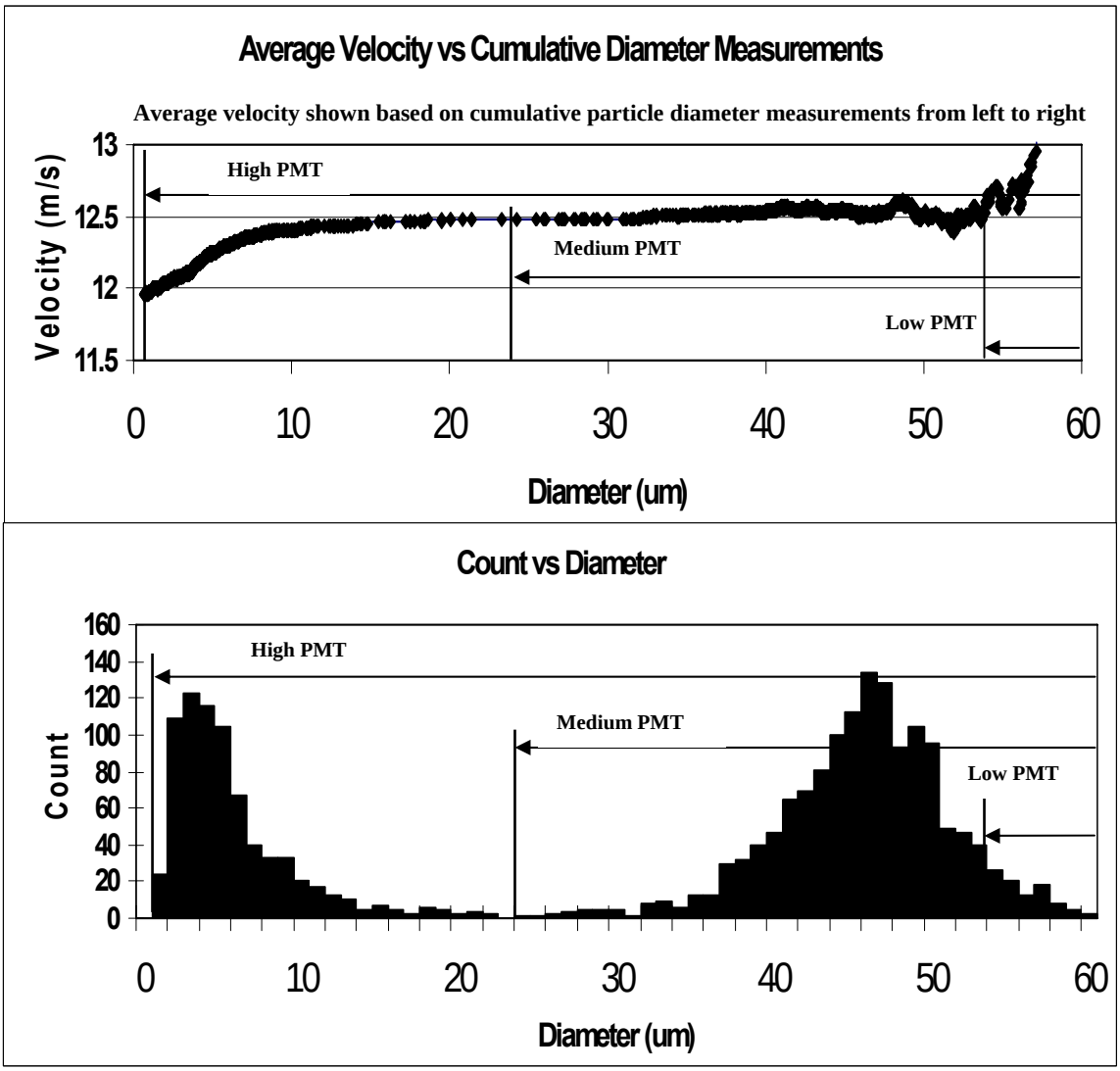

Figure 4-25 PMT versus the velocity measured for two different particle sizes.

As the PMT is further reduced somewhere between the medium and high setting Figure 4.25 shows the average velocity increases and begins to level out at 12.5m/s. The particle sizes that would be approximately measured in this situation would be between 16 and 60 μm. The average velocity has increased from 11.9 to 12.5 m/s since now very few of the velocities of smaller particles which move slower then the larger particles in a decelerating flow are calculated into this new average velocity.

If the PMT is reduced still further to the medium setting the average velocity still remains approximately 12.5 m/s and the velocities of the particle sizes being measured are between 24 and 60 μm. The velocity doesn't change significantly since there are very few particles between this region separating the small and large particle distributions.

Finally, if the PMT is further reduced to the low setting then the system only measures the much larger particles in the right tail of the large particle distribution between 54 and 60 μm. This average velocity has now increased above 12.5 m/s indicating that only these larger particles are being measured.

The correct PMT voltage for measuring the large particle distribution would then be that setting that causes the average velocity to level out. In this case it would be the medium setting. However, since there are not usually many particles in the region that separates the two distributions any PMT setting where the average velocity curve is level would provide approximately the same result.

Before using this measuring technique on non-spherical particles it was necessary to validate it effectiveness on spherical particles since these types of particles can be sized and sorted with their corresponding velocities by the PDPA. Figure 4.26 shows a

graph of the PMT voltage versus the velocity of 38-45 μm glass beads for two different situations. The measurements were made at the 7th step location and 1.4 inches in

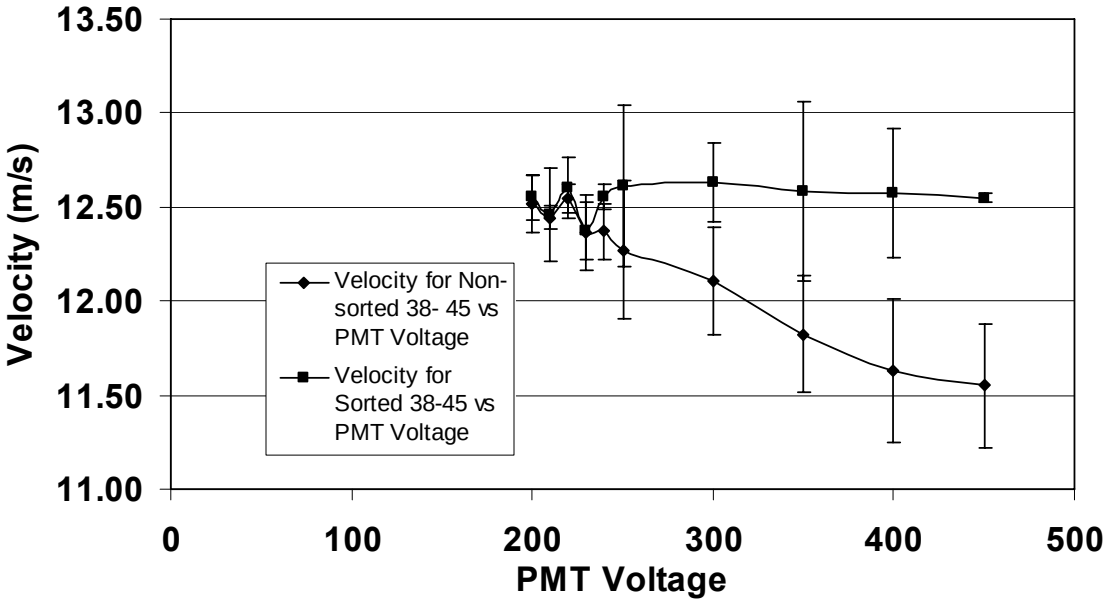

Figure 4-26 PMT versus velocity for 38-45 μm spherical particles.

from the face of the chamber in the thickness direction as shown in Figure 4-13.

The first case was for the measurements made with the PDPA where the velocities of the particles are sorted and averaged with their size between the 38-45 μm ranges. The second case was made without using the sizing capability of the PDPA and reducing the PMT in increments until the average velocity of the particles leveled out. The error bars for these measurements were based on a 95% confidence interval. The PMT setting at this condition was 200 volts the lowest setting permitted by the laser software with the laser power set at a constant 2.5 watts and the laser set up in the forward scattering direction. At these settings the two velocities are as seen in the graph approximately the same at 12.5 m/s.

This shows that by reducing the PMT at the right amount (200 PMT in this case) we can filter out the smaller particle velocities and measure only the average velocity of the larger size distribution. While the average velocity for both cases weren't exact, the method of reducing the PMT came very close to predicting the results of the PDPA. The velocity for the PMT method was 12.55 m/s while that using the PDPA was 12.52 m/s. This validation with the spherical particles shows that this method will also work with the non-spherical particles used in this research.

The method of adjusting the PMT until the average velocity leveled out was used for the gravel shape particles. Figure 4.27 shows the graph of the velocity versus the PMT used to determine the correct PMT necessary to filter out the small particles and measure only the 53-61μm sieved size gravel particles.

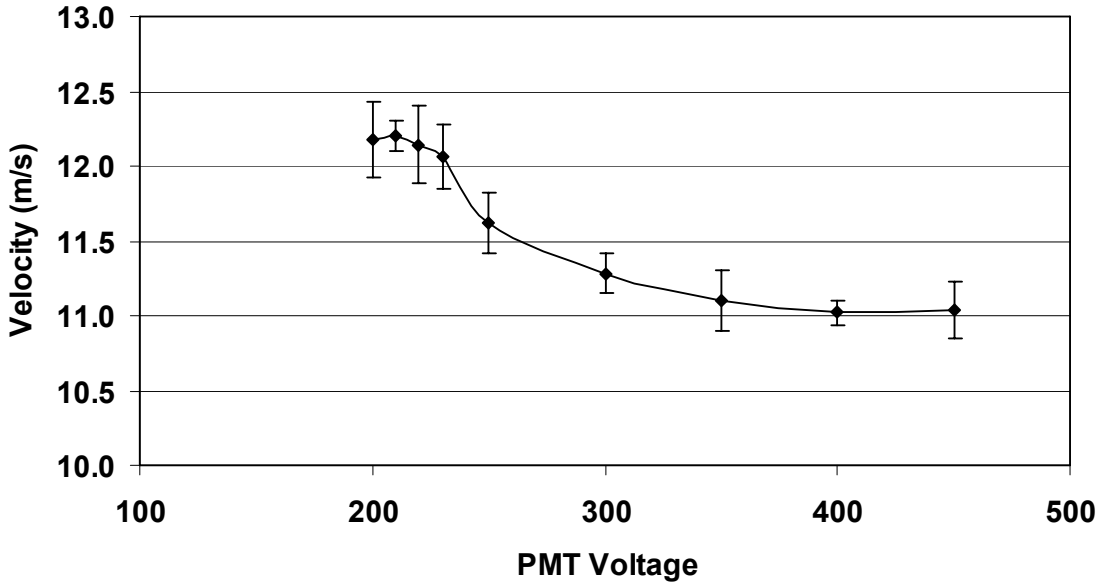

Figure 4-27 PMT versus velocity for 53-61μm sieved size gravel particles.

The laser was set up in the forward scattering direction. As is shown in this figure the average velocity of all the particles which was measured by the highest PMT of 450 volts is approximately 11.0 m/s. A confidence interval of 95 percent was used for the error bars. As the PMT was reduced more of the velocities of the smaller particle distribution were filtered out until the curve started to level out signifying that only the velocity of the larger distribution of particles 53-61μm were being measured. This occurred as shown in this graph at about a PMT setting of 200-220 volts with a corresponding velocity of approximately 12.2 m/s. Therefore, a PMT setting of approximately 210 volts was used in the subsequent velocity measurements of all the gravel sizes to obtain the correct average velocity of the gravel particles as they were measured at the various locations in the backward facing step.

This method was used for all the other non-spherical particles (cylinder and flakes) in order to find the correct PMT voltage setting necessary to measure the desired size distribution. For the cylinder and flakes the laser was set up in the backscattered direction since there were concerns that some of the particles in particular the larger flakes would block some of the laser light if in the forward scattered direction.

As an example, Figure 4.28 shows the results of this method used for the 106-125 μm sieve size cylinders (219 μm mean length). As shown in figure as the PMT voltage was reduced, more and more of the smaller particles were filtered out and the velocity begins to rise. The velocity continues to rise until all the smaller particles are filtered out. The velocity then levels out at a PMT voltage of between 340 volts and 320 volts representing the average velocity of all the cumulative velocity measurements of the

cylinder length distribution shown in figure 4.29. The average velocity of this distribution of cylinders was approximately 10.5 m/s. The velocity continues to rise after

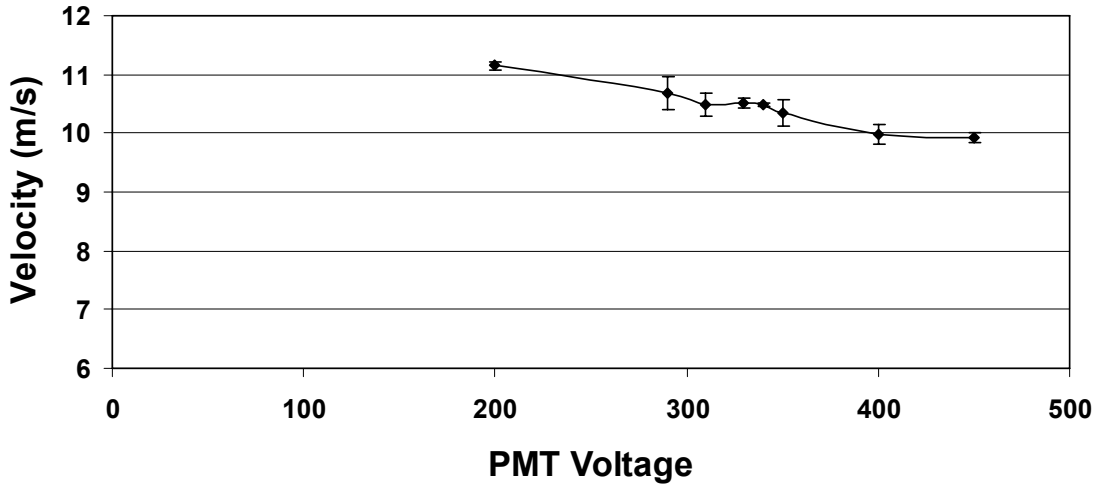

Figure 4-28 PMT versus velocity for the 106-125 µm sieve size cylinders.

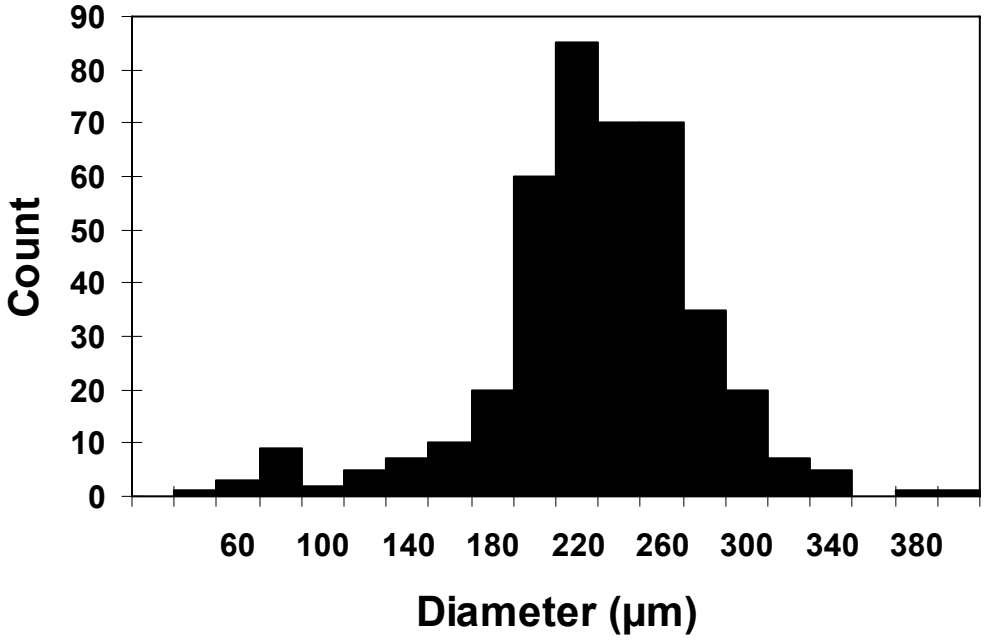

Figure 4-29 The size distribution of the 106-125 µm sieved cylinders.

leveling out as the PMT voltage is further reduced meaning that only a few of the very long cylinders mixed in with the rest of the cylinders are being measured.

As a second validation to check that the PMT voltage used to filter out the small particles was correct for the non-spherical particles, a PMT versus cutoff size method was used. This method involved examining the size distribution of the typical small particles either mixed in or stuck on the non-spherical particles. It was found that the sizes of all these small particles were within the size range of the distribution shown in Figure 4.30.

Figure 4.30 is a histogram of the distribution of the small particles mixed in or stuck on the 53-61 sieved size flakes. A microscope with a high magnification setting was used to determine the size distribution of these small particles. This figure shows the typical maximum size of these small particles to have an equivalent diameter of approximately 12 μm.

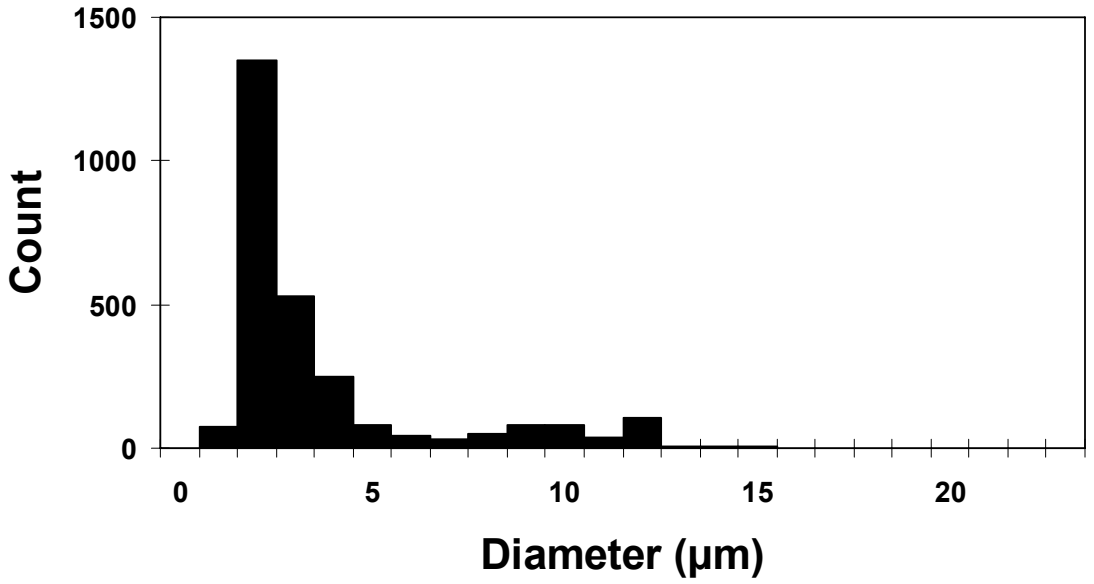

Figure 4-30 Size distribution of small particles on non-spherical particles.

Since the seeded particles had a similar size range to that of the little particles mixed in or stuck on the flakes a method was devised to determine a PMT cutoff for the seeded particle per their given size and use this for the small particles associated with the flakes and cylinders. Using this information to determine a cutoff PMT for the small particles many samples of seeded particles with a mass of 0.2 grams were prepared and entrained in the flow at a nearly constant rate at varying PMT settings from a high of 450 to a low of 200. Four different sets of measurements were made between these two settings. At these various PMT settings the number count of the seeded particles being measured was recorded and related to the corresponding fraction of the frequency size distribution of the seeded particles. By comparing the number of seeded particles counted by the laser at the varying PMT against that of the seeded frequency size distribution a correlation was made relating size of the particles being filtered out to a PMT. Figure 4.31 shows the relationship of the size of the seeded particles to that of its corresponding PMT setting necessary to cutoff that size from being measured.

From Figure 4.31, the cutoff for seeded particles with a diameter of 12 μm or less was a PMT of approximately 330. Consequently, a PMT of this same amount should also filter out the small particles with an equivalent diameter of 12 μm or less that are stuck on and/or mixed in with the flakes. This PMT setting checked out to be approximately the same as that obtained by the PMT versus velocity method where the correct setting is determined by where the velocity levels out. Table 4.5 shows the correct PMT voltages for the different size and shape particles. In addition, this table shows the orientation in which the laser was setup when taking the measurements for the different particles.

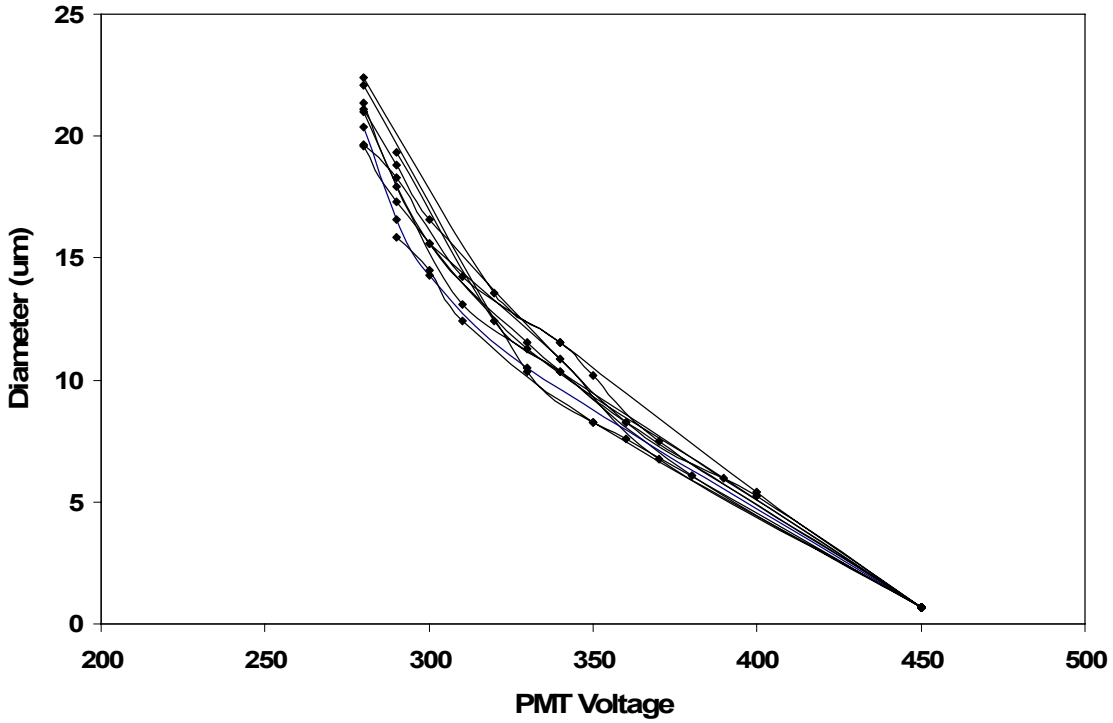

Figure 4-31 PMT cutoff voltage versus the size of the particle.

The method of adjusting the PMT until the velocity leveled out was used for all the non-spherical particles to make the velocity measurements. As was mentioned this method was also validated using the cutoff voltage correlation for the small seeded particles which are similar in size to those small particles associated with the non-spherical particles. The method used in this research to measure the velocity of the non-spherical particles provided the necessary information to estimate the drag coefficients of these particles.

Table 4.5 PMT voltage and laser direction used to measure the velocity of the given particles.

Particle (shape/size)	PMT(Voltage)	Laser Direction
Seeded		
(1-10µm dia.)	450 (PDPA Sizing Used)	Forward Scattering
Spherical		
(38-45µm dia.)	450 (PDPA Sizing Used)	Forward Scattering
(45-51µm dia.)	450 (PDPA Sizing Used)	Forward Scattering
(51-63µm dia.)	450 (PDPA Sizing Used)	Forward Scattering
Gravel		
(38-45µm sieve size)	210	Forward Scattering
(45-53µm sieve size)	210	Forward Scattering
(53-61µm sieve size)	210	Forward Scattering
(75-90µm sieve size)	210	Forward Scattering
(90-106µm sieve size)	210	Forward Scattering
(106-125µm sieve size)	210	Forward Scattering
Cylinder		
(53-61µm long) (16µm dia.)	330	Back Scattering
(61-75µm long) (16µm dia.)	330	Back Scattering
(106-125µm long) (16µm dia.)	330	Back Scattering
Flakes		
(53 - 61µm sieve size) (5µm thick)	330	Back Scattering
(106 -125µm sieve size)(5µm thick)	330	Back Scattering
(180 - 212µm sieve size)(5µm thick)	330	Back Scattering

5 Results

Experimental results of velocity, velocity slip, and drag coefficient as a function of position, size, and shape of the particles are presented in this chapter. The first two sections will provide the results of the gas phase and spherical particles. The next sections show the results for the three non-spherical particles: gravel, flakes, and cylinders.

5.1 Gas Phase Results

The velocity profile above the step was checked. These gas phase velocity measurements were made at both the thickness and side centerlines. Figure 5.1 shows a graph of the velocities along the thickness centerline and Figure 5.2 shows

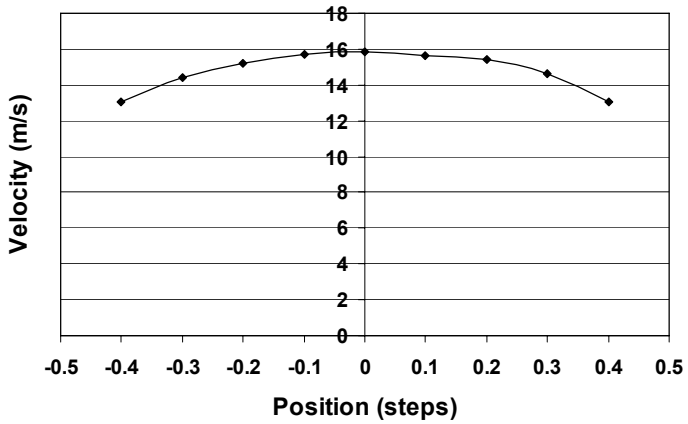

Figure 5-1 Thickness centerline velocity profile above the step.

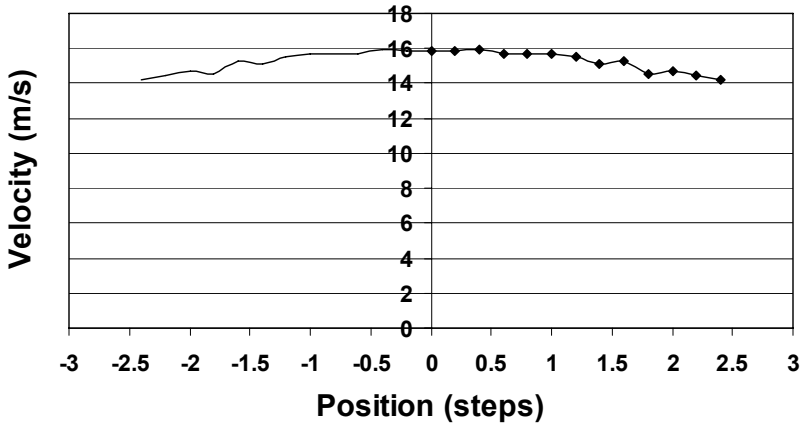

Figure 5-2 Side centerline velocity profile above the step.

the velocities along the side centerline. For the velocities shown in figure 5-2, it was difficult to get the laser to measure the left haft of the centerline due to the laser's receiver having to be offset on that side. Therefore, to show the overall flow profile from this vantage point the line containing the measurements on the right side was superimposed on the left. Also, the velocity measurements could not be made past 2.4 steps from the centerline since this was where the windows ended. From these measurements it indicates the flat velocity profile typical of a fully developed turbulent flow.

Figure 5.3 shows the seeded particle or "gas velocity" profiles across the thickness of the chamber at 10 axial positions below the step. These data characterize the flow field for this particular backward facing step.

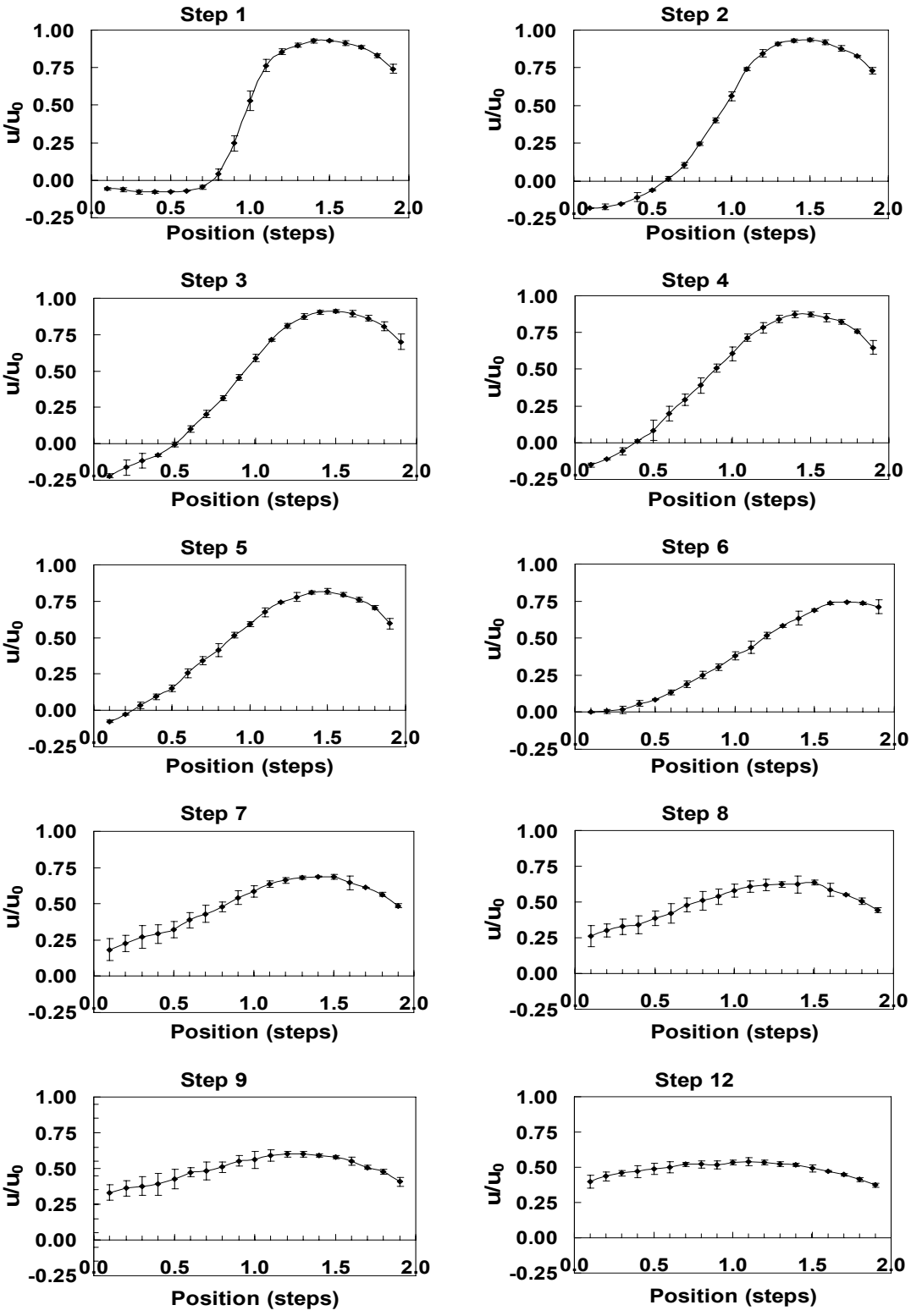

Figure 5-3 Gas phase velocities in backward facing step.

The data are useful for three purposes: 1. a characterization of the flow for comparison with existing data in the literature, 2. validation of the accuracy of CFD calculations used to characterize the flow more completely and 3. to establish a baseline to identify day-to-day experimental variations or experimental errors. The difference between gas and particle phase velocity used in the drag coefficient measurements was typically obtained by re-measuring the seeded flow data on the same day particle velocity was measured due to the potential for minor day-to-day differences in the flow field. As was mentioned in Chapter 4, the "gas phase" measurements were taken at ten different vertical distances below the step starting at 25.4 mm (1 inch, 1 step height) and extending to 228.6 mm (9 inches, 9 step heights) at 25.4 mm increments and then skipping to 304.8 mm (12 inches or 12 step heights). At each of these vertical distances from the step, 19 measurements at an equal spacing of 2.54 mm (0.10 inches, 0.10 step) were made at the centerline across the 50.8 mm thickness of the chamber. The uncertainty denoted by the error bars on the figure are based on a ninety percent confidence interval calculated from three sets of different measurements each taken on a different day. The velocity was non-dimensionalized by dividing each velocity u by u_o, the maximum upstream velocity of 16 m/s.

At the first step height the velocity profile has the expected fully developed profile from 25.4 to 50.8 mm which is the region directly below the upper channel. A negative velocity is seen over most of the 0 to 25.4 mm region directly below the step. This negative velocity region identifies the recirculation zone which extend from the step to approximately 152.4 mm or six step heights where the flow begins to reattach. Reattachment for a backward facing step is expected to be between 6 and 8 step heights

below the step (Kim 1980). Reattachment occurring at the lower end of typical values may be a result of downstream boundary conditions where the flow slows in a large plenum rather than continuing in a loop as is often the case.

Beyond the sixth step height, the flow is positive across the thickness of the chamber and rapidly moves toward a new fully developed profile. At 12 steps heights the flow is almost fully developed. The largest negative velocity occurs at 3 step heights. From this point on, momentum is transferred from the higher velocity flow to the right to the lower velocity flow on the left. The region of highest acceleration (or deceleration) occurs where the velocity profile has the steepest slope. This moves from the center of the chamber toward the right side as the flow proceeds in the axial direction. The locations of highest deceleration where the flow is also primarily in the axial direction was selected for the drag coefficient measurements. This occurs between 7 and 9 step heights.

In addition to these measurements, CFD modeling was completed using Fluent to predict the gas phase velocities. A three dimensional mesh with approximately 200,000 nodes was used in the calculation with the two equation K-epsilon turbulence model. The average velocity of the flow up-stream of the step (15 m/s) was used as an inlet boundary condition. An outflow boundary condition was used at the exit of the chamber. A number of different meshes and configurations were used to obtain the results. Figure 5.4 shows a comparison of the results of Fluent versus that of the measurements.

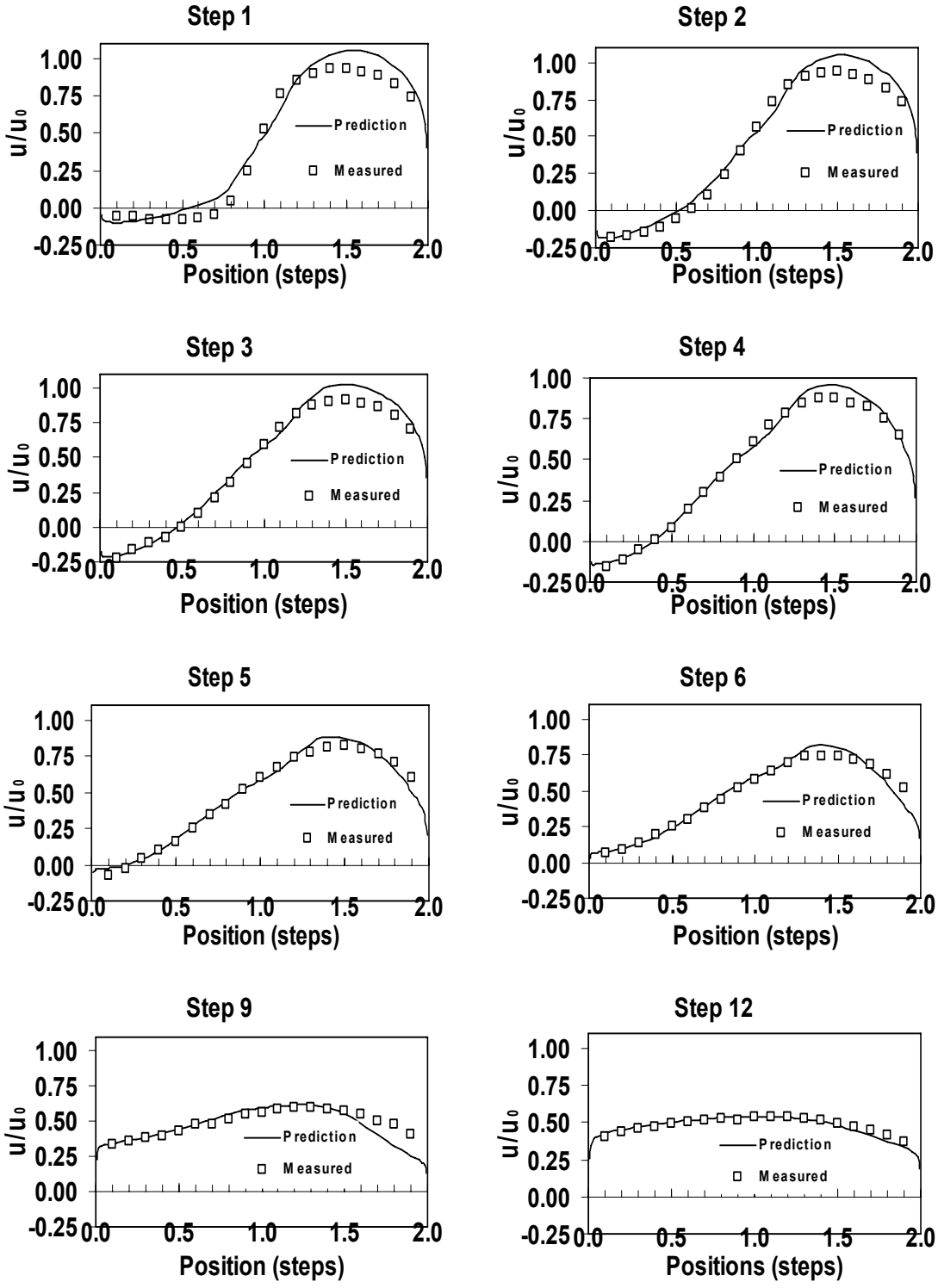

Figure 5-4 Fluent versus measured velocity for gas phase.

During the first three step heights, the measurements and predictions show remarkably good agreement in the re-circulating region, but the measured data show the flow to be decelerating more rapidly than the predictions for the flow downstream of the duct. This may be caused by the inability of the model to capture the turbulent transport of momentum correctly which is a know weakness of simple RANS turbulence modeling. The generally good agreement between model and measured data suggest the component of mean velocity which could not be measured by experiment can be obtained from the CFD results and used to check for flow continuity.

Turbulence intensity in the axial direction is shown in Figure 5.5. The turbulence intensity used in this graph is defined as u'/u_0 where u' is the root mean squared (rms) velocity and u_0 is the maximum upstream velocity. The turbulence intensity varied from a low of 7.7% to a high of about 23.7%. As can be seen from the graphs, the turbulence intensity at the beginning had a narrow spike at a distance of about one step height in from the face of the chamber and begins to spread towards the side (left) the further the flow travels downward. This continued until about the 6^{th} step (the reattachment length) where the turbulence intensity began to quickly level off until at the twelfth step the intensity was nearly completely constant across the entire centerline. The peaks in the turbulence intensity are consistent with the formation of turbulence in the shear layer or regions of high velocity gradient. As the velocity gradient moves toward the step side (left) of the chamber the peak in turbulence intensity follows. The turbulence intensity reduces as the velocity gradient diminishes in the downstream direction.

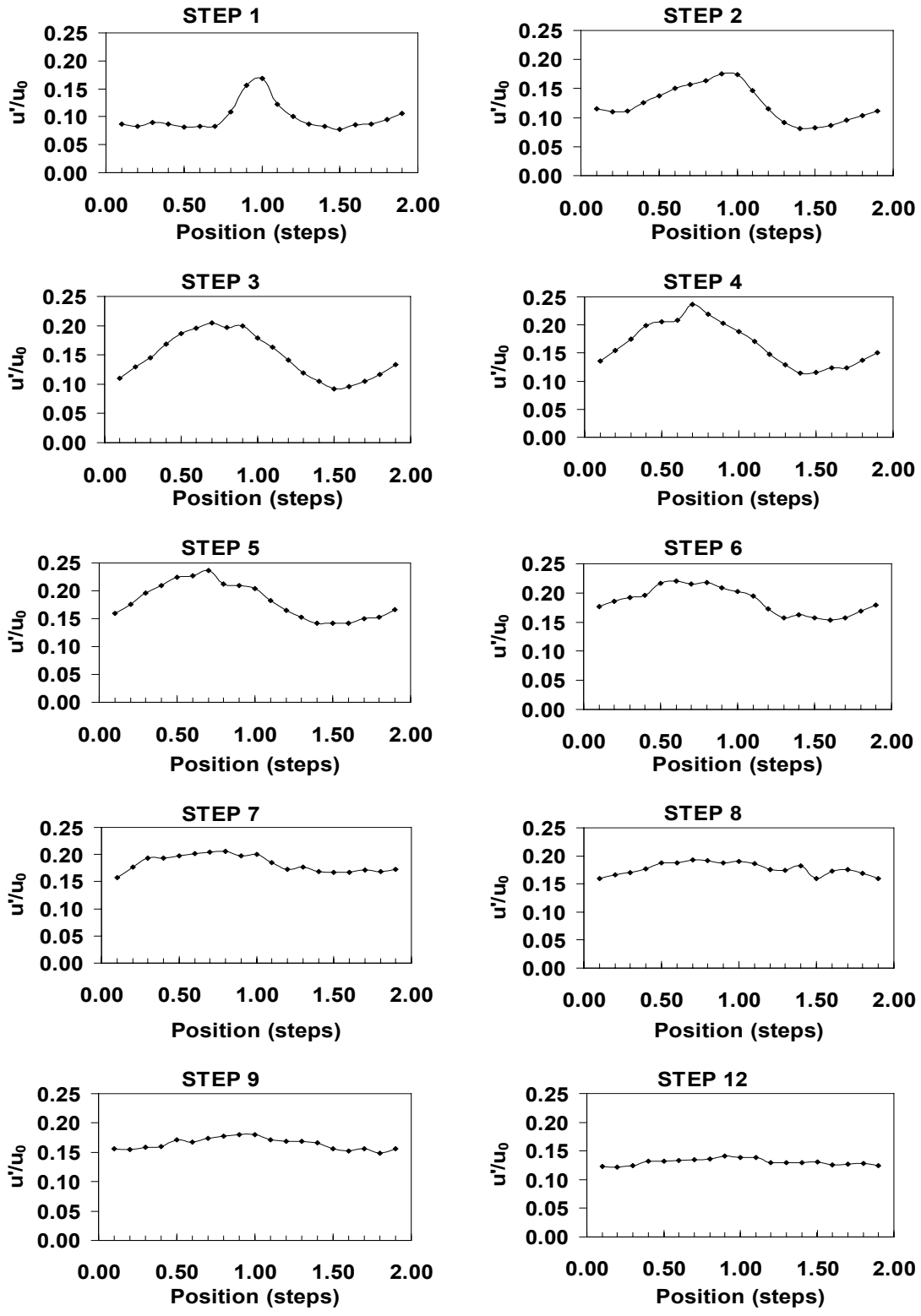

Figure 5-5 The turbulence intensity of the gas phase.

5.2 Particle and Gas Phase Velocity Comparison

5.2.1 Spherical Particles

The velocity measurements of three different size distributions of spherical glass particles were made at various locations after the step with the PDPA. The three diameter size distributions of spherical particles were those captured between sieve sizes of 38-45, 45-53 and 53-61 μm. Figure 5.6, shows the velocity measurements at the different steps for the three different size distributions in comparison to the "gas phase" velocity. Once again the velocity measurements have been normalized by the maximum upstream velocity of 16 m/s. As can be seen from this figure, as the flow progresses past the step the gas slows more rapidly than the particles and the particles do not reverse flow as readily in the recirculation zone. Although differences between particle sizes are less pronounced than the difference between the "gas" and particle phases, the larger particles consistently retain a higher velocity than the smaller particles. As expected, the larger particles have a larger velocity slip.

Table 5.1 shows the average slip of the three different size distributions of spherical particles based on the average difference between the gas and particle velocities between 25.4 and 50.8 mm at each axial position. The reason that only these velocities were used in calculating the average slip shown in Table 5.1 was because there was a much higher concentration and data rate producing a better average in this region. The average slip values shown in this table vary from near zero at step 1 to a maximum of 25% at step 9. This table also shows that when averaged, the slip is more clearly seen to increase with increasing particle size as expected.

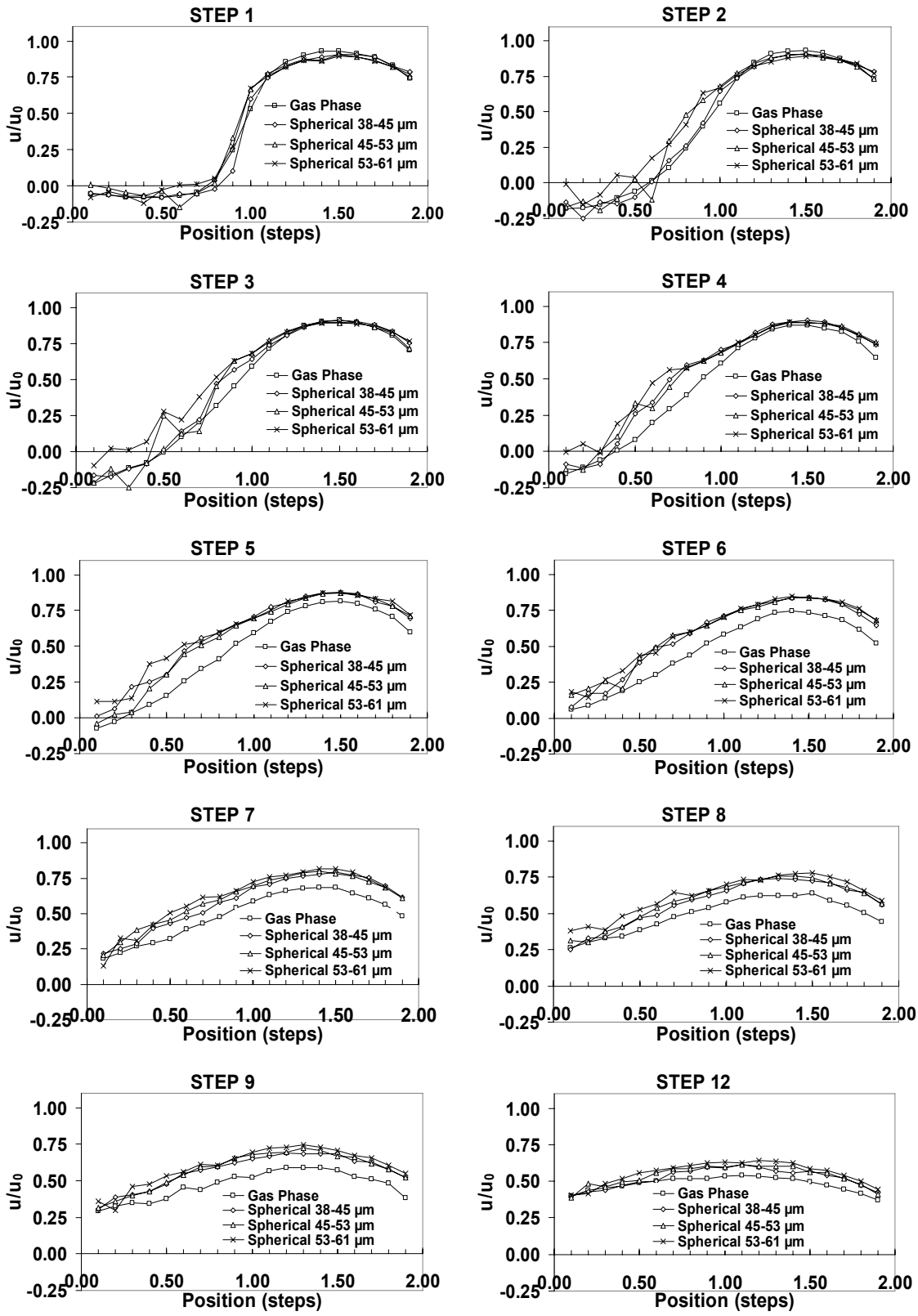

Figure 5-6 Spherical particles versus gas phase.

Table 5-1 Average slip (in percent) for spherical particles.

	Average Slip		
Step	38-45μm	45-53μm	53-61μm
1	0.44	3.54	0.76
2	0.05	0.10	0.20
3	2.05	2.11	2.62
4	5.89	5.11	5.19
5	10.51	9.91	10.91
6	16.18	16.88	17.79
7	17.15	17.51	20.85
8	18.84	20.74	24.69
9	17.60	20.04	25.00
12	12.65	14.51	19.95

One method for predicting the slip of spherical particles due to either a decelerating or accelerating flow is given by Equation 5.1 (Albrecht 1986). This equation is derived from the particle momentum equation assuming the maximum slip is located where the rate of change in slip is equal to zero. The actual slip of a particle can be expected to differ from that predicted by the equation because the derivation of the equation assumes that the gas velocity undergoes a constant deceleration that produces a force on the particle. In the actual flow, the deceleration is not constant and must be approximated using two measured velocities a finite distance apart. The equation should

nevertheless be useful in determining the order of magnitude expected for the velocity slip.

$$S_{\max} = \frac{m_p \frac{du_f}{dx}}{\frac{du_f}{dx}(m_p) + 3\mu\pi d_p} \qquad \textbf{(5.1)}$$

Where:

S_{max} = maximum slip

m_p = mass of the particle

du_f/dx = the spatial gradient of velocity

μ = viscosity of air

d_p = the diameter of the particle

Using the average gas phase measurements over the range from 25.4 to 50.8 mm, to supply the velocity gradients for Equation 5.1, S_{max} was calculated for each particle size assuming the average diameter as representative of the distribution. Figure 5.7 shows a comparison for the three sizes of spherical particles at each step height location. As can be seen in the figure, the agreement between the measured and the predicted slip improves with increasing distance from the step. This is because the points used to measure the velocity slip are assumed to be along streamlines but in reality this assumption is very poor near the step and becomes increasingly better downstream from

the step. The improved agreement of the measured and predicted slip at larger distances suggests this is a better location from which particle drag estimates can be made from successive points in the axial direction. Using the Fluent simulation it was determined a streamline passing through a point at 7 step heights and 38.1 mm from the left wall would pass approximately 0.254 mm to the left of the point directly below it at 8 step heights. This meant that the two measured velocities at eighth and ninth step heights, 38.1 mm from the left wall would provide a good approximation of two velocities along a streamline 25.4 mm apart.

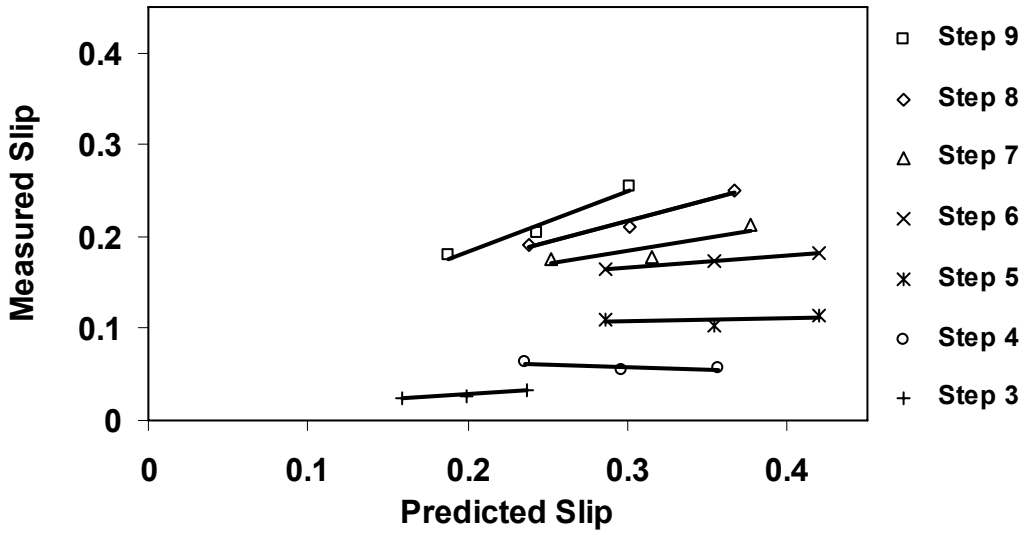

Figure 5-7 Measured versus predicted slip for spherical particles.

Using these two data points, the measured and predicted velocity slips could be compared more accurately. The result was a lower velocity slip in the measured data than was predicted by Equation 5.1. This result was consistent for any set of points that were selected for comparison at any of the spherical particle sizes.

5.2.2 Gravel Shaped Particles

The velocities of six different sieved sizes of gravel shaped particles were measured in the backward facing step. The six different sizes were 38-45, 45-53, 53-61, 75-90, 90-106, and 106-125 μm. Figure 5.8 shows the velocities of three sizes of the gravel shaped particles, 38-45, 45-53 and 53-61μm versus the gas phase velocity. While Figure 5.9 shows the velocities of the larger sizes of these particles, 75-90, 90-106, and 106-125 μm. At the first step, the gas phase velocity is higher than the particle phase which is inconsistent with the physical process occurring but indicative of the uncertainly of the measurements. At later axial positions, the gravel is seen to slip and maintain a higher velocity than the gas phase with the expected trend that the larger particles slip more than the smaller particles.

This trend is opposite to the results of Black (1997), who used essentially an accelerating flow in which no difference was found in the velocity between the same gravel shaped (ground glass) particles and the gas phase. The reason for there being no difference in velocity between the gas phase and the ground glass in the research of Black (1997) may likely be due to a small particle bias as was seen in these experiments prior to reducing the PMT voltage to eliminate the small particles.

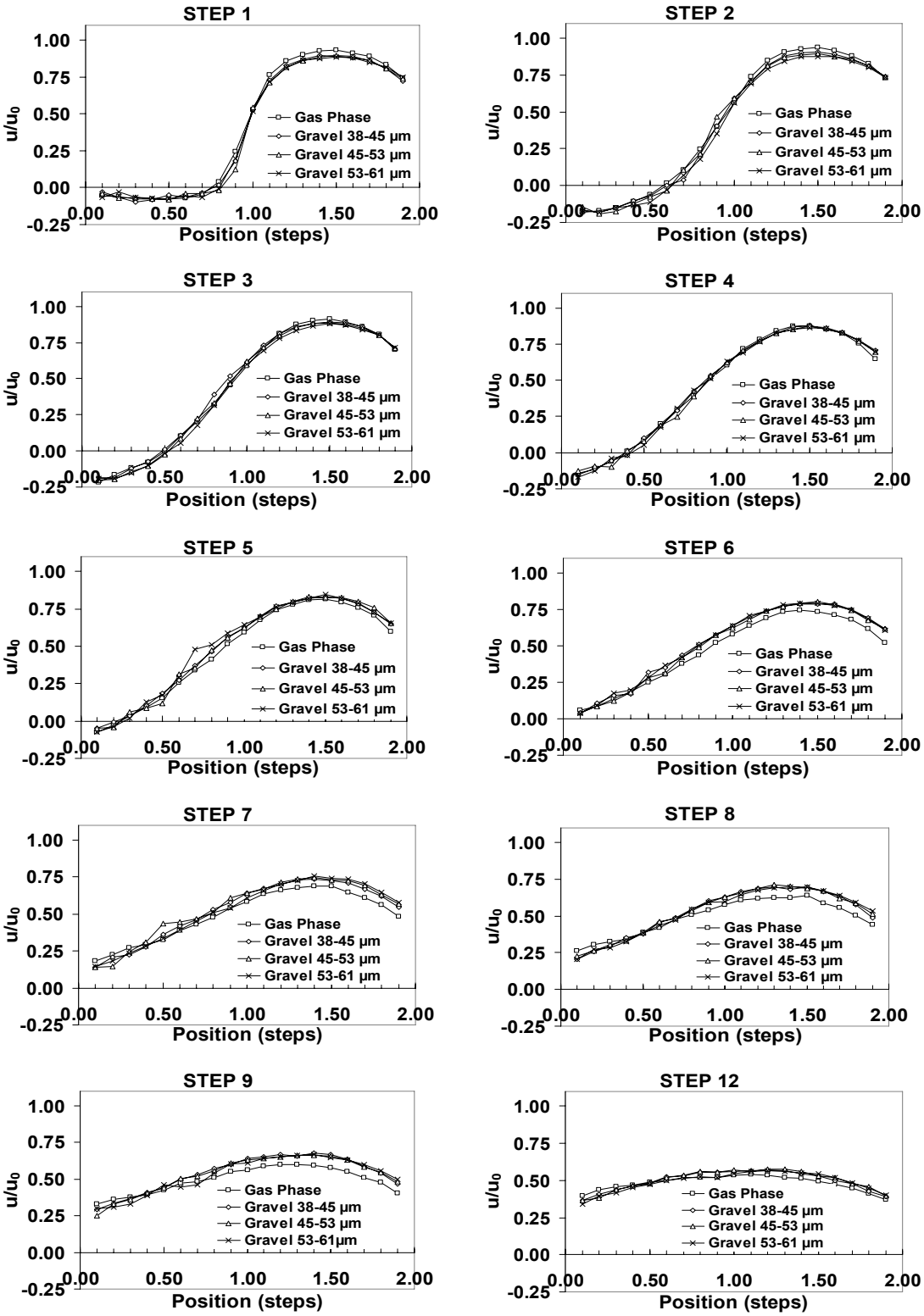

Figure 5-8 Normalized velocities for three gravel shaped particle sizes as a function of axial and horizontal location.

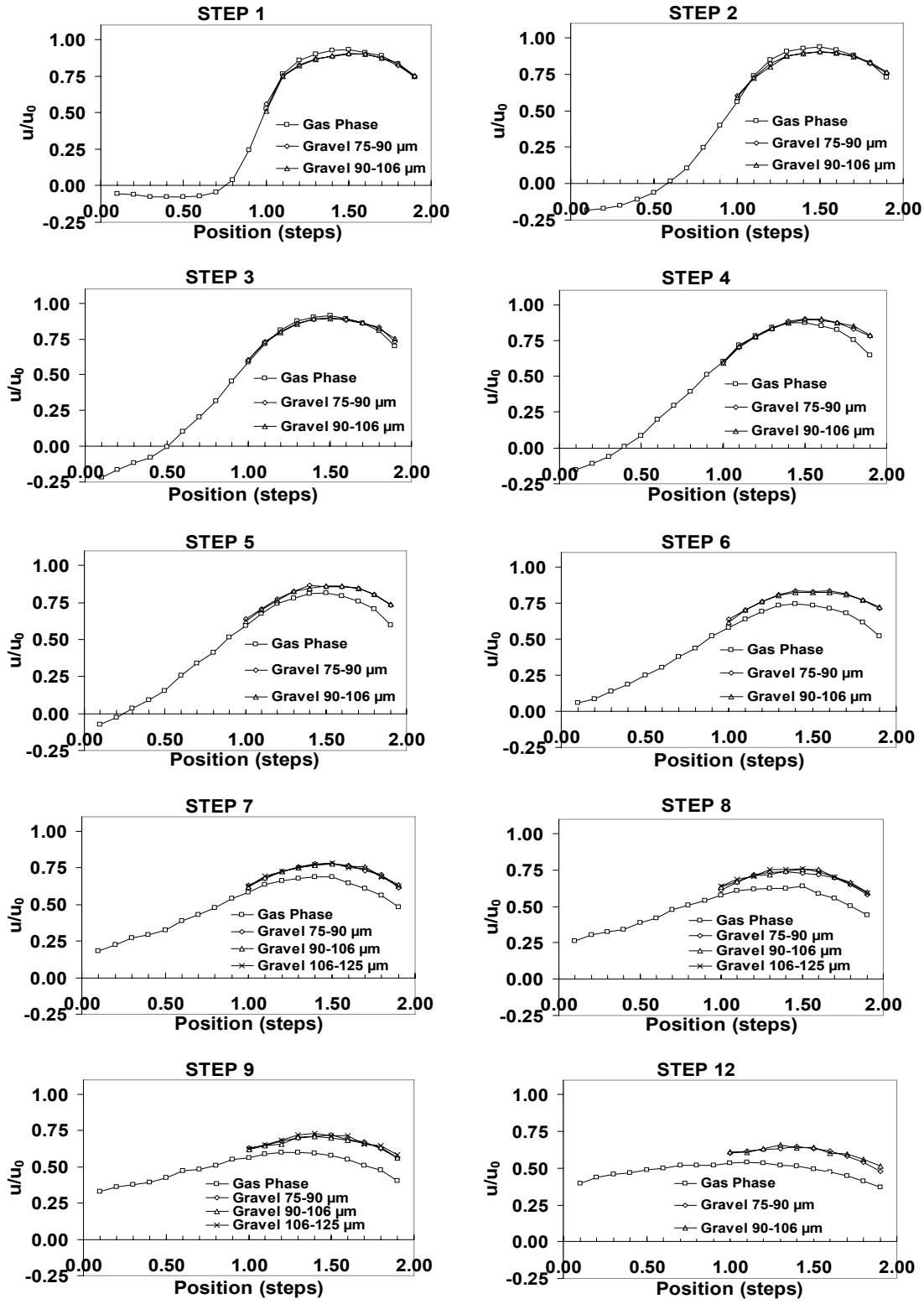

Figure 5-9 Normalized velocities for three other gravel shaped particle sizes as a function of axial and horizontal location.

Table 5.2 shows the slip results of the gravel shaped particles used in the backward facing step. As can be seen from this table, the range of the slip varied from about a -4.5 to thirty five percent. Once again the average slip was calculated at each step by using the velocities from a distance of 25.4mm from the left face of the chamber.

Table 5-2 Average slip (in percent) of gravel shaped particles.

	Average Slip					
Step	38-45μm	45-53μm	53-61μm	75-90μm	90-106μm	106-125μm
1	-3.09	-3.14	-3.72	-1.27	-1.92	
2	-1.77	-2.56	-4.46	-0.72	-1.01	
3	0.16	-0.60	-2.05	0.51	0.63	
4	1.01	0.74	0.38	3.98	4.49	
5	3.68	4.10	4.11	9.06	8.63	
6	9.52	8.83	9.41	16.30	15.51	
7	8.34	10.04	10.14	15.27	15.55	15.23
8	10.35	15.85	20.23	31.52	35.18	33.63
9	13.60	12.80	13.05	22.23	21.46	24.01
12	6.01	7.90	7.30	23.86	25.90	

5.2.3 Cylinder Particles

Because of the difficulty in obtaining sieved particles of the correct size, the cylinder shaped particles were measured at only four locations below the backward facing step. Each of these two pairs of velocity measurements was used in the particle momentum equation to calculate the drag coefficient at two locations for these particles. These measurements were made at the 7.5^{th} and 8^{th} steps, 43.2 mm from the left wall and at the 9^{th} and 9.5^{th} steps, 35.6 mm from the left wall. The results of the average velocity of the cylinders and seeded gas phase are shown in Table 5.3. The results showed the

velocity of all three different sizes of cylinders to be approximately the same in spite of their significantly different masses and lengths. This was significantly different than expected as the larger particles with more momentum were expected to slip more than the smaller particles.

Table 5-3 Velocities of the cylinders versus gas phase.

Particle (shape and size)	Velocity (m/s) at Axial Locations			
	Step 7.5	**Step 8.0**	**Step 9.0**	**Step 9.5**
Cylinders				
53-61µm	10.80	9.76	10.36	9.76
61-75µm	10.91	9.78	10.50	9.76
106-125µm	11.00	9.83	10.39	9.76
Seeded				
1-10µm	9.76	8.80	9.52	9.01

5.2.4 Flake Particles

Velocities for flake shaped particles were taken at the same four measurement locations as the cylinders. Results of particle and "gas phase" velocity are given in Table 5.4 As with the cylindrical particles there is no significant influence of size on velocity slip. These data suggest there is some physical phenomena working on the particles that is not well described by the velocity slip calculations. As a result, a more rigorous description of the force on the particles was sought by determining the drag coefficient based on the particle momentum equation for each of the particle shapes and sizes.

Table 5-4 Velocities of the flakes versus gas phase.

Particle (shape and size)	Velocity (m/s) at Axial Locations			
	Step 7.5	**Step 8.0**	**Step 9.0**	**Step 9.5**
Flakes				
53-61µm	10.84	9.81	10.43	9.86
106-125µm	10.90	9.79	10.41	9.86
180-212µm	10.78	9.82	10.46	9.86
Seeded				
1-10µm	9.76	8.80	9.52	9.01

5.3 Drag Coefficient

The particle momentum equation was introduced in Chapter 3 where all of the forces acting on a particle were described. The largest force on particles below the step is expected to result from drag resulting from the differences in the particle and gas phase velocity. The resulting equation, repeated from Chapter 3 is shown again as Equation 5.1. This equation can be rearranged to determine C_D from the velocity gas a particle velocities at two points along a streamline as shown in Equation 5.2. The errors in the measurements using this equation for the proceeding graphs were estimated based on a confidence interval of between eighty and ninety percent.

$$m\frac{du_p}{dt} = \frac{1}{2}\rho(u_p - u_g)^2 c_D A \qquad \textbf{(5.2)}$$

$$C_D = \frac{2m\dfrac{du_p}{dt}}{\rho(u_p - u_g)^2 A} = \frac{2m\dfrac{u_{P,2} - u_{P,1}}{(y_2 - y_1)/u_p}}{\rho(u_p - u_g)^2 A} \qquad \textbf{(5.3)}$$

A measurement of the drag coefficient, C_D, between the two measured points was obtained for the flow conditions for each of the spherical particle sizes. Data from Ruck and Makiola (1988) were also used to calculate the drag coefficients which are at higher Reynolds numbers. These data, C_D versus Reynolds number are plotted in Figure 5.10 where they are compared with theoretical results for a sphere in Stokes flow at low Reynolds number (Re < 1.0) and from wind tunnel data for Re > 1.0. The results show that both the data and the theoretical Stokes flow values are a linear function of Reynolds number but both experimental results fall well above the theoretical line. For example, the measured C_D for the highest Reynolds number measured in this study is 3.5 times higher than the published values in the literature (White, 2006; Munson, Young and Okiishi, 2002). Both the data from Ruck and Makiola (1988) and the data from this study fall roughly on the same trend line.

In order to determine the accuracy of the measurement method, particles were dropped down the chamber in quiescent air allowing the particles to reach their terminal velocity. In this instance the air within which the particle is traveling is not turbulent

unless induced by the particle. This experiment produced the drag coefficient shown at the lowest Reynolds number using a triangle symbol. For this condition, the measured value is 0.66 of the theoretical value which is within the uncertainty of the data given the spread in particle size and the uncertainty in velocity. The decrease in C_D with increasing Reynolds number suggests dominance in friction drag over form drag. These data suggest the same functional relationship or that friction drag is still dominant and yet greater for the particles in turbulent flow in comparison to particles in quiescent flow.

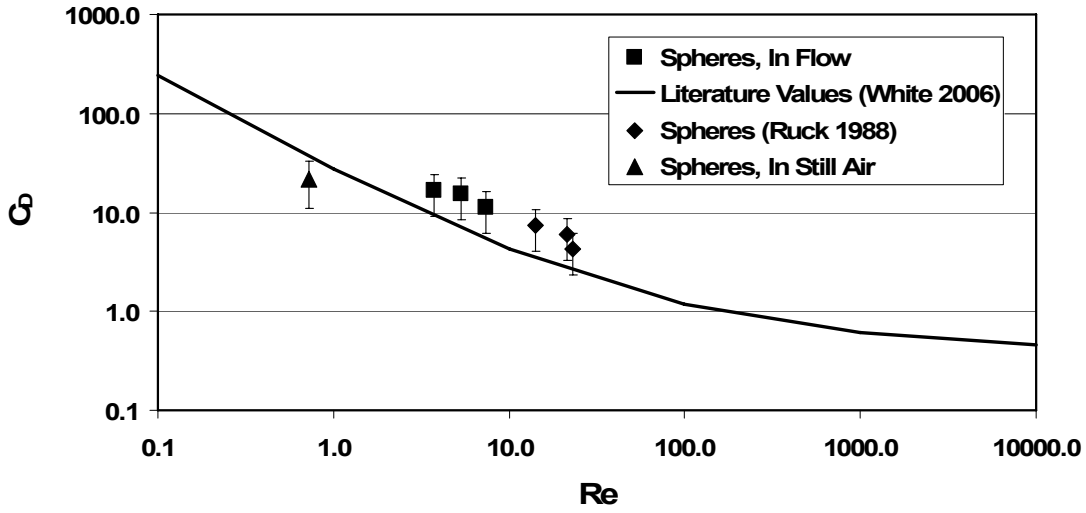

Figure 5-10 Coefficient of drag versus Reynolds number for spheres.

Like the spherical particles, the C_D's for the gravel shaped particles were estimated from the particle momentum equation. The results are shown in Figure 5.11. As can be seen in this figure, the C_D's for the gravel shaped particles measured in flowing air are above the published data for spheres. Whereas, the C_D's for the gravel shaped particles measured in still air are just below the published data (White, 2006) for spheres and flat plate theory.

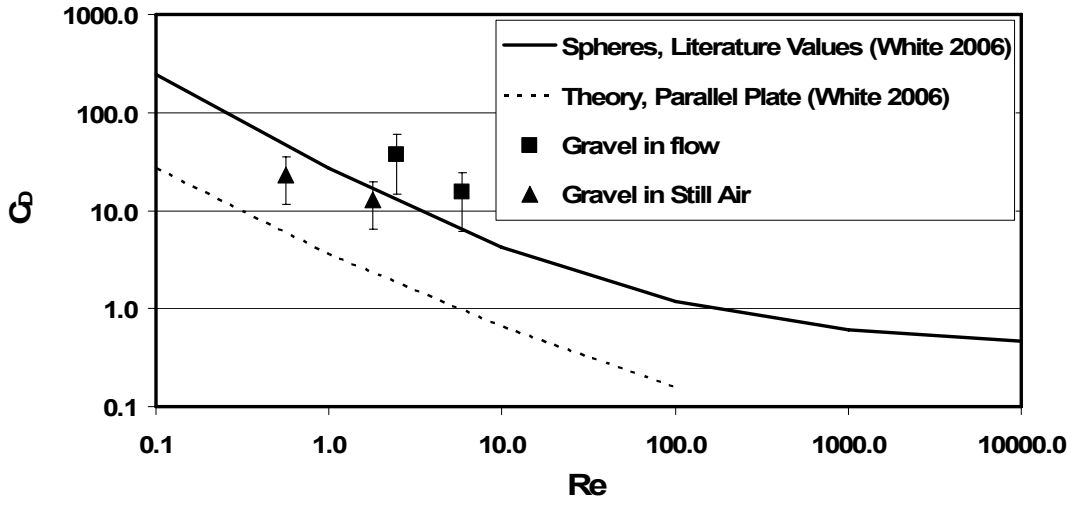

Figure 5-11 Coefficient of drag versus Reynolds number for gravel particles.

Drag coefficients for the cylindrical particles are shown in Figures 5.12, and 5.13 where C_D has been calculated based on flow parallel or perpendicular to the axis of the cylinder respectively. Each figure contains C_D measured in the turbulent backward facing step and using terminal velocity in the quiescent chamber. For cross flow or flow perpendicular to the cylinder, the cross sectional area of the cylinder is used. For parallel flow, the area is represented by the surface area around the circumference of the cylinder. Theoretical results for cylinders in parallel and cross flow can be found in the literature (White, 2006) which are analytical results for laminar flow and have been measured for stationary objects in turbulent flows. These results have been added to the figures as solid lines.

Assuming the cylinders are in parallel flow, the measured C_D in the step is 5 -10 times higher while the drag coefficient from the terminal velocity agrees well with published values. This agreement suggests that if the flow is not turbulent, the cylinders will align themselves with the flow producing friction drag along the length of the

cylinder. As with the spherical particles, the data shows the drag is significantly higher when in a flow that is already turbulent in comparison to a quiescent flow. It is interesting also to note that the drag appears to be independent of the Reynolds number although the range of Reynolds numbers measured is not very large. This suggests that drag is dominated by form or pressure drag and not by viscous or friction effects.

Assuming the cylinders are in cross flow produces a drag coefficient for the quiescent air that is significantly below published results indicating the cylinders are most likely aligning themselves parallel to the flow. Even though published values for C_D are

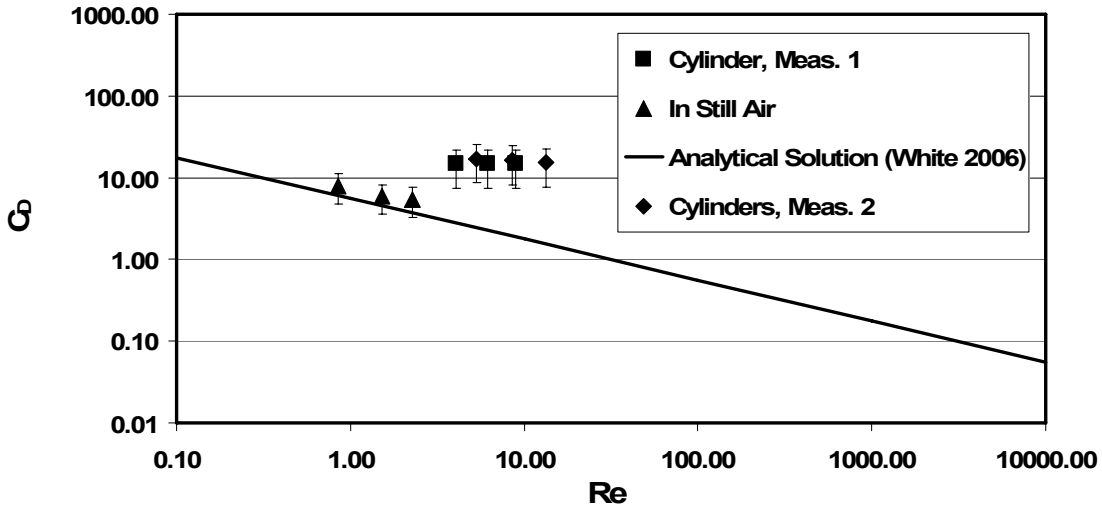

Figure 5-12 C_D versus Re for cylinders in parallel flow.

higher in cross flow, the measured C_D's are on the order of 3-5 times higher in the turbulent flow below the step. This is further indication that the turbulence is influencing the drag on the particles.

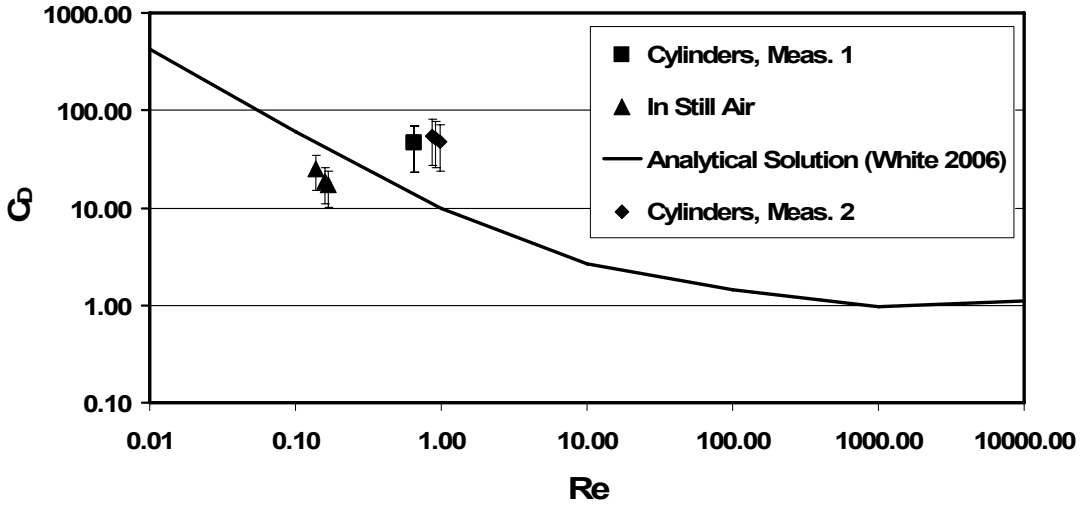

Figure 5-13 C_D versus Re for cylinders in perpendicular flow.

Finally, Figures 5-14 and 5-15 present the same data for the flakes in both parallel and perpendicular flow comparing the drag coefficients measured to the published analytical values and to the drag coefficients measured in quiescent air. These data are very similar to the cylindrical particle data. The flake drag coefficients for parallel flow agree some what close with published values when measured in quiescent air but the drag coefficients in the turbulent air below the step are on the order of 6 -21 times higher than the published values. In this case, data from two different locations in the step are shown. As with the cylinders, the results for these particles in the flow show that the C_D's for these cases are not a function of Reynolds number.

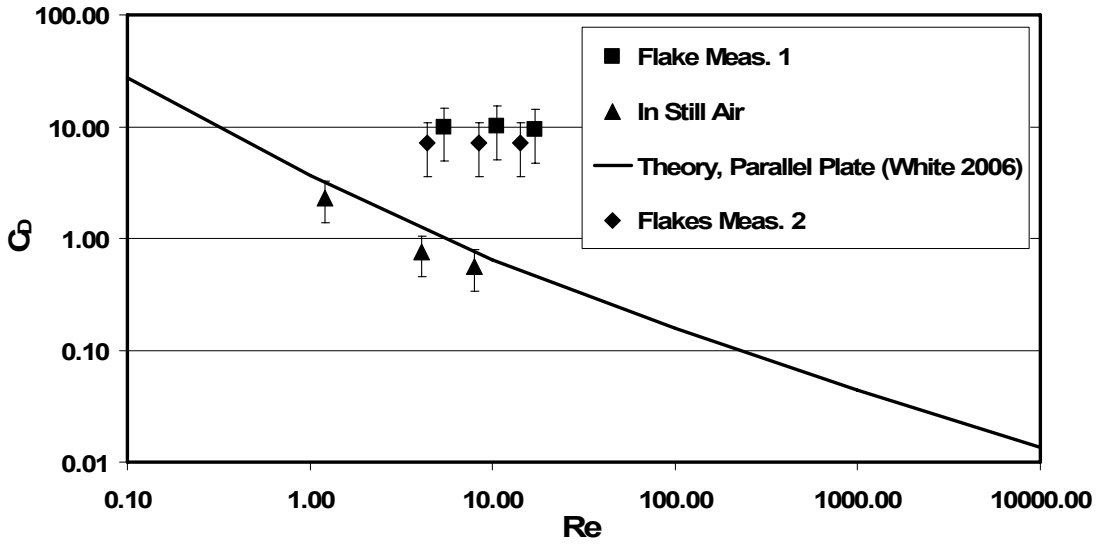

Figure 5-14 C_D versus Re for flakes in parallel flow.

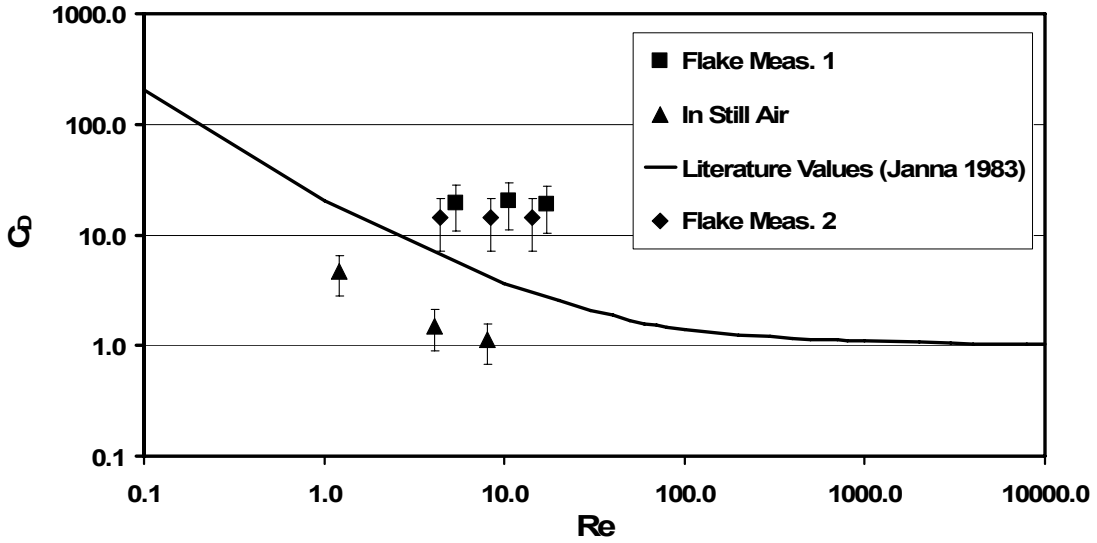

Figure 5-15 C_D versus Re for flakes in perpendicular flow.

5.4 Discussion of Results

The data presented in the previous section support two hypotheses: 1. Turbulence in the air produced independently of the relative velocity of the air and particles tend to increase the drag on particles and 2. For the relatively low Reynolds numbers investigated (0.5 – 30), the highly non-spherical particles (particle for which the projected area changes based on particle orientation) have a larger difference between the measured and published drag coefficients than spherical shaped particles. These non-spherical particles also appear to behave as if drag is pressure dominated (C_D is independent of Reynolds number) while particles for which the projected area is independent of orientation behave as if they are friction drag dominated (C_D decreases with increasing Reynolds number). It is of interest to discuss the physical phenomena which might produce such a result.

In order to understand the impact of turbulence, a numerical model was produced describing particle motion under the influence of a decelerating turbulent flow. The instantaneous gas phase velocity was represented by a sinusoidal function with a characteristic frequency and decreasing mean velocity as shown in Equation 5.4. This gas was assumed to produce a drag on the particle proportional to the velocity squared and characteristic area as shown in Equation 5.5. Because the model is an idealization of turbulence, it is not expected that the results will allow an accurate prediction of the drag coefficient, but rather the purpose is to determine if the instantaneous velocity which produces higher instantaneous relative velocities between the gas and particles for a portion of each oscillation can possibly be responsible for the increase in drag observed. For this reason the largest justifiable turbulent velocities will be selected for the model.

$$V_g = \left[\overline{V_1} + \left(\overline{V_2} - \overline{V_1} \right) \frac{x - x_1}{x_2 - x_1} \right] + \mathrm{V}' Sin\left(\frac{2\pi t}{\tau} \right) \tag{5.4}$$

Where: $\mathrm{V}' = \sqrt{2}\mathrm{V}_{\mathrm{rms}}$

$$\mathrm{m}_{\mathrm{P}} \frac{\mathrm{dV}_{\mathrm{P}}}{\mathrm{dt}} = \frac{1}{2} \mathrm{C}_{\mathrm{D}} \rho \mathrm{A} \left(\mathrm{V}_{\mathrm{p}} - \mathrm{V}_{\mathrm{g}} \right)^2 \tag{5.5}$$

The magnitude of the sinusoidal fluctuation, V′, was taken to be 1.414 times the rms turbulent velocity from LDV measurements. The period of the oscillation was determined from theoretical values of turbulence length scales. Three turbulence length scales are often discussed in the literature. The integral length scale, l_0 is associated with the large eddies that are created in the flow. In this application the large eddies can be thought of as on the order of the size of the recirculation zone behind the step. Typically, l_0, is selected as half the geometric length scale of the flow. In this case, 0.5 times the step height or 12.5 mm was selected. A second length scale of turbulence is the Taylor microscale which is a scale where velocities within the flow correlate, thus representing eddies within the flow which are shed or are produced by the integral length scale turbulence. A final length scale of turbulence is the smallest eddies capable of maintaining an identity before the bulk motion of the fluid is dissipated into random molecular motion through viscous dissipation. This scale is known as the Kolmogorov scale, l_k. Turns (2000) gives a correlation for the Taylor and Kolmogorov scales of turbulence for a jet based on Reynolds number as shown in Equations 5.6 and 5.7.

$$l_\lambda = \frac{l_0}{Re_{l_0}^{1/2}} \quad \textbf{(5.6)}$$

$$l_k = \frac{l_0}{Re_{l_0}^{3/4}} \quad \textbf{(5.7)}$$

Based on these two correlations the Taylor microscale and the Kolmogorov scale of turbulence at the points used to measure C_D are approximately 150 and 17 μm respectively. The Kolmogorov scale is smaller than the particles being measured but far too large to move within the boundary layer. The Taylor microscale is larger than the particle suggesting flow moves back and forth relative to the particle outside of the boundary layer with a given period. The period (τ) for turbulent fluctuations used in Equation 5.9 was based on this length scale and the time required for an eddie to rotate around a circle of characteristic diameter l_λ as shown in Equation 5.8

$$\tau = \frac{\pi l_\lambda}{V'} \quad \textbf{(5.8)}$$

The number of periods occurring between the two measured locations used to calculate the drag coefficient is calculated as shown in Equation 5.9, where the time to travel the measured path length is divided by the period. The time for a particle to travel along the measured distance is determined by dividing the distance by the average mean particle velocity. The velocity change of a particle can be predicted by applying

Equation 5.5 where the right hand side is the net force on the particle and the left side is the change in momentum. This equation can be integrated numerically given an assumed drag coefficient. A difficulty arises in integrating the equation because the relative velocity is squared and thus always positive regardless of whether the gas is slower or faster than the particle. This can be resolved by tracking the sign of the relative velocity as the equation is numerically integrated.

$$N_{cyc} = \frac{(x_2 - x_1)}{0.5(V_{p,1} + V_{p,2})\tau} \quad \textbf{(5.9)}$$

A result for a 41.5 μm spherical particle velocity in an oscillating gas is shown in Figure 5.16. This particle was calculated to see 19.6 turbulent oscillations over the 25.4 mm distance between the two measurements. The drag coefficient was adjusted until the initial and final particle velocities were equal to those of the measurement. In this case the required drag coefficient was $C_D = 5.3$. It is interesting to note that the mass of the particle is large enough to keep the particle from oscillating appreciably and could therefore be assumed not to oscillate in all of the particles measured. By decreasing the particle mass in the model enough to detect an oscillation it was observed that the particle was initially 90 degrees out of phase with the gas, but as the particle mass is further decreased, the oscillations decrease in both magnitude and phase difference with the gas velocity.

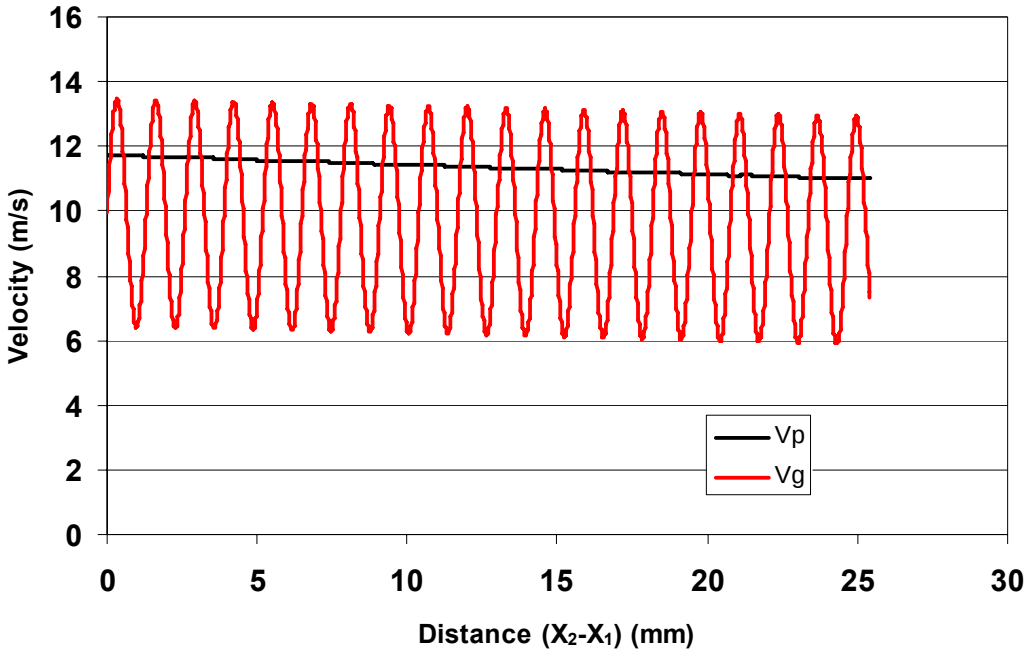

Figure 5-16 Model of a solid particle within an oscillating gas velocity between two positions in the backward facing step.

The model was used on each particle size and shape for which the drag coefficient was previously measured to produce a turbulent corrected drag coefficient versus a Turbulent Reynolds number (Re_T) based on the turbulent intensity. The results are shown in Figures 5.17 - 5.21.

The spherical and gravel shaped particles have been combined in the first figure because of the similarity in their geometry and because they both produce a drag coefficient which is now in better agreement with existing correlations. This analysis suggests that the higher drag coefficients measured on spheres and gravel shaped particle may merely be the result of using the average and not the instantaneous velocity of the particles in the drag calculation.

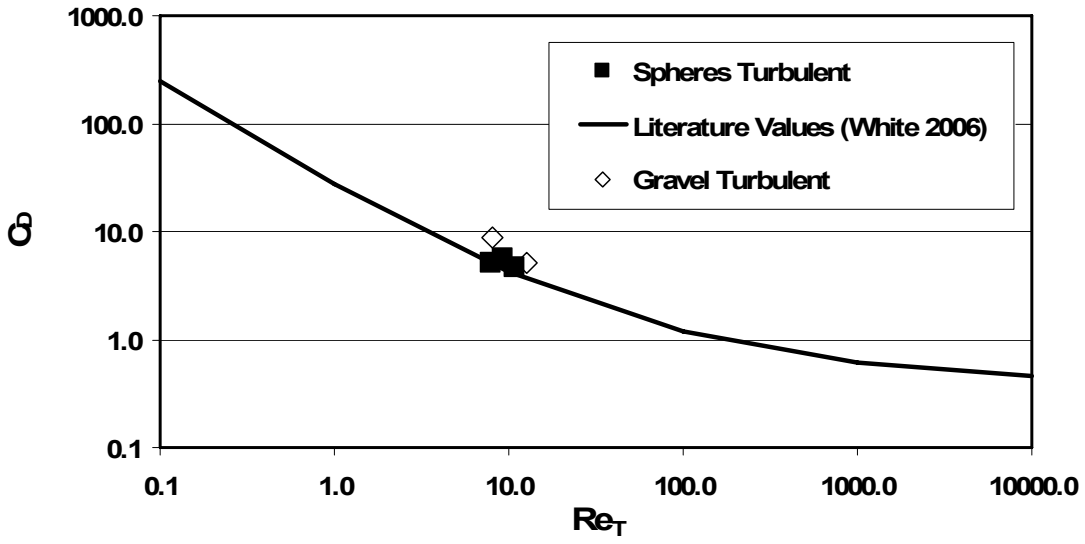

Figure 5-17 Drag coefficients for spherical and gravel shaped particles based on an instantaneous sinusoidal turbulent gas velocity between 9 and 10 step heights below the step.

Accounting for instantaneous velocities on cylinder improves the agreement between measured and previously correlated drag coefficients, but regardless of whether the particle is assumed to be oriented perpendicular or parallel to the flow, the measured drag is still higher. This leads one to suspect that the asphericity of the particle is a contributing factor to the drag and that the flow may be producing a change in orientation which supplements momentum exchange with the gas phase. The possibility of particle spin entraining fluid within the boundary layer which changes direction and creates turbulent structure in the vicinity of the particle has been suggested by others. (Brucato, Grisafi and Montante (1998))

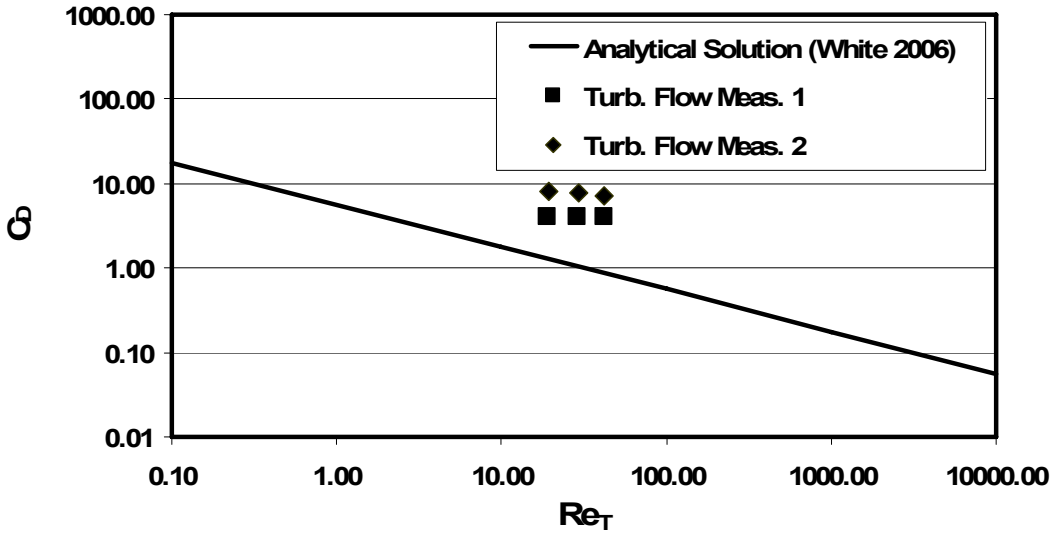

Figure 5-18 Drag coefficients for cylindrical shaped particles in parallel flow based on an instantaneous sinusoidal turbulent gas velocity at two locations below the step.

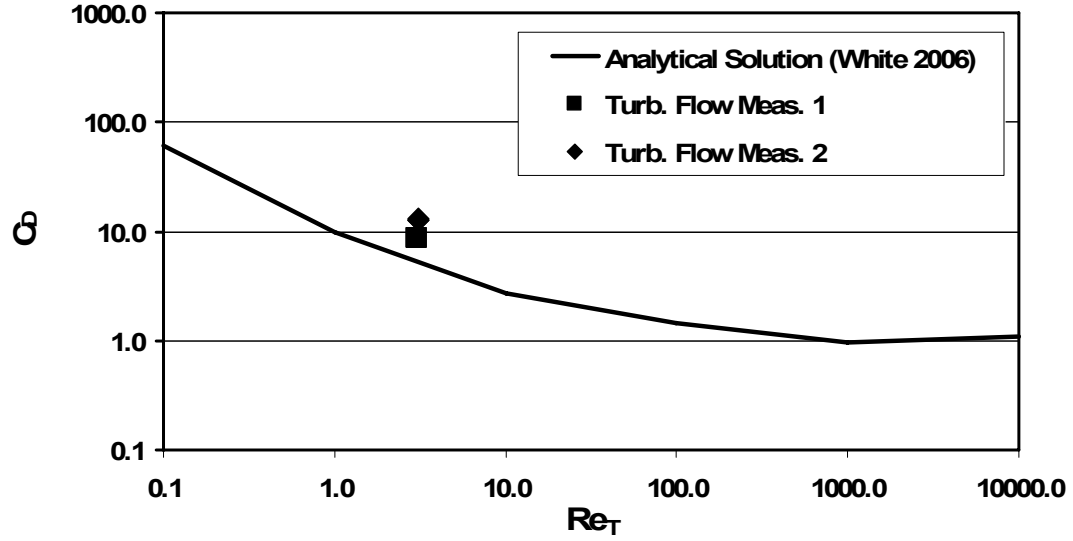

Figure 5-19 Drag coefficients for cylindrical shaped particles in perpendicular flow based on an instantaneous sinusoidal turbulent gas velocity at two locations below the step.

In the case of flakes or flat shaped particles, the drag coefficients adjusted for instantaneous velocity do not agree well with theoretical values in the case of plates in parallel flow but in comparison to a correlation for disks in cross flow, C_D agrees better. This result is consistent with the concept that the flow produces a spinning particle which creates an area around which the flow must move and pressure is not well recovered. In the case of the flake, the area represented by a perpendicular cross section is representative of the area which would be produced by a sphere which contains a spinning plate. This is not the case for the cylinder. A spinning cylinder could potentially produce a surface area proportional to the length squared while the area for either cross flow or parallel flow is proportional only to the area.

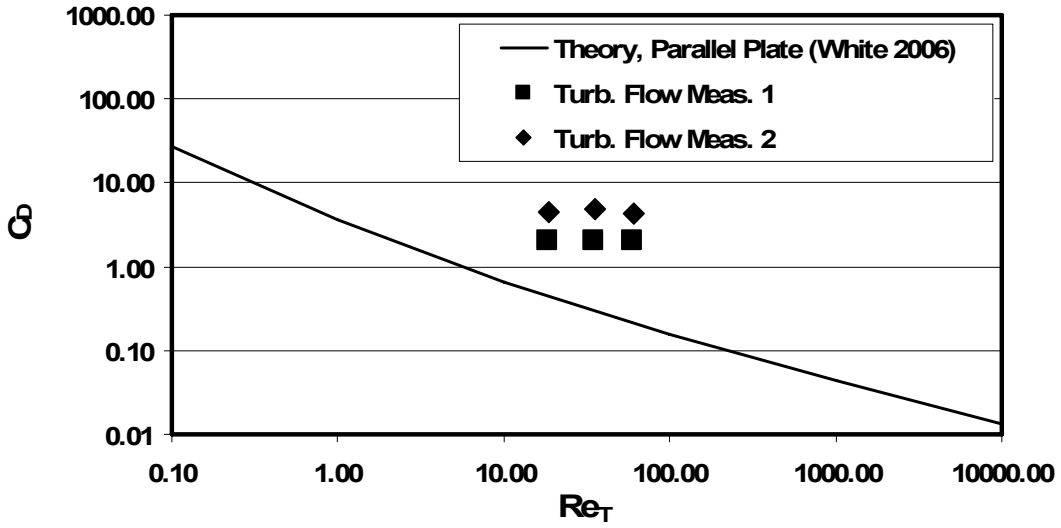

Figure 5-20 Drag coefficients for flat flake shaped particles in parallel flow based on an instantaneous sinusoidal turbulent velocity at two locations below the step.

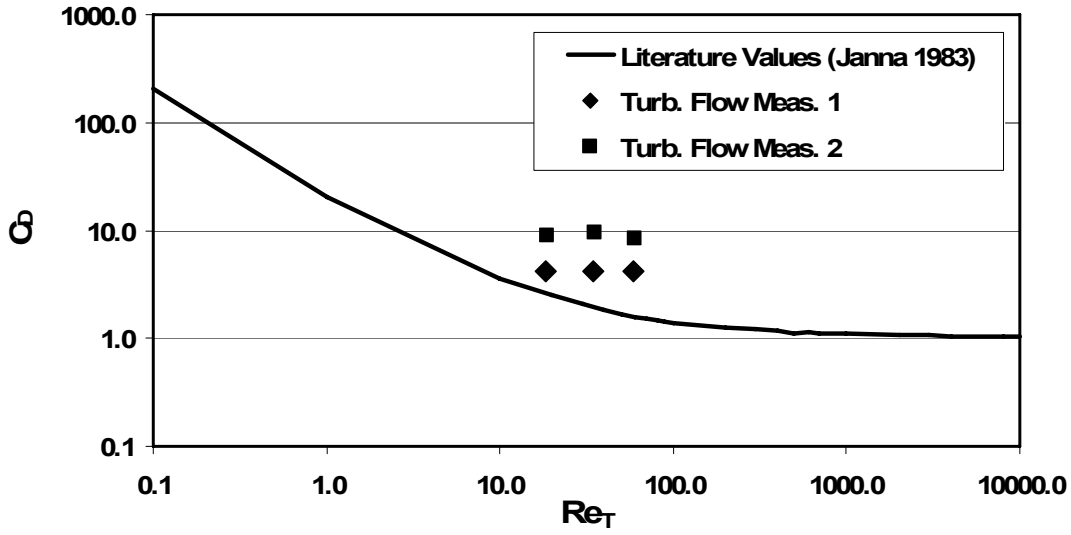

Figure 5-21 Drag coefficients for flake or flat shaped particles perpendicular to the flow based on an instantaneous sinusoidal turbulent gas velocity at two locations below the step.

6 Summary, Conclusions and Recommendations

6.1 Summary and Conclusions

The behavior of drag and slip on spherical and non-spherical particles in a backward facing step with turbulent flow was explored in this research. This provided information such as the drag coefficient for particles of various sizes and shapes which is a required parameter in CFD programs in order to predict and model particle flow.

The gas phase velocity was mapped throughout the chamber at 19 different places across 10 different axial locations below the step as a basis for providing the relative velocity necessary for calculating the slip and drag. Small seeded particles on the order of just a few microns were used to take these measurements. To test for repeatability these measurements were preformed at three different days and times. These results showed a reasonable repeatability thereby demonstrating the usefulness of this data.

In addition to these measurements, CFD modeling was completed using Fluent to predict the gas phase velocities. Generally good agreement between the model and measured data resulted at most places throughout the flow.

Three different sizes of spherical particles were measured at the same locations as the gas phase. The slip of these spherical particles was shown to increase roughly according to Equation 5.1 developed by Albrecht (1986) from the particle momentum

equation. The coefficient of drag was then calculated using the mean relative velocity (the difference between the mean particle velocity and mean gas phase velocity) in the particle momentum equation. The results showed that by using only the mean relative velocity in the particle momentum equation that the drag coefficients were significantly higher than correlations published in the literature. Additionally, the drag coefficients of spherical particles used in another study (Ruck 1988) were also shown to be in agreement with this data and higher than literature correlation. However, when the instantaneous fluctuating turbulent velocity was modeled as a sine wave, a drag coefficient consistent with literature values was obtained. In addition to the measurements being made in moving air, the spheres were dropped in still air and the terminal velocity measured and used in calculating the drag coefficient. The drag coefficient for the spheres in still air without turbulence when calculated showed it to be close to the literature values.

The velocities of six different sizes of gravel shaped particles were also measured throughout the backward facing step. To accurately measure the velocities of the gravel particles in order to calculate the slip and drag, the PMT of the laser system had to be turned down to a level that filtered out the small particle bias. Previous research done by others without adjusting the PMT has produced erroneous results showing no slip between the gas phase and these same types of particles in an accelerating flow. The slip of the gravel shaped particles was shown to be significant; however the magnitude of the slip was not as large as that for the spherical particles for similar sizes. The drag coefficient of some of these gravel particles were calculated using the particle momentum equation using the velocity measurements from this research. The results of these particles in the flow show the drag coefficients of these particles to lie just above the

literature values of the spheres. The drag coefficients of these particles in still air once they reached their terminal velocity were located in the literature values between a sphere and a flat plate.

Finally, the velocities of three different size distributions of cylindrical and flake shaped particles were measured at several locations in the backward facing step in order to calculate their slip and drag coefficients. Like the gravel shaped particles, adjustment of the PMT was required in order to measure the correct size distribution of the particles and thereby eliminate small particle bias from the measurements. The results of these measurements showed the velocity of all three different sizes of the cylindrical particles to be approximately the same in spite of their significantly different lengths and sizes. Likewise, the results of the flakes also showed them to have no significant difference in velocity among their three different sizes. This was significantly different than expected as the larger particles with more momentum were expected to slip more than the smaller particles.

The results of the drag coefficients using the mean relative velocity in the particle momentum equation showed the cylindrical shaped particles to have up to a 10 times higher coefficient of drag when compared with the published literature values. While the results of the flakes showed in some cases the drag coefficients to have up to a 21 times higher drag coefficient when using the mean relative velocity in the calculations.

However, unlike the spheres when an instantaneous velocity was modeled and used to calculate a drag coefficient, the coefficient of drag of the cylinders and flakes still remained significantly higher than the current literature values. As a comparison these particles were also dropped in still air and the terminal velocity measured. These results

showed the drag coefficient for both these types of particles in still air without turbulence to be very close to their literature values.

The results demonstrate that the drag coefficient of particles is significantly impacted by pre-existing turbulence in the flow field which has the effect of increasing drag. In the case of spherical or nearly spherical particles, the increased drag could be accounted for by considering the instantaneous velocity of the particles. For highly non spherical particles, the turbulence produces drag higher than can be accounted for considering instantaneous velocity. One possibility is that turbulence induces particle spin which alters the boundary layer causing separation and increased form drag on an area larger than the projected cross section. Not only the magnitude but the frequency of the turbulence appears to be important in determining the effect of the drag on the particle making a simple correlation between drag in turbulent and non turbulent flow challenging.

In conclusion, the main contribution of this research is twofold. First, it provides important experiment data for non-spherical particles flowing in a turbulent medium which is non-existent in past research. This was accomplished by using proper LDV laser measurement techniques that were developed in this work that ensure accurate measurements by eliminating small particle bias. Second, the drag coefficients calculated from the measured data of this research show that the current literature values which are largely based on particles in a non-turbulent medium are very inaccurate for non-spherical particles moving in a fluid with free stream turbulence even though they have the same Reynolds numbers. This is very important, since CFD codes require that

accurate drag coefficients be used in order to correctly predict or model the flow characteristics of particles.

6.2 Recommendations

The following recommendations for future research on this topic are as follows:

1. A particle image velocimetry (PIV) system equipped with shadow graphy would provide a technique for measuring the size, velocity and orientation of individual non-spherical particles. Knowing the orientation of a particle along with its velocity as it flows through a turbulent medium could provide valuable insight in being able to better predict and/or model the behavior of non-spherical particles.

2. More shapes and sizes of particles could be measured in order to develop a wider data base of drag coefficients for modeling turbulent particle flow.

3. In addition to measuring more sizes and shapes of particles, the entire flow regime should be explored to better understand the overall affect that turbulence has on drag for the different types of particles.

References

Albrecht, H. E., "Laser-Doppler-Stromungsmessung," Akademie-Verlag Berlin, Vol. 2, (1986)

Asia, L., Garcia, J. A., Cerecedo, L. M., I. G., Palacin, Calvo, E., "Particle Concentration and Local Mass Flux Measurements in Two-Phase Flows with PDA. Application to a stud on the Dispersion of Spherical Particles in a Turbulent Air Jet," Int. Journal of Multiphase Flow, Vol. 28, pp. 301 –324 (2002)

Bauckhage, K., "The Phase Doppler Difference Method, a New Laser Doppler Technique for Simultaneous Size and Velocity Measurements, Part 1," Part. Part. Syst. Charact., Vol. 5, pp. 16 –22 (1988)

Baxter, L. L., "Turbulent Transport of Particles," Dissertation, BYU, (1989)

Black, D. L., McQuay, M.Q., Bonin, M. P., "Laser-based Techniques for Particle-size Measurements: a Review of Sizing Methods and Their Industrial Application," Prog. In Energy and Comb. Sci. (1995)

Black, D. L., "Experimental Investigation of Particle Dispersion with Spherical and Nonspherical Particles," Dissertation, BYU (1997)

Benedict, L. H., Gould, R. D., "Near Wall Velocity Measurements in the Recirculation Zone of a Backwards Facing Step Flow," Proceedings of FEDSM'98 1998 ASME Fluids Engineering Division Summer Meeting June 21-25, pp. 1- 8 (1998)

Brucato, A., Grisafi, F., Montante, G., "Particle Drag Coefficients in Turbulent Fluids," Chemical Engineering Science, Vol. 53, No 18, pp. 3295 – 3314 (1998)

Clift, R., Grace, J. R., Weber, M. E., "Bubbles, Drops, and Particles," Academic Press, New York (1978)

Durst, F. and Naqwi, A., "Phase-Doppler anemometry and spray measurements," Advanced Combustion Science," In T. Someya (Ed), pp 80-85, Springer-Verlag, Berlin (1993)

Durst, F., Zare, M., "Laser Doppler Measurements in Two-Phase Flows," Proc. LDA Symp., pp. 403 – 429 (1975)

Fessler, J. R., E. K., Eaton, "Turbulence Modification by Particles in a Backward-Facing Step Flow," J. Fluid Mechanics, Vol. 394, pp. 97-117 (1999)

Fluent User Guide, Fluent Inc. (2005)

Ganser, G. H., "A Rational Approach to Drag Prediction of Spherical and Nonspherical Particles," Powder Technology, Vol. 77, pp. 143 – 152, (1993)

Haider, A., Levenspiel, O., "Drag Coefficient and Terminal Velocity of Spherical and Nonspherical Particles," Powder Technology, Vol 58, pp. 63-70, (1989)

Hardalupas, Y. and Liu, C. H., "Backscatter phase-Doppler anemometry for transparent non-absorbing spheres," Exp. in Fluids, Vol. 14, pp. 379-390 (1993)

Hardalupas, Y., Taylor, A. M. K. P, Whitelaw, J. H., "Particle Dispersion in a Vertical Round Sudden-Expansion Flow," Phil. Trans. R. Soc. Lond. A , Vol. 341, pp. 411 - 422 (1992)

Hartman, M., Trnka, O., Svoboda, K., "Free Settling of Nonspherical Particles," Ind. Eng. Chem. Res., Vol. 33, pp. 1979 – 1983 (1994)

Hishida, K., Ando, A., Maeda, M., "Experiments on Particle Dispersion in a Turbulent Mixing Layer, 'Intl. J. Multiphase Flow," Vol 13, pp. 181 – 194 (1992)

Houser, M. J. and Bachalo, W. D., "Extension of the phase/Doppler particle analyzer to submicron particle measurements," In Chigier N. and Stewart G. W. (Eds), Particle Sizing and Analysis, Proc. SPIE 573, pp. 57-66 (1985)

Janna, W. S., Introduction to Fluid Mechanics, Brooks/Cole Engineering Division, Belmont, California, (1983)

Kasagi, N., Matsunaga, A., "Three-Dimensional Particle-Tracking Velocimetry Measurement of Turbulence Statistics and Energy Budget in a Backward-Facing Step Flow," Int. J. Heat and Fluid Flow, pp. 477 – 485 (1995)

Kiger, K. T., Lasheras, J. C., "The Effect of Vortex Pairing on Particle Dispersion and Kinetic Energy Transfer in a Two-Phase Turbulent Shear Layer," J. Fluid Mech., Vol 302, pp. 149 – 178 (1995)

Kiger, K. T., Lasheras, J. C., "Dissipation Due to Particle/Turbulence Interaction in a Two-Phase, Turbulent Shear Layer," Phys. Fluids, Vol. 9, No. 10 (1997)

Kim, J., Kline, S. J., Johnston, J. P., "Investigation of a Reattaching Turbulent Shear Layer: Flow Over a Backward –Facing Step," J. of Fluids Engr., Vol. 102, pp. 302-308 (1980)

Klett, J. D., "Orientation Model for Particles in Turbulence," J. of Atmos. Sci., Vol. 52, pp. 2276 – 2285 (1995)

Liou, Meng-Sing, Singh, K. P., "Numerical Analysis of Turbine Coolant Passage Flows," ASME, Presented at the International Gas Turbine & Aeroengine Congress & Exhibition (1998)

Lu, Q.Q., Fontaine, J.R., Aubertin, G., "Particle Motion in Two-Dimensional Confined Turbulent Flows," Aerosol Science and Tech. Vol. 17, pp. 169 – 185 (1992)

McAndrew, D., Coppen, S., Rogers, C. B., "Measurement of Fluid Turbulence Along the Path of a Heavy Particle in a Back-ward Facing Step Flow," Int. J. of Multiphase Flow, Vol. 27, pp. 1517 – 1532 (2001)

Morgan, A. J., Barton, I. E., "Comparison of Lagrangian Tracking Schemes to Flow over a Backward-Facing Step," Communications in Num. Methods in Engr. Vol 16, pp. 831 – 837 (2000)

Munson, B. R., Young, D. F., Okiishi, T. H., Fundamentals of Fluid Mechanics, 4th Ed., Wiley, New York, (2002)

Nagwi, A. A., Durst, F., "Light Scattering Applied to LDA and PDA Measurements. Part 1, Theory and Numerical Treatments," Part. Part. Syst. Charact., Vol. 8, pp. 245 (1991)

Ower, E. and Pankhurst, R.C., "The measurement of Air Flow", Pergamon Press, Oxford, England (1977)

Ruck, B., Makiola, B., "Particle Dispersion in a Single-Sided Backward-Facing Step Flow," Int. J. Multiphase Flow, Vol. 14, No. 6, pp. 787 – 800 (1988)

Sankar, S. V., Bachalo, W. D., "Performance Analysis of Various Phase-Doppler Systems," 4th Intl. Congress on Optical Particle Sizing, Nuremberg, Germany (1995)

Sankar, S. V., Weber, B. J., Kamemoto, D. Y. and Bachalo, W. D., "Sizing fine particles with the phase Doppler interferometric technique," Appl. Opt., Vol. 30, pp. 4914-4920 (1991)

Shih, C., Ho, C., "Three-Dimensional Recirculation Flow in a Backward Facing Step," Journal of Fluids Engineering, Vol 116, pp. 229 – 232 (1994)

Shirolkar, J. S. "Modeling Turbulent Particle Dispersion in Dilute, Nonreacting Flows," Dissertation, BYU, (1996)

Sommerfeld, M. "Particle Dispersion in Turbulent Flow: The Effect of Particle Size Distribution," Part. Part. System Charact., Vol. 7, pp. 209 – 220 (1990)

Swamee, P. K., Ojha, C. S. P., "Drag Coefficient and Fall Velocity of Nonspherical Particles," Journal of Hydraulic Engineering, Vol. 117, pp. 660-667 (1991)

Swithenbank, J., Beer, J. M., Taylor, M., Abbot, D. and Mccreath, G. C., "A laser diagnostic technique for the measurement of droplet and particle size distributions," Progress in Astronautics and Aeronautics, Vol. 53, pp. 421-447 (1977)

Trang-Cong, S., Gay, M., Michaelides, E., "Drag Coefficients of Irregularly Shaped Particles,"Powder Technology, Vol. 139, pp. 21-32 (2003)

Turns, S. R., An Introduction to Combustion: concepts and applications, 2nd ed., McGraw Hill, Boston, (2000)

Wallner, E., Meiburg, E., "Vortex Pairing in Two-Way Coupled, Particle Laden Mixing Layers," Int. J. of Multiphase Flow, (2000)

Wang, L. P., Stock, D. E., "Dispersion of Heavy Particles by Turbulent Motion," J. of the Atmospheric Sciences, Vol 50, pp. 1897 – 1913 (1993)

White, F. M., Viscous Fluid Flow, 3rd Ed., McGraw- Hill, New York, 2006

Zhou, Q., Leschziner, M. A., "Modeling Particle Dispersion in Turbulent Recirculating Flow with an Anisotropy-Resolving Scheme," 1997 ASME Fluids Engineering Division Summer Meeting, FEDSM 97

Appendix A.

Gas Phase Velocities

Seeded Data (Gas Phase Velocities)

Distance from face (steps)	First Run	Second Run	Third Run
		Velocity (m/s)	
Step 1			
0.1	-0.82	-0.98	-0.96
0.2	-0.96	-0.89	-1.17
0.3	-1.13	-1.39	-1.22
0.4	-1.16	-1.33	-1.25
0.5	-1.19	-1.24	-1.24
0.6	-1.15	-1.08	-1.09
0.7	-0.57	-0.76	-0.82
0.8	0.41	1.01	0.49
0.9	3.45	4.45	3.89
1	7.93	9.11	8.31
1.1	11.84	12.60	12.17
1.2	13.50	13.84	13.74
1.3	14.24	14.43	14.51
1.4	14.69	14.87	14.97
1.5	14.81	14.91	14.9
1.6	14.64	14.73	14.43
1.7	14.15	14.13	14.31
1.8	13.44	13.17	13.28
1.9	11.99	11.57	12.09
Step 2			
0.1	-2.80	-3.07	-2.78
0.2	-2.75	-2.79	-2.75
0.3	-2.26	-2.28	-2.73
0.4	-1.77	-1.72	-1.66
0.5	-0.81	-1.03	-1.02
0.6	0.05	0.28	0.40
0.7	1.53	1.75	1.73
0.8	3.76	4.04	4.02
0.9	6.22	6.73	6.24
1	9.01	9.09	8.9
1.1	11.60	12.07	11.83
1.2	13.44	13.67	13.51
1.3	14.42	14.63	14.52
1.4	14.76	14.81	14.97
1.5	14.87	14.87	15.15
1.6	14.60	14.59	14.89
1.7	14.07	13.99	14.08
1.8	13.30	13.06	13.46
1.9	11.82	11.19	12.03

Distance from face (steps)	First Run	Second Run	Third Run
		Velocity (m/s)	
Step 3			
0.1	-3.61	-3.37	-3.55
0.2	-2.89	-2.91	-2.04
0.3	-1.97	-2.26	-1.32
0.4	-1.31	-1.16	-1.32
0.5	-0.24	0.03	-0.02
0.6	1.67	1.80	1.37
0.7	3.23	3.53	3.06
0.8	4.92	5.23	4.96
0.9	7.13	7.52	7.21
1	9.19	9.65	9.46
1.1	11.35	11.51	11.42
1.2	12.79	13.09	12.97
1.3	13.78	14.02	14.14
1.4	14.36	14.42	14.59
1.5	14.47	14.54	14.70
1.6	14.19	14.18	14.54
1.7	13.78	13.62	13.97
1.8	12.92	12.58	13.17
1.9	11.41	10.66	11.57
Step 4			
0.1	-2.58	-2.44	-2.32
0.2	-1.83	-1.76	-1.77
0.3	-1.01	-1.12	-0.67
0.4	0.27	0.12	0.06
0.5	0.59	1.54	1.85
0.6	3.10	2.73	3.66
0.7	4.28	4.77	5.00
0.8	5.69	6.43	6.65
0.9	8.25	7.86	8.33
1	9.70	9.24	10.12
1.1	11.26	11.35	11.68
1.2	12.56	12.15	12.85
1.3	13.52	13.19	13.64
1.4	14.02	13.74	14.12
1.5	13.99	13.79	14.07
1.6	13.76	13.72	13.30
1.7	13.33	13.00	13.22
1.8	12.19	12.18	11.96
1.9	10.70	10.56	9.86

Distance from face (steps)	First Run	Second Run	Third Run
		Velocity (m/s)	
Step 5			
0.1	-1.13	-1.28	-1.18
0.2	-0.33	-0.45	-0.43
0.3	0.71	0.69	0.31
0.4	1.52	1.31	1.65
0.5	2.700	2.38	2.29
0.6	4.35	4.11	3.79
0.7	5.73	5.41	5.26
0.8	7.08	6.45	6.29
0.9	8.46	8.28	8.06
1	9.69	9.50	9.37
1.1	11.13	10.55	10.71
1.2	11.96	11.91	11.84
1.3	12.80	12.24	12.33
1.4	13.09	12.99	12.85
1.5	13.28	12.94	13.00
1.6	12.82	12.77	12.59
1.7	12.24	12.18	11.94
1.8	11.40	11.14	11.3
1.9	9.74	9.15	9.72
Step 6			
0.1	1.09	0.74	1.03
0.2	1.41	1.37	1.37
0.3	2.30	2.00	2.22
0.4	3.23	2.82	2.97
0.5	4.19	3.74	4.12
0.6	4.90	5.00	4.62
0.7	6.17	6.28	5.77
0.8	7.39	6.95	6.64
0.9	8.36	8.07	8.49
1	9.40	9.22	9.29
1.1	10.47	9.65	10.38
1.2	11.11	11.03	10.96
1.3	11.67	11.74	11.85
1.4	11.87	11.94	11.94
1.5	11.73	11.67	11.86
1.6	11.21	11.05	11.88
1.7	10.78	10.84	11.07
1.8	9.68	9.90	10.03
1.9	7.96	8.32	8.79

Distance from face (steps)	First Run	Second Run	Third Run
		Velocity (m/s)	
Step 7			
0.1	3.42	3.23	2.09
0.2	4.08	3.66	3.02
0.3	5.03	4.36	3.55
0.4	5.37	4.49	4.20
0.5	5.78	4.93	4.76
0.6	6.77	5.98	5.86
0.7	7.49	6.35	6.83
0.8	8.01	7.45	7.47
0.9	9.04	8.83	8.18
1	9.78	9.20	9.10
1.1	10.34	10.17	9.92
1.2	10.74	10.69	10.39
1.3	10.97	10.86	10.75
1.4	10.98	11.04	10.98
1.5	11.05	10.82	11.09
1.6	10.37	10.78	9.87
1.7	9.72	9.79	9.80
1.8	9.11	9.07	8.86
1.9	7.91	7.73	7.64
Step 8			
0.1	4.87	4.17	3.47
0.2	5.33	4.63	4.54
0.3	5.79	5.15	4.76
0.4	6.13	5.18	5.08
0.5	6.57	6.31	5.64
0.6	7.48	6.56	6.23
0.7	8.05	7.77	7.14
0.8	8.63	8.34	7.47
0.9	9.05	8.76	8.04
1	9.77	8.98	9.04
1.1	10.08	9.75	9.35
1.2	10.32	9.89	9.53
1.3	10.17	9.91	9.84
1.4	10.22	10.36	9.30
1.5	10.06	10.13	10.4
1.6	9.72	9.48	8.92
1.7	8.82	8.92	8.83
1.8	7.96	8.33	8.00
1.9	6.90	7.12	7.24

Distance from face (steps)	First Run	Second Run Velocity (m/s)	Third Run
Step 9			
0.1	5.56	5.63	4.73
0.2	6.06	6.13	5.19
0.3	6.75	5.78	5.58
0.4	6.96	6.31	5.51
0.5	7.36	7.00	6.08
0.6	7.89	7.50	7.31
0.7	8.24	7.84	7.06
0.8	8.55	8.03	7.87
0.9	9.10	8.96	8.45
1	9.40	9.15	8.34
1.1	9.88	9.33	9.13
1.2	9.79	9.58	9.42
1.3	9.80	9.58	9.42
1.4	9.58	9.40	9.40
1.5	9.26	9.39	9.15
1.6	8.91	9.06	8.50
1.7	8.21	7.96	8.19
1.8	7.46	7.74	7.75
1.9	6.68	6.69	6.14
Step 12			
0.1	6.87	6.15	6.08
0.2	7.32	6.90	6.75
0.3	7.55	7.16	7.26
0.4	7.98	7.33	7.25
0.5	8.27	7.52	7.65
0.6	8.31	8.04	7.58
0.7	8.45	8.31	8.22
0.8	8.60	8.31	8.09
0.9	8.58	8.07	8.22
1	8.72	8.40	8.56
1.1	8.96	8.59	8.42
1.2	8.70	8.54	8.40
1.3	8.51	8.22	8.35
1.4	8.18	8.31	8.33
1.5	7.63	7.91	8.13
1.6	7.50	7.61	7.60
1.7	7.07	7.25	7.10
1.8	6.53	6.58	6.78
1.9	5.80	6.09	5.99

Appendix B.

Gas Phase RMS Velocities

Seeded Data (Gas Phase RMS)

Dist. from face (steps)	First Run	Second Run	Third Run
		Velocity (m/s)	
Step 1			
0.1	1.29	1.37	1.54
0.2	1.27	1.41	1.33
0.3	1.33	1.42	1.53
0.4	1.35	1.30	1.51
0.5	1.34	1.30	1.27
0.6	1.28	1.36	1.31
0.7	1.27	1.31	1.40
0.8	1.66	1.72	1.87
0.9	2.37	2.58	2.54
1	2.71	2.66	2.73
1.1	1.98	1.83	2.07
1.2	1.51	1.65	1.68
1.3	1.37	1.45	1.34
1.4	1.35	1.33	1.28
1.5	1.17	1.30	1.22
1.6	1.29	1.49	1.31
1.7	1.37	1.38	1.40
1.8	1.46	1.59	1.54
1.9	1.62	1.75	1.72
Step 2			
0.1	1.79	1.85	1.89
0.2	1.76	1.85	1.68
0.3	1.39	2.04	1.91
0.4	1.89	2.05	2.07
0.5	2.15	2.29	2.16
0.6	2.36	2.47	2.39
0.7	2.53	2.60	2.43
0.8	2.64	2.64	2.57
0.9	2.75	2.78	2.88
1	2.66	2.77	2.92
1.1	2.40	2.28	2.38
1.2	1.71	1.76	2.06
1.3	1.36	1.59	1.47
1.4	1.37	1.23	1.28
1.5	1.28	1.29	1.40
1.6	1.40	1.40	1.35
1.7	1.56	1.56	1.48
1.8	1.58	1.69	1.69
1.9	1.65	1.95	1.75

Dist. from face (steps)	First Run	Second Run Velocity (m/s)	Third Run
Step 3			
0.1	1.66	1.84	1.81
0.2	1.96	2.14	2.10
0.3	2.27	2.25	2.47
0.4	2.66	2.67	2.74
0.5	2.90	3.01	3.04
0.6	3.17	3.10	3.10
0.7	3.09	3.36	3.35
0.8	2.98	3.19	3.31
0.9	3.15	3.28	3.13
1	2.80	2.86	2.95
1.1	2.47	2.69	2.67
1.2	2.25	2.24	2.26
1.3	1.88	1.82	1.99
1.4	1.56	1.72	1.77
1.5	1.39	1.51	1.50
1.6	1.40	1.62	1.57
1.7	1.54	1.84	1.67
1.8	1.86	1.81	1.92
1.9	2.04	2.15	2.19
Step 4			
0.1	2.11	2.14	2.27
0.2	2.60	2.39	2.46
0.3	2.73	2.76	2.91
0.4	3.27	3.07	3.18
0.5	2.90	3.36	3.59
0.6	3.33	3.10	3.55
0.7	4.28	3.59	3.50
0.8	3.68	3.46	3.37
0.9	3.22	3.14	3.36
1	2.93	3.17	2.93
1.1	2.83	2.66	2.68
1.2	2.45	2.46	2.18
1.3	1.97	1.99	2.22
1.4	1.78	1.64	2.07
1.5	1.90	1.81	1.82
1.6	1.83	1.99	2.12
1.7	1.86	2.00	2.05
1.8	2.28	2.34	1.99
1.9	2.30	2.32	2.61

Dist. from face (steps)	First Run	Second Run Velocity (m/s)	Third Run
Step 5			
0.1	2.57	2.58	2.51
0.2	2.73	2.91	2.77
0.3	3.16	3.09	3.18
0.4	3.27	3.42	3.35
0.5	3.61	3.69	3.48
0.6	3.68	3.56	3.67
0.7	3.96	3.84	3.54
0.8	3.37	3.39	3.42
0.9	3.37	3.27	3.40
1	3.22	3.30	3.28
1.1	2.80	3.04	2.89
1.2	2.69	2.70	2.50
1.3	2.20	2.52	2.61
1.4	2.39	2.29	2.11
1.5	2.42	2.33	2.09
1.6	2.31	2.15	2.38
1.7	2.42	2.38	2.40
1.8	2.56	2.50	2.30
1.9	2.64	2.61	2.72
Step 6			
0.1	2.74	2.78	2.98
0.2	3.00	2.83	3.07
0.3	3.04	3.12	3.06
0.4	3.36	2.82	3.20
0.5	3.48	3.46	3.46
0.6	3.49	3.63	3.47
0.7	3.50	3.55	3.30
0.8	3.53	3.50	3.43
0.9	3.39	3.51	3.09
1	3.31	3.30	3.08
1.1	3.00	3.49	2.88
1.2	2.69	2.70	2.92
1.3	2.62	2.48	2.43
1.4	2.61	2.60	2.56
1.5	2.49	2.60	2.46
1.6	2.59	2.50	2.29
1.7	2.73	2.57	2.26
1.8	2.71	2.61	2.77
1.9	2.91	2.83	2.88

Dist. from face (steps)	First Run	Second Run Velocity (m/s)	Third Run
Step 7			
0.1	2.68	2.82	2.09
0.2	2.87	2.79	2.85
0.3	2.98	3.27	3.04
0.4	3.03	3.24	2.98
0.5	3.21	3.13	3.11
0.6	3.29	3.25	3.14
0.7	3.16	3.31	3.36
0.8	3.25	3.32	3.29
0.9	3.10	3.26	3.11
1	3.01	3.43	3.16
1.1	2.91	2.87	3.10
1.2	2.85	2.65	2.80
1.3	2.65	2.84	3.01
1.4	2.70	2.79	2.57
1.5	2.54	3.00	2.47
1.6	2.67	2.62	2.76
1.7	2.68	2.90	2.64
1.8	2.67	2.81	2.64
1.9	2.61	2.78	2.89
Step 8			
0.1	2.53	2.66	2.49
0.2	2.71	2.58	2.70
0.3	2.68	2.82	2.65
0.4	2.80	2.84	2.87
0.5	2.89	3.11	3.02
0.6	2.94	3.17	2.89
0.7	3.02	3.13	3.08
0.8	2.99	3.17	3.03
0.9	2.99	3.12	2.91
1	2.92	3.19	3.01
1.1	2.88	3.02	3.03
1.2	2.66	2.90	2.88
1.3	2.58	3.10	2.66
1.4	2.64	2.88	3.21
1.5	2.61	2.65	2.37
1.6	2.52	3.03	2.74
1.7	2.67	3.01	2.73
1.8	2.77	2.73	2.59
1.9	2.68	2.64	2.37

Dist. from face (steps)	First Run	Second Run	Third Run
		Velocity (m/s)	
Step 9			
0.1	2.41	2.75	2.32
0.2	2.47	2.61	2.36
0.3	2.68	2.52	2.41
0.4	2.67	2.55	2.48
0.5	2.81	2.73	2.66
0.6	2.64	2.71	2.69
0.7	2.75	2.80	2.79
0.8	2.77	2.93	2.84
0.9	2.82	2.93	2.90
1	2.79	2.85	3.03
1.1	2.73	2.79	2.70
1.2	2.60	2.80	2.69
1.3	2.64	2.80	2.68
1.4	2.50	2.86	2.62
1.5	2.45	2.48	2.54
1.6	2.48	2.31	2.54
1.7	2.45	2.56	2.47
1.8	2.53	2.29	2.33
1.9	2.48	2.51	2.48
Step 12			
0.1	2.02	1.98	1.91
0.2	1.95	1.82	2.07
0.3	2.00	2.04	1.92
0.4	2.10	2.15	2.08
0.5	2.07	2.16	2.11
0.6	2.11	2.17	2.15
0.7	2.11	2.12	2.21
0.8	2.25	2.13	2.17
0.9	2.15	2.24	2.39
1	2.22	2.22	2.20
1.1	2.22	2.20	2.23
1.2	2.18	2.03	2.03
1.3	2.09	2.05	2.09
1.4	2.09	2.09	2.03
1.5	2.19	2.04	2.02
1.6	2.08	1.90	2.08
1.7	2.18	2.01	1.93
1.8	2.15	2.00	2.01
1.9	1.98	1.99	2.01

Appendix C.
Spherical Particle Velocities

Spherical Particle Data

Distance from face (steps)	Diameter 38-45µm	45-53µm	53-61µm
	Velocity (m/s)		
Step 1			
0.1	-0.86	0.09	-1.27
0.2	-1.01	-0.30	-0.63
0.3	-1.17	-0.76	-1.08
0.4	-1.11	-1.13	-1.87
0.5	-1.26	-0.52	-0.47
0.6	-0.87	-2.33	0.08
0.7	-0.90	-0.85	0.23
0.8	-0.35	0.30	0.81
0.9	1.67	5.34	4.37
1	9.60	10.68	10.78
1.1	11.98	12.43	12.12
1.2	13.14	13.32	13.10
1.3	13.83	13.95	13.86
1.4	14.26	13.90	13.76
1.5	14.46	14.48	14.35
1.6	14.54	14.22	14.19
1.7	14.21	13.85	13.76
1.8	13.21	13.10	13.16
1.9	12.60	12.08	12.34
Step 2			
0.1	-2.12	-2.69	-0.17
0.2	-4.02	-2.04	-2.44
0.3	-2.14	-3.09	-1.38
0.4	-2.32	-1.81	0.88
0.5	-1.63	0.45	0.55
0.6	0.15	-1.93	2.82
0.7	2.50	4.69	4.40
0.8	4.15	7.71	6.55
0.9	6.77	9.30	10.11
1	10.33	10.87	10.71
1.1	11.82	12.34	12.17
1.2	13.07	13.44	13.20
1.3	14.03	14.09	13.69
1.4	14.45	14.38	14.13
1.5	14.51	14.59	14.29
1.6	14.42	14.10	14.20
1.7	13.88	13.83	13.93
1.8	13.30	13.14	13.43
1.9	12.51	11.74	12.37

Distance from face (steps)	38-45µm	45-53µm	53-61µm
		Velocity (m/s)	
Step 3			
0.1	-2.62	-3.41	-1.51
0.2	-2.85	-1.87	0.39
0.3	-1.93	-4.00	0.19
0.4	-1.34	-1.32	1.11
0.5	0.17	3.97	4.43
0.6	2.24	1.96	3.54
0.7	3.55	2.24	6.03
0.8	7.56	7.28	8.23
0.9	9.05	10.11	10.11
1	10.28	10.87	10.92
1.1	11.80	12.37	12.14
1.2	12.93	13.32	13.20
1.3	13.83	13.93	13.92
1.4	14.40	14.31	14.28
1.5	14.53	14.26	14.30
1.6	14.44	14.34	14.15
1.7	14.07	13.76	13.97
1.8	13.29	13.16	13.28
1.9	12.08	11.40	12.23
Step 4			
0.1	-1.41	-1.93	-0.05
0.2	-1.84	-2.06	0.82
0.3	-1.40	0.04	-0.18
0.4	0.82	1.64	3.11
0.5	4.12	5.36	4.70
0.6	5.40	4.75	7.55
0.7	7.91	7.14	9.04
0.8	9.53	9.25	9.16
0.9	10.07	10.00	9.95
1	11.25	10.88	10.97
1.1	11.90	11.89	12.05
1.2	13.12	12.89	12.89
1.3	13.98	13.71	13.88
1.4	14.30	14.18	14.33
1.5	14.44	14.21	14.20
1.6	14.28	14.06	14.14
1.7	13.65	13.81	13.62
1.8	12.85	12.97	12.80
1.9	11.80	12.01	11.83

Distance from face (steps)	38-45µm	45-53µm	53-61µm
		Velocity (m/s)	
Step 5			
0.1	0.19	-0.67	1.84
0.2	1.05	0.39	1.87
0.3	3.47	0.68	2.20
0.4	3.99	3.26	6.05
0.5	4.86	4.84	6.67
0.6	7.45	7.14	8.23
0.7	8.97	8.11	8.47
0.8	9.46	9.00	9.59
0.9	10.43	10.27	10.45
1	11.29	11.10	11.14
1.1	12.43	11.88	12.04
1.2	12.85	12.72	13.07
1.3	13.55	13.38	13.42
1.4	13.97	13.86	13.94
1.5	14.05	13.93	13.93
1.6	13.83	13.74	13.73
1.7	12.99	13.36	13.30
1.8	12.54	12.54	13.02
1.9	11.14	11.42	11.50
Step 6			
0.1	1.26	2.56	2.96
0.2	2.71	3.28	2.27
0.3	2.71	4.10	4.27
0.4	4.31	3.26	5.26
0.5	6.17	6.67	6.95
0.6	7.92	7.88	7.21
0.7	8.20	9.19	9.09
0.8	9.37	9.57	9.56
0.9	10.64	10.32	10.34
1	11.42	11.27	11.17
1.1	12.13	12.00	12.16
1.2	12.61	12.40	12.67
1.3	12.98	12.89	13.28
1.4	13.37	13.47	13.55
1.5	13.48	13.39	13.38
1.6	13.18	13.30	13.29
1.7	12.64	12.76	12.88
1.8	11.55	12.01	12.16
1.9	10.28	10.90	10.82

Distance from face (steps)	38-45µm	45-53µm	53-61µm
		Velocity (m/s)	
Step 7			
0.1	3.51	3.27	2.07
0.2	4.04	4.74	5.21
0.3	4.60	6.12	4.96
0.4	6.35	6.76	6.70
0.5	6.93	7.27	8.06
0.6	7.52	8.27	8.80
0.7	8.13	9.07	9.80
0.8	9.28	9.60	9.92
0.9	9.76	10.51	10.63
1	11.03	11.10	11.57
1.1	11.31	11.81	12.11
1.2	11.94	12.14	12.34
1.3	12.21	12.58	12.72
1.4	12.40	12.77	13.06
1.5	12.73	12.48	13.07
1.6	12.38	12.26	12.68
1.7	12.07	11.57	11.89
1.8	11.10	10.91	10.99
1.9	9.81	9.71	10.22
Step 8			
0.1	3.98	5.02	6.06
0.2	5.26	4.83	6.49
0.3	5.33	5.97	6.17
0.4	6.41	6.56	7.67
0.5	7.52	7.64	8.39
0.6	7.81	8.63	9.09
0.7	8.88	9.36	10.31
0.8	9.53	9.79	9.96
0.9	9.99	10.53	10.47
1	10.45	10.92	11.24
1.1	11.26	11.38	11.72
1.2	11.77	11.76	11.70
1.3	11.80	12.07	12.21
1.4	11.73	12.12	12.42
1.5	11.59	11.93	12.51
1.6	11.41	11.33	12.05
1.7	10.58	10.85	11.50
1.8	10.35	10.19	10.47
1.9	8.94	9.06	9.45

Distance from face (steps)	38-45µm	45-53µm	53-61µm
		Velocity (m/s)	
Step 9			
0.1	4.83	5.05	5.77
0.2	6.25	5.77	4.77
0.3	6.46	6.43	7.41
0.4	6.84	6.84	7.67
0.5	7.63	7.79	8.56
0.6	8.83	8.62	8.98
0.7	9.14	9.51	9.82
0.8	9.51	9.59	9.74
0.9	9.96	10.51	10.47
1	10.39	10.92	11.14
1.1	10.67	11.06	11.64
1.2	11.10	11.18	11.70
1.3	10.97	11.60	11.97
1.4	10.99	11.30	11.72
1.5	10.92	10.71	11.30
1.6	10.15	10.63	10.77
1.7	10.04	9.89	10.51
1.8	9.24	9.26	9.74
1.9	8.36	8.40	8.77
Step 12			
0.1	6.41	6.19	6.51
0.2	6.81	7.78	6.69
0.3	7.01	7.42	7.72
0.4	7.55	7.94	8.29
0.5	7.93	8.15	8.90
0.6	8.04	8.88	9.19
0.7	9.04	9.40	9.50
0.8	9.10	9.34	9.73
0.9	9.55	9.69	10.01
1	9.44	9.59	10.13
1.1	9.84	9.84	10.03
1.2	9.58	9.69	10.32
1.3	9.13	9.62	10.17
1.4	8.95	9.64	9.99
1.5	9.11	9.06	9.40
1.6	8.65	8.88	9.18
1.7	8.36	8.30	8.63
1.8	7.56	7.65	8.06
1.9	6.79	6.58	7.13

Appendix D.
Gravel Shaped Particle Velocities

Gravel Particle Data

	Sieve Size					
	38-45µm	45-53µm	53-61µm	75-90µm	90-106µm	106-125µm
Dist. from face	Velocity (m/s)					
Step 1						
0.1	-0.50	-0.67	-1.08			
0.2	-1.08	-1.14	-0.49			
0.3	-1.60	-1.09	-1.07			
0.4	-1.28	-1.25	-1.16			
0.5	-0.83	-1.34	-1.20			
0.6	-1.05	-0.64	-0.90			
0.7	-0.56	-0.64	-1.08			
0.8	0.27	-0.27	-0.10			
0.9	2.86	1.98	3.12			
1	8.43	8.65	8.29	8.92	8.21	
1.1	11.66	11.36	11.44	12.07	11.94	
1.2	13.24	13.04	12.98	13.24	13.18	
1.3	13.94	13.74	13.79	13.92	13.78	
1.4	14.33	14.12	14.01	14.17	14.28	
1.5	14.25	14.34	14.14	14.41	14.53	
1.6	14.08	14.26	14.03	14.43	14.43	
1.7	13.84	13.72	13.58	13.96	14.01	
1.8	12.89	12.89	13.07	13.14	13.39	
1.9	11.53	11.84	11.98	12.01	12.09	
Step 2						
0.1	-2.63	-2.36	-2.71			
0.2	-2.89	-3.06	-2.91			
0.3	-2.38	-2.79	-2.40			
0.4	-1.66	-1.97	-2.14			
0.5	-1.19	-1.22	-1.84			
0.6	0.03	-0.54	-0.45			
0.7	0.59	1.68	1.07			
0.8	3.39	3.43	2.86			
0.9	6.48	7.51	5.66			
1	9.49	9.45	8.95	9.68	9.52	
1.1	11.31	11.27	11.03	11.63	11.61	
1.2	13.07	12.96	12.69	13.20	12.86	
1.3	14.05	13.88	13.53	13.98	14.02	
1.4	14.42	14.16	13.98	14.30	14.22	
1.5	14.50	14.31	14.01	14.42	14.52	
1.6	14.24	14.01	13.97	14.35	14.30	
1.7	13.77	13.66	13.48	13.98	13.89	
1.8	12.98	13.01	12.81	13.13	13.37	
1.9	11.82	11.82	11.74	12.20	12.24	

	Sieve Size					
	38-45µm	45-53µm	53-61µm	75-90µm	90-106µm	106-125µm
Dist. from face			Velocity (m/s)			
Step 3						
0.1	-2.95	-3.23	-3.10			
0.2	-2.98	-3.13	-3.09			
0.3	-1.94	-2.25	-2.45			
0.4	-1.21	-1.67	-1.65			
0.5	0.17	-0.39	-0.21			
0.6	1.75	1.35	0.86			
0.7	3.45	3.57	2.80			
0.8	6.23	5.28	5.03			
0.9	8.32	7.46	7.70			
1	9.85	9.93	9.59	9.68	9.67	
1.1	11.74	11.46	11.15	11.74	11.64	
1.2	13.03	12.77	12.44	12.81	12.72	
1.3	13.79	13.66	13.33	13.74	13.70	
1.4	14.14	14.13	13.88	14.21	14.24	
1.5	14.31	14.21	14.09	14.34	14.23	
1.6	14.20	14.02	13.91	14.11	14.23	
1.7	13.76	13.57	13.41	13.76	13.87	
1.8	12.84	12.81	12.79	13.30	13.15	
1.9	11.27	11.33	11.49	11.69	12.05	
Step 4						
0.1	-2.23	-2.05	-2.74			
0.2	-1.84	-1.48	-1.97			
0.3	-0.86	-1.56	-0.62			
0.4	-0.27	0.22	-0.32			
0.5	1.61	1.26	0.83			
0.6	3.00	3.01	2.80			
0.7	4.61	3.97	4.91			
0.8	6.80	6.23	6.85			
0.9	8.51	8.48	8.20			
1	9.90	10.04	10.05	9.58	9.52	
1.1	11.17	11.29	11.05	11.18	11.42	
1.2	12.36	12.34	12.28	12.43	12.39	
1.3	13.23	13.21	13.17	13.32	13.37	
1.4	13.89	13.61	13.65	14.11	13.99	
1.5	14.03	13.95	13.79	14.37	14.29	
1.6	13.66	13.77	13.73	14.25	14.41	
1.7	13.25	13.24	13.20	13.95	14.01	
1.8	12.45	12.34	12.44	13.30	13.60	
1.9	11.33	11.11	11.09	12.47	12.56	

	Sieve Size					
	38-45µm	45-53µm	53-61µm	75-90µm	90-106µm	106-125µm
Dist. from face	Velocity (m/s)					
Step 5						
0.1	-0.74	-0.81	-1.17			
0.2	-0.11	-0.68	-0.61			
0.3	0.59	1.00	0.33			
0.4	1.60	1.34	2.02			
0.5	2.96	1.89	2.79			
0.6	4.35	4.98	4.66			
0.7	5.96	5.71	7.65			
0.8	7.44	7.61	8.19			
0.9	9.02	8.90	9.38			
1	10.02	10.00	10.28	10.27	9.95	
1.1	11.26	11.13	11.13	11.28	11.24	
1.2	12.31	11.95	12.20	12.39	12.26	
1.3	12.70	12.82	12.75	13.18	13.24	
1.4	13.15	13.29	13.12	13.90	13.56	
1.5	13.27	13.22	13.51	13.70	13.83	
1.6	13.15	13.18	13.10	13.74	13.80	
1.7	12.52	12.80	12.66	13.54	13.52	
1.8	11.68	12.10	11.65	12.87	12.92	
1.9	10.38	10.45	10.50	11.70	11.79	
Step 6						
0.1	0.55	0.65	0.57			
0.2	1.69	1.39	1.41			
0.3	2.51	1.98	2.83			
0.4	2.74	2.87	3.14			
0.5	5.07	4.50	4.52			
0.6	5.61	5.03	5.89			
0.7	7.01	6.68	6.69			
0.8	8.13	7.81	8.11			
0.9	9.15	9.21	9.16			
1	10.24	9.97	10.24	10.18	9.87	
1.1	11.16	10.91	11.29	11.22	11.20	
1.2	11.84	11.81	11.80	12.17	12.12	
1.3	12.29	12.31	12.50	12.89	12.86	
1.4	12.57	12.66	12.70	13.33	13.14	
1.5	12.61	12.82	12.70	13.30	13.14	
1.6	12.58	12.50	12.42	13.39	13.19	
1.7	12.00	11.91	11.86	12.98	12.96	
1.8	11.08	10.81	10.98	12.32	12.32	
1.9	9.84	9.87	9.68	11.42	11.52	

	Sieve Size					
	38-45µm	45-53µm	53-61µm	75-90µm	90-106µm	106-125µm
Dist. from face	Velocity (m/s)					
Step 7						
0.1	2.22	2.25	2.37			
0.2	3.31	2.32	2.92			
0.3	3.59	3.95	3.74			
0.4	4.41	4.95	4.56			
0.5	5.75	6.98	5.35			
0.6	6.68	7.15	6.29			
0.7	7.43	7.44	7.25			
0.8	8.48	8.16	8.12			
0.9	9.23	9.75	8.62			
1	10.22	10.23	9.75	10.11	9.93	10.03
1.1	10.79	10.72	10.55	10.83	10.97	11.08
1.2	11.17	11.41	11.23	11.59	11.58	11.61
1.3	11.70	11.75	11.62	12.08	11.99	12.02
1.4	11.77	11.95	12.09	12.43	12.31	12.39
1.5	11.64	11.66	11.87	12.48	12.45	12.50
1.6	11.38	11.64	11.76	12.26	12.19	12.00
1.7	10.68	11.07	11.24	11.69	12.08	11.94
1.8	9.91	10.05	10.34	11.30	11.13	11.05
1.9	8.73	9.12	9.23	9.87	10.20	9.97
Step 8						
0.1	3.29	3.66	3.28			
0.2	4.12	4.21	4.39			
0.3	4.70	4.90	4.55			
0.4	5.60	5.29	5.25			
0.5	6.03	6.24	6.11			
0.6	7.34	7.40	6.95			
0.7	7.79	7.74	7.56			
0.8	8.72	8.56	8.73			
0.9	9.65	9.52	9.44			
1	10.06	10.05	9.57	9.80	10.15	10.22
1.1	10.62	10.50	10.35	10.68	10.77	10.99
1.2	11.02	11.00	10.78	11.50	11.44	11.28
1.3	11.13	11.44	11.10	11.78	11.52	12.04
1.4	10.89	11.23	11.15	11.81	11.93	12.09
1.5	11.14	11.01	11.18	11.66	12.04	12.15
1.6	10.65	10.70	10.75	11.49	12.04	11.84
1.7	10.11	9.93	10.24	11.19	11.23	11.20
1.8	9.21	9.36	9.51	10.43	10.64	10.45
1.9	7.82	8.21	8.52	9.32	9.58	9.47

	Sieve Size					
	38-45µm	45-53µm	53-61µm	75-90µm	90-106µm	106-125µm
Dist. from face	Velocity (m/s)					
Step 9						
0.1	4.69	4.01	4.74			
0.2	5.35	5.32	4.95			
0.3	5.87	5.80	5.28			
0.4	6.51	6.46	6.23			
0.5	7.04	7.02	7.38			
0.6	7.98	8.08	7.13			
0.7	8.45	8.36	7.42			
0.8	9.18	8.89	8.63			
0.9	9.57	9.75	9.71			
1	10.22	10.13	9.75	10.12	9.95	10.01
1.1	10.46	10.22	10.23	10.38	10.34	10.43
1.2	10.65	10.41	10.42	10.81	10.51	10.90
1.3	10.55	10.63	10.57	11.15	11.31	11.50
1.4	10.88	10.57	10.69	11.38	11.32	11.67
1.5	10.70	10.51	10.32	11.50	11.22	11.40
1.6	10.20	10.07	10.06	11.02	10.91	11.46
1.7	9.43	9.37	9.60	10.79	10.63	10.54
1.8	8.62	8.70	8.88	9.97	10.21	10.37
1.9	7.51	7.75	7.94	8.99	8.98	9.30
Step 12						
0.1	5.83	5.86	5.43			
0.2	6.5	6.13	6.31			
0.3	7.03	7.02	6.66			
0.4	7.43	7.45	7.24			
0.5	7.72	7.69	7.55			
0.6	8.42	8.29	7.98			
0.7	8.49	8.54	8.2			
0.8	8.87	9	8.39			
0.9	8.88	8.89	8.35			
1	9.01	9.16	8.77	9.66	9.81	
1.1	9.06	9.01	9	9.91	9.71	
1.2	9.18	9.23	9.09	10.02	10.13	
1.3	9.05	9.23	8.96	10.1	10.5	
1.4	8.77	8.97	8.84	10.34	10.19	
1.5	8.52	8.52	8.74	10.14	10.27	
1.6	7.95	8.32	8.3	9.92	9.67	
1.7	7.64	7.63	7.77	9.27	9.52	
1.8	6.87	7.31	7.19	8.65	9.01	
1.9	6.25	6.32	6.46	7.65	8.21	